THM MODELLING OF THE ALC1604 EXPERIMENT

FINAL REPORT

S. Tourchi, J. Vaunat & A. Gens

International Centre for Numerical Methods in Engineering (CIMNE)

Universitat Politècnica de Catalunya (UPC)

Barcelona, July 1-, 2019

Executive summary

The report presents an interpretation of the full-scale HA-ALC1604 in situ heating test carried out on Callovo-Oxfordian claystone (COx) in the Meuse/Haute-Marne underground research laboratory (MHM-URL). The MHM-URL is a site-specific facility planned to study high-level radioactive waste disposal in the Callovo-Oxfordian claystone. The main aims of ALC full-scale emplacement experiment performed within the context of in the EU project LUCOEX (WP3) and consists in demonstrating the construction feasibility of a High-Level Waste (HLW) cell representative of the 2009 benchmark concept and in determining the impact of thermal loading on the overall behaviour of the cell. The experiment has also been used to acquire new data on the THM behaviour of the surrounding rock and to compare them with those acquired in previous small scale heating experiments.

The concept of the test consists of a horizontal micro-tunnel approximately 25 m long and 0.7 m in diameter, which excavated in the direction of the major horizontal stress. The excavation rate of the micro-tunnel was around 0.3-0.5 mh-1, and the excavation was completed in seven days. A non-alloy steel casing is placed in the cell body. The cell head has a metal sleeve called the Insert. Five heaters (H1 to H5), each 3 m long and 0.5 m in diameter, have been installed in the body section, continuously. The power applied in the deepest 15m was constant and equal to 220 W/m, in order to reach around 85 ºC in two years. Heating has been applied in two stages; A cooling stage (also applied in steps) completes the experiment. A comprehensive instrumentation system has been installed to gather observations that define the THM behaviour of the argillite. The test has been completed by the schedule envisaged.

Interpretation of the test has been assisted by the performance of a series of analyses simulating the experiment reported in this document. Coupled 3D-THM numerical analyses have been carried out to provide a structured framework for interpretation, and to enhance understanding of THM behaviour of Callovo-Oxfordian claystone. Numerical analyses have been based on a coupled theoretical formulation that incorporates a constitutive law especially developed for this type of material. The law includes several features that are relevant for a satisfactory description of the hydromechanical behaviour: anisotropy of strength and stiffness, behaviour nonlinearity and occurrence of plastic strains before peak strength, significant softening after the peak, time-dependent creep deformations and permeability increase due to damage. Particular attention has been devoted to the modelling of the steel lining and the gap between it and the rock.

By performing the numerical analysis, it has been possible to incorporate anisotropy of material parameters and of in situ stresses. The performance and analysis of the in situ tests have significantly enhanced the understanding of a complex THM problem and have proved the capability of the numerical formulation to provide adequate predictive capacity. The reference analysis has achieved a satisfactory reproduction of the pore pressure observations in all the sensors. Anisotropy effects during heating and cooling are adequately captured. They generally support the values of the THM parameters used in the simulation of previous experiments.

More specifically, several thermal analyses have been performed to obtain the best estimated values of anisotropic thermal conductivity that lead to the closest reproduction of the temperatures recorded during the test. They differ by 2.5% from the reference values in both the direction parallel and orthogonal to the bedding plane. As a general rule, an excellent reproduction of the temperature

field and its variation with time during both heating and cooling has been achieved. Those optimised anisotropic thermal conductivity parameters are subsequently used in the THM computations.

As foreseen, heating of the Callovo-Oxfordian argillite has resulted in significant increases of pore pressures due to the differential thermal expansion of pore water and soil skeleton and solid phase. The evolution of pore pressures is the result of the interplay of pore pressure generation by heating and pore pressure dissipation. Observations of pore pressures show that the evolution of pore pressures is affected by the anisotropic properties of thermal conductivity, stiffness and permeability and the increase of permeability in the Excavated Damaged Zone. Numerical THM model provide results in good agreement with all the pore pressure sensors.

A specific feature of ALC1604 experiment is the presence of a steel lining around the heater and a gap between the steel lining and the rock, that are slightly eccentric with respect to the centreline of the micro-tunnel because of the weight of both heater and steel lining. This peculiar feature has been carefully reproduced in the 3D model and allows for a well-reproduction of lining deformation during all the experiment. Aspects like lining ovalization during convergence of the rock on the lateral side of the lining, ovalization stop when lining enters in contact with the vault of the micro-tunnel and further ovalization inversion is well-captured by the model.

The HA-ALC1604 experiment has yielded valuable data on the in situ behaviour of the Callovo-Oxfordian claystone subjected to heating and cooling around a HA disposal cell as well as on the response of the steel lining. Interpretation, based on thermal and coupled THM analyses, has proved satisfactory showing that the processes involved are well understood and adequately incorporated in the formulation and associated computer code. It is worth noting that the numerical works performed in this project have converged to a unique final three-dimensional model accounting for most experiment elements (rock, steel lining, insert, gap, thermos-hydraulic effect of surrounding galleries), based on THM parameters consistent with those used in other tests, and reproducing well all measurements.

Table of contents

1. Introduction

The HA-ALC1604 experiment is an in situ heating test performed in the Meuse/Haute-Marne underground laboratory where the host rock is Callovo-Oxfordian (COx) argillite. It has been designed and put in go by ANDRA as a continuation of the work carried out in the TER and TED experiment.

The HA-ALC1604 is an experiment designed to evaluate the arrangement of a real alveolus for nuclear waste disposal. Therefore, there are essential differences between this experiment and the TER and the TED experiments. The most relevant differences are the longitudinal dimension of the heated zone and the existence of the casings that composed the alveolus. This arrangement allows for the observation of:

- The hydro-mechanical (HM) effects of the excavation of the micro-tunnel.
- The temperature field generated by a series of heaters installed along the alveolus.
- The overpressure generated in the domain affected by the heaters.
- The mechanical responses of the casings due to the thermal load imposed by the heaters and the thermo-hydro-mechanical response of the argillite.
- The THM evolution of the air gap located between the casings and the argillite.

It is known that the other important issue is the superposition of the several temperature fields generated by a sequence of alveoli along with the galleries, but it was covered in the experiment TED. The main aims of the experiment are the field observation of the thermo-hydro-mechanical (THM) behaviour of the argillite as well as contributing to the characterization of the argillite, the estimation of various THM parameters based on the experiment results and relevant information coming from the past field experiments and finally evaluate the overall response of the system designed, including the effects of steel lining and gap between it and the rock. This final report presents the most relevant results of the series of numerical analysis performed about this experiment, together with comparisons with the field observations.

This report is organised into five sections. Section 1 is an introduction. Section 2 describes the essential features of the HA-ALC1604 test, whereas the theoretical formulation is presented in Section 3. The results of the thermal analyses are collected in Section 4, and the THM results are presented in Section 5. Finally, Section 6 contains the main conclusions and goals for future tasks. Additional information has been organised in the Appendices in order not to disturb the natural flow of the report.

2. The HA-ALC1604 test

Based on the useful information obtained in the past thermo-hydro-mechanical experiments TER and TED (Gens *et al.*, 2013), the HA-ALC1604 experiment has been designed to evaluate the behaviour of a system similar to the real alveolus in which the nuclear waste will be placed {Citation}. As Figure 1 shows, the general scheme of an alveolus is a micro-tunnel composed of two main parts. At the back part of the excavation, it is found the operative zone ("Partie utile") where the nuclear waste will be placed during the operational phase of the repository and the beginning of the excavation ("Téte d'alveole") in which a sealing system will be installed after the waste disposal. All parts of the alveolus are covered with steel casings in contact with the host rock. Therefore the study of the contacts between the different parts of the arrangement is crucial.

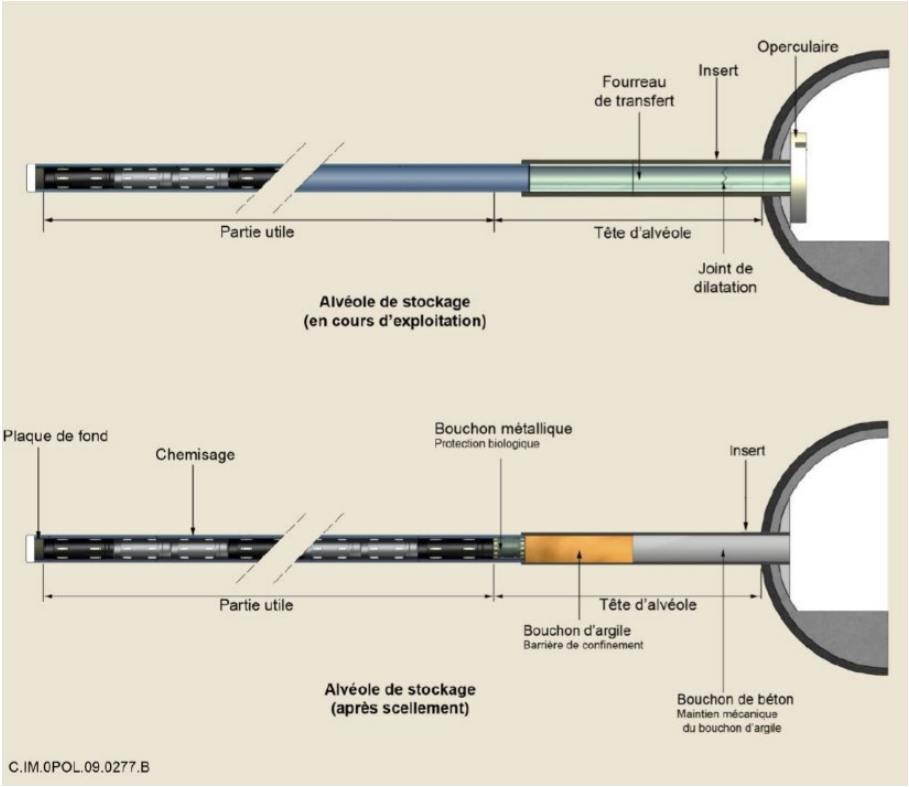

Figure 2-1 General scheme of HA alveoli. (Andra, 2013).

HA-ALC1604 experiment aims at simulating a configuration based on the concept developed for HA alveoli. The main difference between the previous heating in-situ experiments. It consists of a 25 m long micro-tunnel (alveolus) divided into two parts. The first part ("Tête d'alvéole") has a diameter of 0.79 m and a length of 6 m long. The second part ("Partie utile") has a diameter of 0.75m (Figure 2) and a length of 19 m. Five heaters (H1 to H5), each 3 m long and 0.508 m diameter, have been installed in the back of the alveolus, contiguously. The nominal power to be applied in each heater has been designed to achieve a maximum temperature of 90ºC on the rock-casings interface when all heaters are simultaneously switched on, a design requirement of the repository.

The HA-ALC1604 experiment is located in the GAN gallery, at the main level (490 m deep, see Figure 2-2). The excavation of the GAN Gallery started in September 2010 followed by the drilling of the alveolus on 23 October 2012 during seven days. The excavation of the boreholes for the instrumentation sensors started on 31 October 2012 (Table 2-1). A heating test was performed from 30 January 2013 to 15 February 2013. The heating phase started on 18 April 2013 with the same nominal power in all heaters (Figure 2-3) and was maintained up to 6th February 2019. Afterwards, three-steps cooling phase was launched and is still ongoing. Some power cut-offs episodes have occurred during the experiment. As indicated the Figure 2, the alveolus was excavated on the direction of the major horizontal stress. This fact has important implications for the hydro-mechanical response of the rock around the excavations.

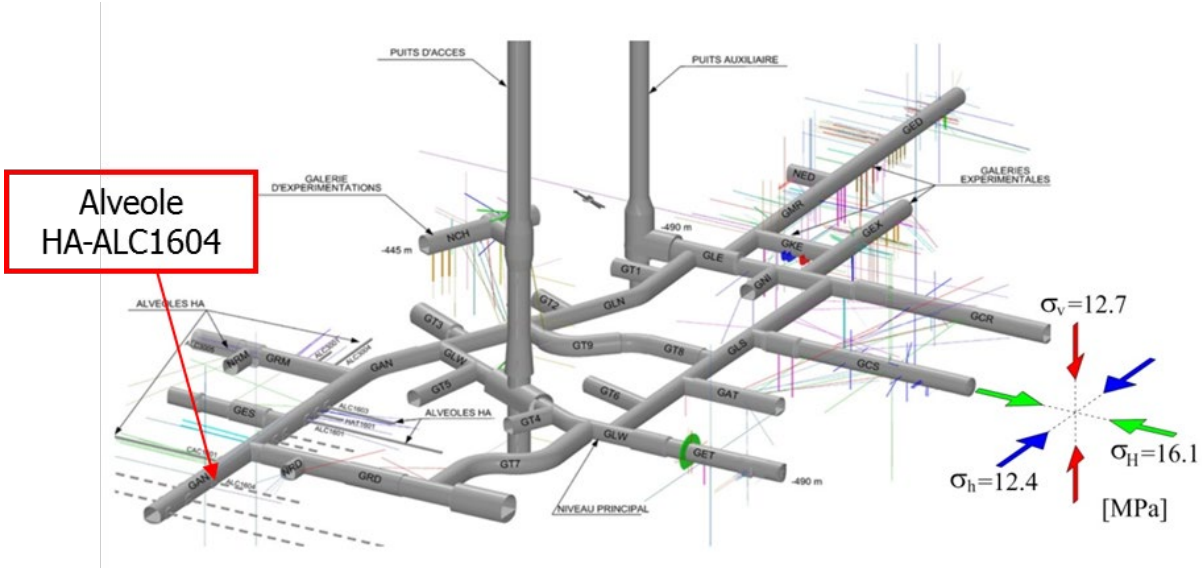

Figure 2-2 Location of the HA-ALC1604 alveolus in a three-dimensional view of the Mause/Haute-Marne Laboratory. The main galleries, as well as the boreholes at the main level -490 m are indicated (Andra, 2012).

Table 2-1. Stages of HA-ALC1604 experiment

Step	Phase	Date	Duration
1	Galleries GAN-GRD Excavation	September 9, 2010 → October 23, 2012	775 days
2	Alveoli Excavation	October 23, 2012 → October 31, 2012	56h
3	Boreholes/Instrumentation	October 31, 2012 → January 30, 2013	94 days
4	Heating Test (30W/m)	January 30, 2013 → February 15, 2013	16 days
5	Cooling	February 15, 2013 → April 18, 2013	61 days
6	Heating Stage (220W/m)	April 18, 2013 → February 6, 2019	~6 years
7	First cooling phase (85W/m)	February 6, 2019 → April 8, 2019	61 days
8	Second cooling phase (35W/m)	April 8, 2019 → June 11, 2019	64 days
9	Final cooling phase	June 11, 2019 → August 4, 2025	~6 years

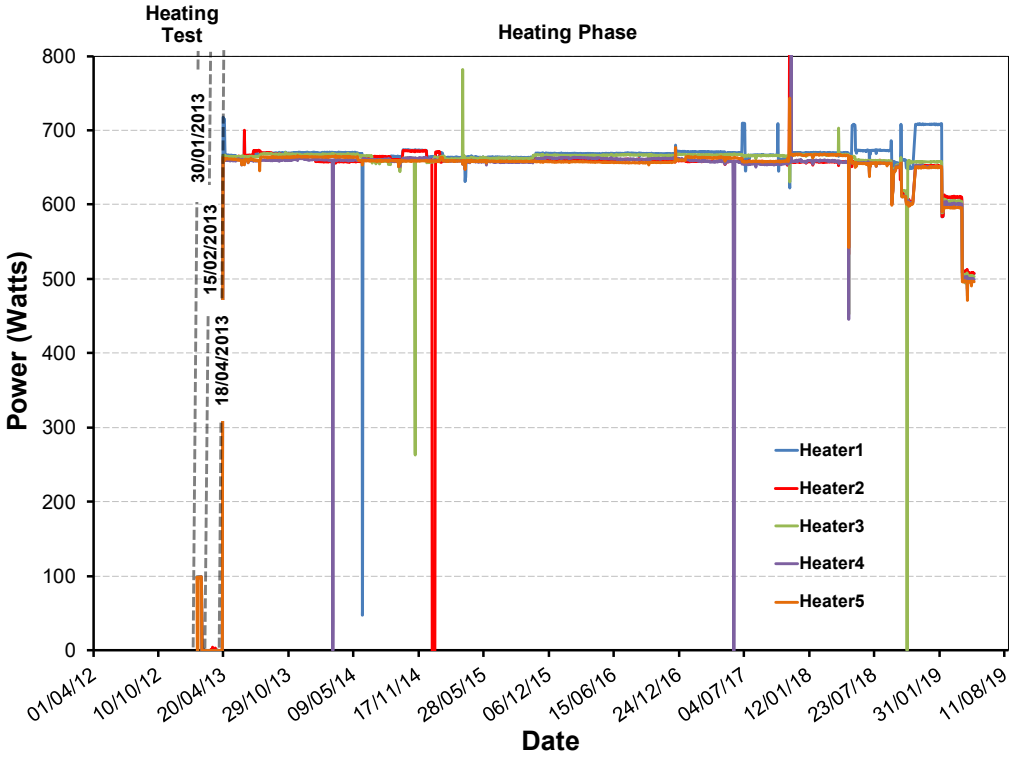

Figure 2-3 Timeline of the HA-ALC1604 experiment with the different heating stages applied until the moment.

The alveolus has been heavily instrumented from the gallery GAN and the niche NRD (Figure 4). The THM behaviour of the argillite has been studied through 9 boreholes that contain 28 temperature sensors, 18 piezometers and one extensometer with 20 points of measurements. The temperature and convergence of the gallery GAN are also instrumented.

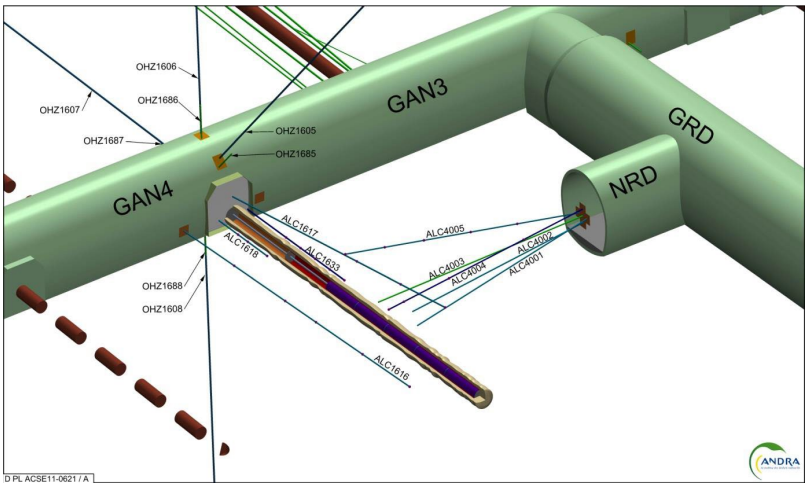

Figure 2-4 Instrumentation boreholes of the HA-ALC1604 alveolus in a three-dimensional view. (Andra, 2013).

More specifically, the instrumentation of the THM behaviour of the argillite in the HA-ALC1604 experiment comprises (Figures 2-4 and 2-5):

- Six boreholes with one (ALC4001 and ALC 4002), three (ALC1617 and ALC1618) and five (ALC4005 and ALC 1616) piezometer chambers associated with temperature sensors to measure the pressure gradient from the gallery into the rock mass and the pressure evolution near to the heated zone. These boreholes are backfilled with resin to ensure permeability and low compressibility.
- Two boreholes with five temperature measurement (ALC4003 and ALC1633) installed from the gallery niche NRD and gallery GAN, respectively. The boreholes are backfilled with a mix of bentonite and grout in order to reproduce the characteristics of the rock, mainly its permeability.
- The strain measurement borehole (ALC4004) equipped with 20 extensometers. These boreholes are located perpendicular to the heaters, and it is installed from the NRD niche.

Conversely to TED experiment, HA-ALC1604 does not focussed only on a specific plane. Figure 2-5 shows a horizontal cross-section that coincides with the bedding plane. It shows all the borehole lines (ALC1916, ALC1617, ALC1618, ALC1633, ALC4001, ALC4002, ALC4003, ALC4004 and ALC4005) as well as all the vertical cross-sections where sensors measurements are available (Y = 3, 4, 4.5, 5, 10, 13 13.6, 14.5, 17.5 and 22 m).

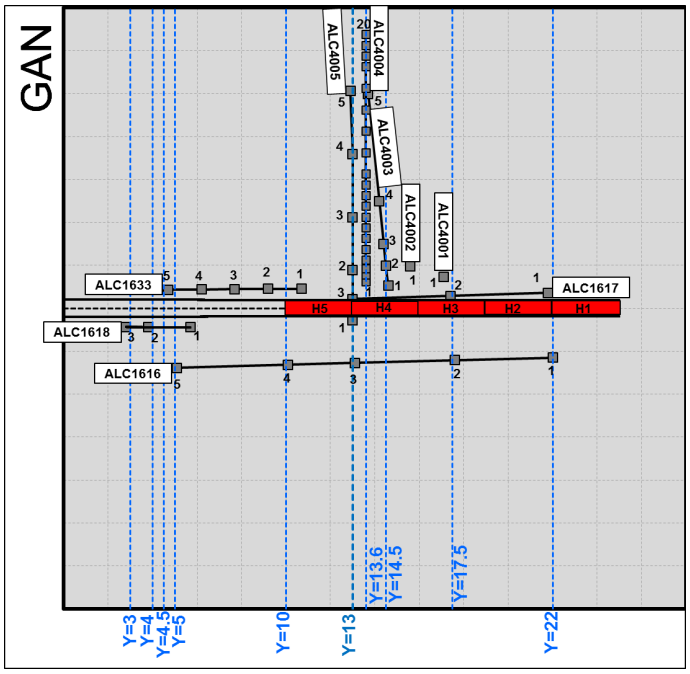

Figure 2-5 Horizontal cross-section of the instrumentation and alveolus arrangement.

Specific instrumentation was also installed to follow the responses of the steel casing and the contacts with the rock (Figure 2-6). Temperature on steel casing is monitored in 13 sections. Vertical and horizontal convergence of the casing is measured in six sections in the heated zone and in three sections in the non-heated zone. Relative humidity and gap aperture are monitored in the gap between the steel lining and the host rock. Figures 2-7 and 2-8 depict the location of temperature measurements on the steel casing and at the contact casing/argillite. Casing temperature is monitored at two points per sections, located at 15 degrees on the left and right of alveolus vertical centreline. Temperature in the gap is monitored at one point *per* section.

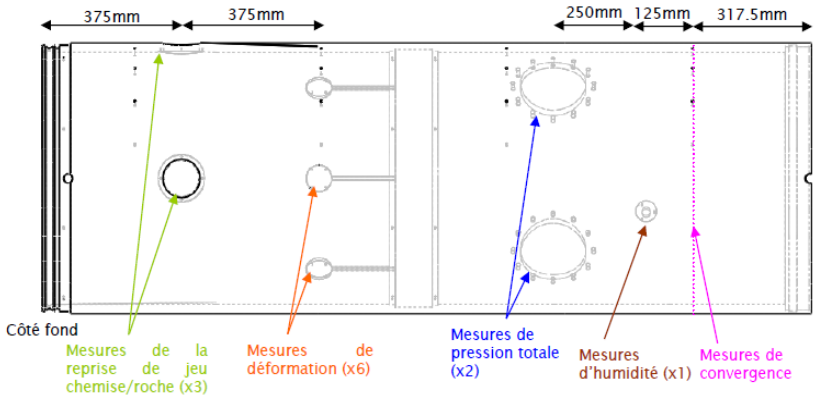

Figure 6 - Détails de l'instrumentation d'une chemise (vue 1)

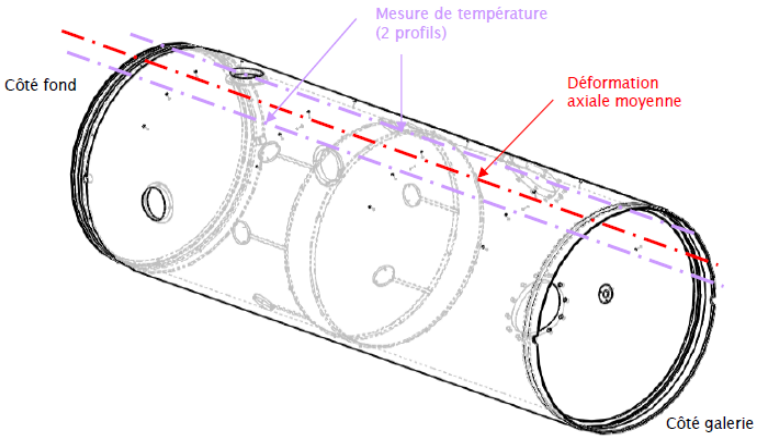

Figure 2-6 Location of the instrumentation on the steel casings. (Andra, 2013).

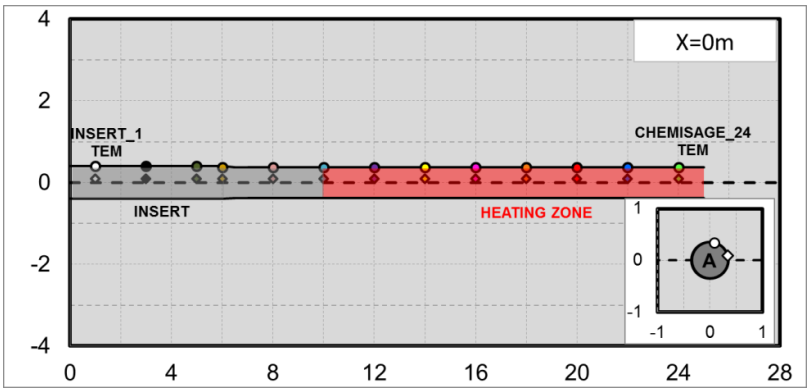

Figure 2-7 Vertical cross-section of the alveolus (perpendicular to bedding plane) indicating the location of temperature measurements.

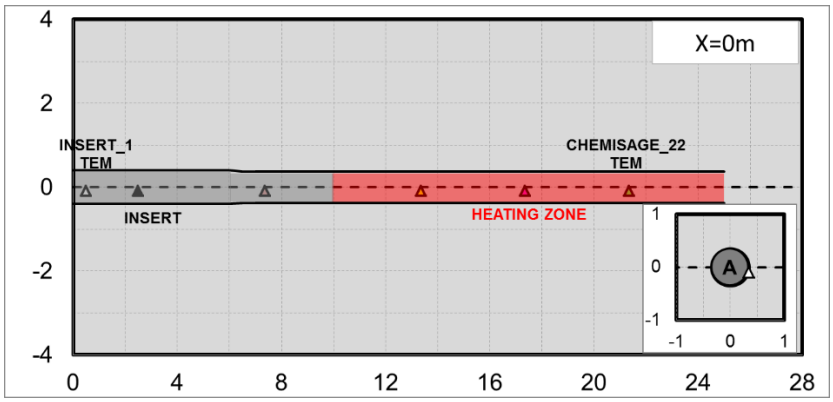

Figure 2-8 Vertical cross-section of the alveolus (perpendicular to bedding plane) indicating the location of temperature measurements at the contact casings/rock.

3. Theoretical Formulation

This section describes the theoretical formulation of the coupled thermo-hydro-mechanical (THM) processes that take place during the heating in a porous medium using a multi-phase, multi-species approach (Olivella *et al.*, 1994). Before a numerical simulation can be performed, a physical conceptual model is required. Therefore, a review of the physical processes and mechanisms thought to take place during the heating of a low permeability stiff porous medium are first summarised.

3.1 Basis of the formulation

Processes occurring in a heating experiment in argillaceous rocks can be described in terms of mass and heat transport phenomena in deformable porous media. The fluids present in the rock, in the more general case, are pore water and air. Temperature and pressure gradients cause all three phases to flow simultaneously. Each phase may consist of several components and the dispersive and diffusive effects of components within each phase account for transport. Changes in pressure and temperature are further accompanied by deformation of the porous medium. Mass balance equations can, therefore, be established to determine the spatial and temporal variations of each of the components, within each of the phases present. An energy balance equation determines the temperature variations.

The formulation for saturated materials is a particular case of the general formulation (Olivella et al. 1994). The formulation is based on a multiphase, multispecies approach. It is assumed that the porous medium is composed of three species: mineral (-), water (w) and air (a), distributed in three phases: solid (s), liquid (l) and gas (g). In the particular form presented here, the mineral phase and the solid phase coincide. However, the liquid phase may contain dissolved air, and the gas phase is a mixture of water vapour and dry air.

Local equilibrium is assumed throughout. To construct a well-posed mathematical system for the description of the stress, pore pressure, flux and deformation in the porous medium, equations based on mass and momentum conservation principles need to be introduced. Together with the constitutive laws and equilibrium restrictions, these equations constitute the governing equations.

3.2 Balance equations

Balance or conservation principles express fundamental physical observations concerning the interaction of a continuum medium and the environment. They reflect the balance of the most essential physical measures for the body of interest.

A general balance equation contains three terms: the change concerning the time of a property of the porous material ψ, the divergence of the flux of this property and the rate of production/decay of the property, given by:

$$\frac{\partial}{\partial t}\left(\theta_{\psi}\cdot\rho\right)+\nabla\cdot\left(j_{\psi}\right)-f^{\psi}=0 \qquad (1)$$

Where θ_ψ is the mass content of ψ per unit volume, j_ψ is the total mass flux of ψ and f^ψ is the rate of production/decay of ψ per unit volume. Using a compositional approach, the volumetric mass of a species in a phase θ_ψ is the product of the mass fraction of that species, ω_ψ, and the bulk density of the phase, ρ.

The total mass flux of a species in a phase, j_ψ, can be decomposed into an advective flux caused by fluid motion and non-advective flux, and advective flux caused by solid motion, to simplify the equations.

Mass balance of water

This balance equation introduces the state variable P_l, liquid pressure, which is linked with the Darcy flux $\mathbf{q}_l$. As water is present in liquid and gas phases, the total mass balance of water is expressed as:

$$\frac{\partial}{\partial t}\left(\theta_l^w S_l \phi + \theta_g^w S_g \phi\right) + \nabla\cdot\left(\mathbf{j}_l^w + \mathbf{j}_g^w\right) = f^w \tag{2}$$

Where θ_l^w and θ_g^w are the mass content of water per unit volume of liquid and gas, respectively? S_l and S_g is the degree of saturation of liquid and gaseous phases, respectively and ϕ is the porosity. $\mathbf{j}_l^w$ and $\mathbf{j}_g^w$ are the total water mass fluxes in the liquid and gas phases concerning a fixed reference system and f^w is an external supply of water per unit volume of the medium.

The definition of the material derivative:

$$\frac{D_s}{Dt}(\psi) = \frac{\partial_s}{\partial t} + \frac{d\mathbf{u}}{dt}\cdot\nabla(\psi) \tag{3}$$

leads to the following expression of the water mass balance:

$$\phi\frac{D_s}{Dt}\left(\theta_l^w S_l + \theta_g^w S_g\right) + \left(\theta_l^w S_l + \theta_g^w S_g\right)\frac{D_s\phi}{Dt} + \left(\left(\theta_l^w S_l + \theta_g^w S_g\right)\phi\right)\nabla\cdot\frac{d\mathbf{u}}{dt} + \nabla\cdot\left(\mathbf{j}'^w_l + \mathbf{j}'^w_g\right) = f^w \tag{4}$$

In saturated materials, the water mass balance can be reduced to the following expression:

$$\frac{\partial}{\partial t}\left(\rho_l\phi\right) + \nabla\cdot\left(\mathbf{j}_l\right) = f^w \tag{5}$$

Mass balance of solid

The mass balance of solid in the medium can be written in terms of porosity:

$$\frac{\partial}{\partial t}\left(\theta_s\left(1-\phi\right)\right)+\nabla\cdot\mathbf{j}_s=0 \tag{6}$$

where θ_s refers to the grain content per unit volume of soil and $\mathbf{j}_s$ is the mass flux of solid.

Energy balance for the whole medium

The equation for internal energy balance for the porous medium is established taking into account the specific internal energy per unit mass of each phase $\left(E_s, E_l\right)$:

$$\frac{\partial}{\partial t}\left(E_s\rho_s\left(1-\phi\right)+E_l\rho_l\phi\right)+\nabla\cdot\left(\mathbf{i}_c+\mathbf{j}_{E_s}+\mathbf{j}_{E_l}\right)=f^Q \tag{7}$$

where $\mathbf{i}_c$ is the energy flux due to conduction through the porous medium, $\mathbf{j}_{E_s}$ and $\mathbf{j}_{E_l}$ are advective fluxes of energy caused by mass motions and f^Q is an internal or external energy supply.

Balance of momentum (equilibrium)

If inertial terms are neglected, the balance of momentum for the porous medium reduces to the equilibrium equation for macroscopic total stresses:

$$\nabla\cdot\boldsymbol{\sigma}+\mathbf{b}=\mathbf{0} \tag{8}$$

where $\boldsymbol{\sigma}$ is the stress tensor and $\mathbf{b}$ is the vector of body forces.

3.3 Constitutive equations

The formulation must be completed with various constitutive laws that describe the various phenomena under consideration. The constitutive equations establish the link between the state variables (or unknowns) and the dependent variables. The main constitutive laws correspond to the state equations for the density of solid, liquid and gas phases, the flow of heat by conduction, the advective flow of water, the storage term of water for unsaturated conditions (retention curve) and the constitutive law for mechanical behaviour.

Heat conduction is governed by Fourier's law:

$$\mathbf{i}_c=-\lambda\nabla T \tag{9}$$

where $\mathbf{i}_c$ is the conductive heat flux and λ is the matrix of transverse thermal conductivity:

$$\boldsymbol{\lambda}=\begin{bmatrix}\lambda_{//} & 0 & 0\\ 0 & \lambda_{//} & 0\\ 0 & 0 & \lambda_{\perp}\end{bmatrix} \tag{10}$$

Generalised Darcy's law is used to relate advective fluxes of fluid to phase pressure gradient:

$$\mathbf{q}_l = -\mathbf{K}\left(\nabla P_l - \rho_w g\right) = -\frac{\mathbf{k}}{\mu_l}\left(\nabla P_l - \rho_w g\right) \tag{11}$$

where $\mathbf{K}$ is the permeability tensor, $\mathbf{k}$ is the intrinsic permeability tensor and μ_l denotes the dynamic viscosity. Liquid permeability depends on temperature through the variation of water viscosity, and intrinsic permeability depends on porosity. The intrinsic permeability $\mathbf{k}$ depends on the pore structure of the porous medium by the Kozeny's law:

$$\mathbf{k} = \mathbf{k}_0 \frac{\phi^3}{\left(1-\phi\right)^2} \frac{\left(1-\phi_0\right)^2}{\phi_0^{\,3}} \tag{12}$$

where ϕ_0 is the reference porosity and $\mathbf{k}_0$ is the intrinsic permeability tensor for matrix ϕ_0:

$$\boldsymbol{k_0} = \begin{bmatrix} k_{0//} & 0 & 0 \\ 0 & k_{0//} & 0 \\ 0 & 0 & k_{0\perp} \end{bmatrix} \tag{13}$$

When solid skeleton deforms, the volume of pores and its distribution can change. Intrinsic permeability is, therefore, a function of volumetric deformation, which is computed on the basis of the displacements.

The relative permeability is considered a function of the effective degree of saturation, defined thought a generalized power law,

$$k_r = AS_e^{\Lambda} \tag{14}$$

where A and Λ are material parameters.

In the context of argillaceous materials, it is necessary to take into account the large increase of permeability that occurs when the rock experiences damage. In order to reproduce this phenomenon, permeability cannot be constant but should evolve with damage growth. In the context of the current elastoplastic model, this feature is incorporated by including a dependency of the intrinsic permeability on the plastic multiplier. An exponential function has been adopted for this purpose:

$$\boldsymbol{k} = \boldsymbol{k_0} e^{\eta(\lambda^p - \lambda_0^p)} \tag{15}$$

where k_0 is the intrinsic permeability of the intact rock, η is a constant that controls the rate of change, λ^p is the plastic multiplier and λ^p

The retention curve linking suction and equivalent degree of saturation is given by the Van Genuchten (Van Genuchten, 1980) expression:

$$S_e = \frac{S_l - S_{rl}}{S_{ls} - S_{rl}} = \left(1 + \left(\frac{s}{P}\right)^{\frac{1}{1-\lambda}}\right)^{-\lambda} \tag{16}$$

where S_{rl} is the residual degree of saturation, S_{ls} is the degree of saturation in saturated conditions (typically 1), and P and λ are model parameters.

The elastic part of the mechanical constitutive law is based on transverse isotropic elasticity, given by the following constitutive matrix:

$$\begin{bmatrix} \sigma_{xx} \\ \sigma_{yy} \\ \sigma_{zz} \\ \tau_{xy} \\ \tau_{xz} \\ \tau_{yz} \end{bmatrix} = \begin{pmatrix} \Delta\left(\frac{E_H}{E_V} - \nu_{HV}^2\right) & \Delta\left(\frac{E_H}{E_V}\nu_H + \nu_{HV}^2\right) & \Delta\nu_{HV}\left(1+\nu_H\right) & 0 & 0 & 0 \\ \Delta\left(\frac{E_H}{E_V}\nu_{HV} + \nu_{HV}^2\right) & \Delta\left(\frac{E_H}{E_V} - \nu_{HV}^2\right) & \Delta\nu_{HV}\left(1+\nu_H\right) & 0 & 0 & 0 \\ \Delta\nu_{HV}\left(1+\nu_H\right) & \Delta\nu_{HV}\left(1+\nu_H\right) & \Delta\left(1-\nu_H^2\right) & 0 & 0 & 0 \\ 0 & 0 & 0 & G_V & 0 & 0 \\ 0 & 0 & 0 & 0 & G_V & 0 \\ 0 & 0 & 0 & 0 & 0 & \frac{E_H}{2\left(1+\nu_H\right)} \end{pmatrix} \begin{bmatrix} \varepsilon_{xx} \\ \varepsilon_{yy} \\ \varepsilon_{zz} \\ \gamma_{xy} \\ \gamma_{xZ} \\ \gamma_{YZ} \end{bmatrix} \tag{17}$$

$$\Delta = \frac{E_H}{\left(1+\nu_{HV}\right)\left[\frac{E_H}{E_V}\left(1-\nu_{HV}\right) - 2\nu_{HV}^2\right]} \tag{18}$$

where *H* and *V* directions correspond, for the case of Callovo-Oxfordian, respectively to the direction in bedding plane (*P* in Fig. 3-1) and orthogonal to it (*S* in Fig. 3-1).

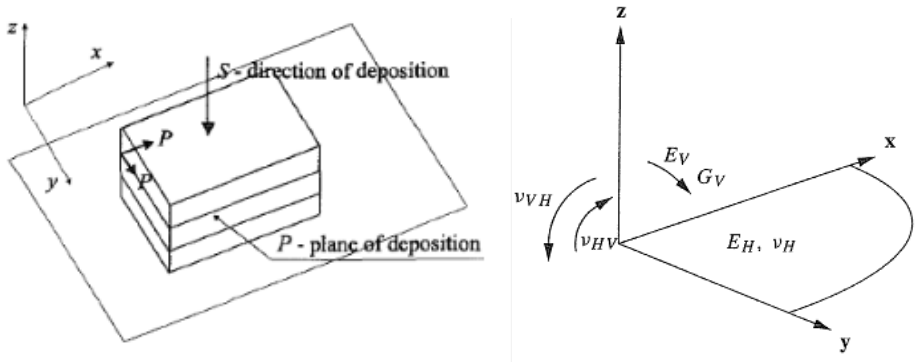

Figure 3-1. Axes orientation for considering transverse isotropy. The z-axis is in the direction of sediment deposition, S, while x and y axes are in the plane of deposition, P (Potts and Zdravkovic, 1999).

Stress appearing in Equation (17) correspond to the effective stress. Expressions for it in saturated and unsaturated conditions are given in Appendix 1.

The elastic law is further complemented with elastoplastic and creep equation according to the model for Mánica et al. (2016). Detailed equations of the model are presented in Appendix 1.

3.4 Computer code

All the numerical analyses presented in this report have been performed using the computer code CODE_BRIGHT (Olivella *et al.*, 1996). CODE_BRIGHT is a finite element programme (with some finite volume features) capable of performing coupled THM analyses involving both saturated and unsaturated media. It incorporates a wide range of multi-physics processes and an extensive library of constitutive laws for geomaterials (DIT-UPC, 2002).

4. Analysis of the thermal response

A proper interpretation of the thermo-hydraulic coupling requires a good representation of the thermal field throughout the domain (Gens *et al.*, 2007). To this end, the value of the thermal conductivity of the clay must be known as precisely as possible.

As stated above, the influence of the mechanical and hydraulic behaviour on the thermal response is negligible. The thermal conductivity of the host material does not change, because, throughout the whole experiment, it remains saturated, and the changes of porosity are minimal. Therefore, a purely thermal analysis can be performed to find the value of thermal conductivity that achieves the closest agreement with measured temperatures. The aim of this thermal analysis is, therefore, the interpretation of the temperature field obtained during the heating experiment and the determination of the optimum thermal parameters.

4.1 Thermal parameters

Two parameters are directly related to the thermal conduction problem: specific heat and thermal conductivity. Both parameters are dependent on the composition of the porous materials: porosity, mineralogy of solid phase and pore fluids. Specific heat is the amount of heat required to raise the temperature of the unit mass of the material by a given amount (usually one degree). Because of the storage nature of this parameter, a volumetric average considering the different constituents may be applied:

$$\rho \cdot C = \rho_s \cdot (1-\phi) \cdot C_s + \rho_w \cdot \phi \cdot S_r \cdot C_w + \rho_a \cdot \phi \cdot (1-S_r) \cdot C_a \tag{19}$$

Where the "*s*", "*w*", and "*a*" subscripts stand for solid, water and air, respectively, ϕ is the porosity and S_r is the degree of saturation. The specific heat of the solid phase of the rocks measured in laboratory experiments was 800 J/kg/K (Andra, 2005), resulting in values for the saturated porous materials of about 1000 J/kg/K for the Callovo-Oxfordian Clay (Conil et al. 2010). Because of the lower uncertainty associated with the specific heat that depends exclusively on the medium composition and not on grain arrangement, these values were assumed to be satisfactory estimates.

Conversely, thermal conductivity, the property of a material that indicates its ability to conduct heat, is not only influenced by the material composition but also by the arrangement of the different constituents. In argillaceous rocks, there is a specific arrangement of the clay particles because of their sedimentary nature. However, as a first approximation, the equation proposed by Farouki (1986) for the isotropic thermal conductivity of a random mixture of several materials can be applied to a porous medium as:

$$\lambda_0 = \lambda_s^{1-\phi} \cdot \lambda_w^{\phi \cdot S_r} \cdot \lambda_a^{\phi \cdot (1-S_r)} \tag{20}$$

Significant variations of carbonates or quartz, which are relatively high conductive minerals, are also known to occur in argillaceous rocks as a function of the sediment level and should be taken into account. The average composition of Callovo-Oxfordian Clay is 55% of clay, 28% of calcite, 17% of quartz and 15% of porosity. Considering the mineralogy and accounting for a thermal conductivity of the clay component of 1.1 W/m/K, of 0.7 W/m/K for the water and of 3.75 and 8 W/m/K for calcite and quartz crystals respectively, a first-order approximation of the saturated thermal conductivity of the Callovo-Oxfordian Clay of 1.8 W/m/K can be obtained.

During different laboratory experiment campaigns carried out on saturated COX samples, an evident influence of the heat flow orientation with respect to bedding was observed. Average values of 2 W/m/K and 1.3 W/m/K are indicated for the parallel and the perpendicular thermal conductivity values, respectively (Andra, 2005).

Taking these values as a departure, a three-dimensional sensitivity analysis has been performed to back-analyse the value of thermal conductivity that achieves the closest agreement with measured temperatures of the experiment. A slight variation of 2.5 % has been found with respect to the reference values in both directions: 2.05 W/m/K along bedding planes and 1.33 W/m/K orthogonal to it.

4.2 Evolution of applied power

HA-ALC1604 experiment is now in the cooling phase. Previously, after a short heating test, the nominal power (660 W) was reached in each heater (Figure 4-1). Conversely to past THM experimental tests, the nominal power was imposed in one single step.

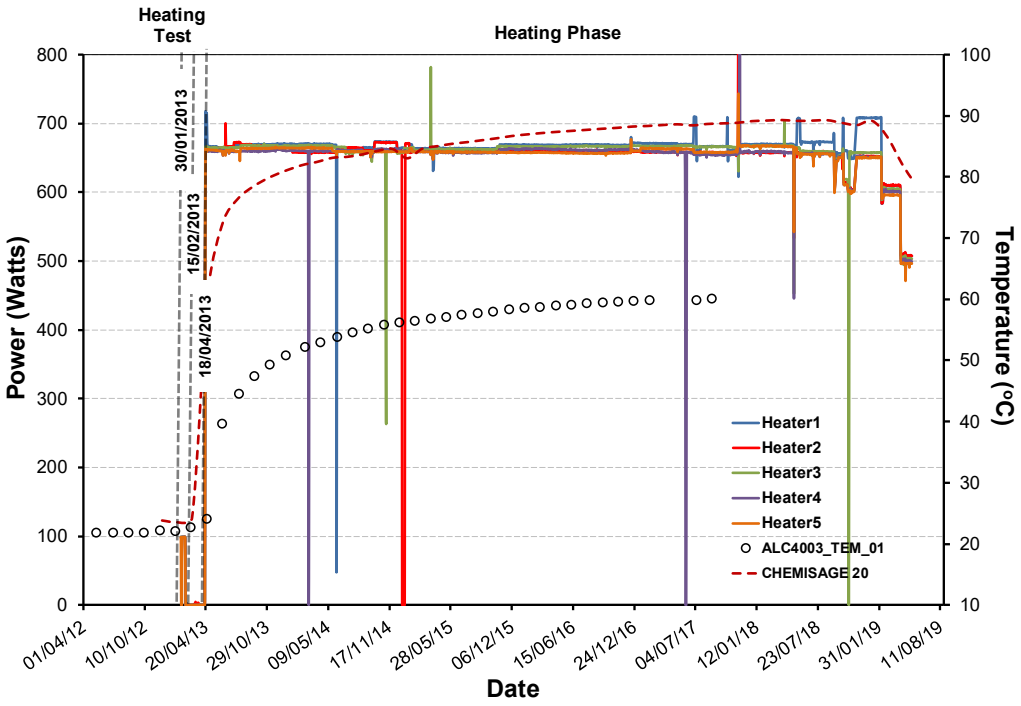

Figure 4-1. Evolution of the power applied. The temperature measured in the sensor ALC4003_TEM_01 and the steel casing temperature is added, to show the temperature response to the power input.

During the heating stage of the experiment, the input power will be maintained long enough to achieve a quasi-permanent state, in order to separate the transitory and the steady-state. Some punctual power cut-offs episodes have occurred during the experiment; however, they have had a negligible influence on the temperature evolution in the COx and punctual effects on the temperature evolution of the steel casing temperature (Figure 4-1).

4.3 Overview of temperature measurements

The gallery GAN influences the COx temperature evolution at a certain distance from the gallery wall. Until 5 meters inside the mass rock, the evolution of temperature is the combination of the periodic temperature changes in the gallery GAN and the input power in the heated zone (Figure 4-2). This influence of the temperature fluctuation in the gallery GAN is also registered at some meters inside of the steel casings and the gap between the COx and the casings (Figures 4-3 and 4-4).

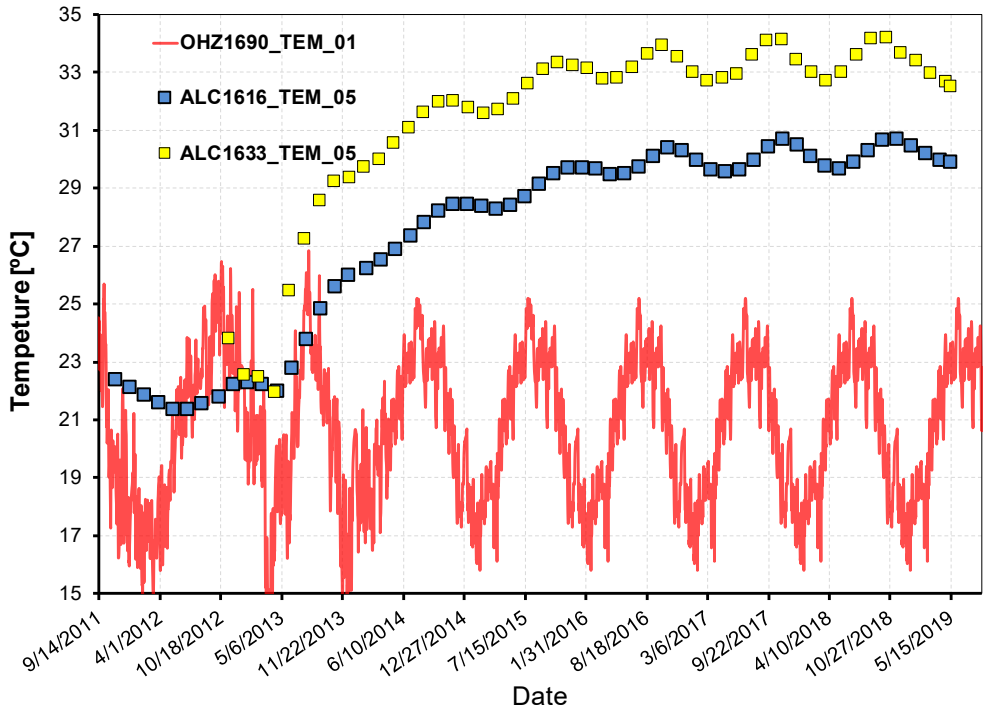

Figure 4-2. Evolution of temperature at 5 m from the gallery wall (Sensors ALC1616_TEM_05 and ALC1633_TEM_05). The temperature measured in the gallery GAN is also added, to show the influence of the gallery.

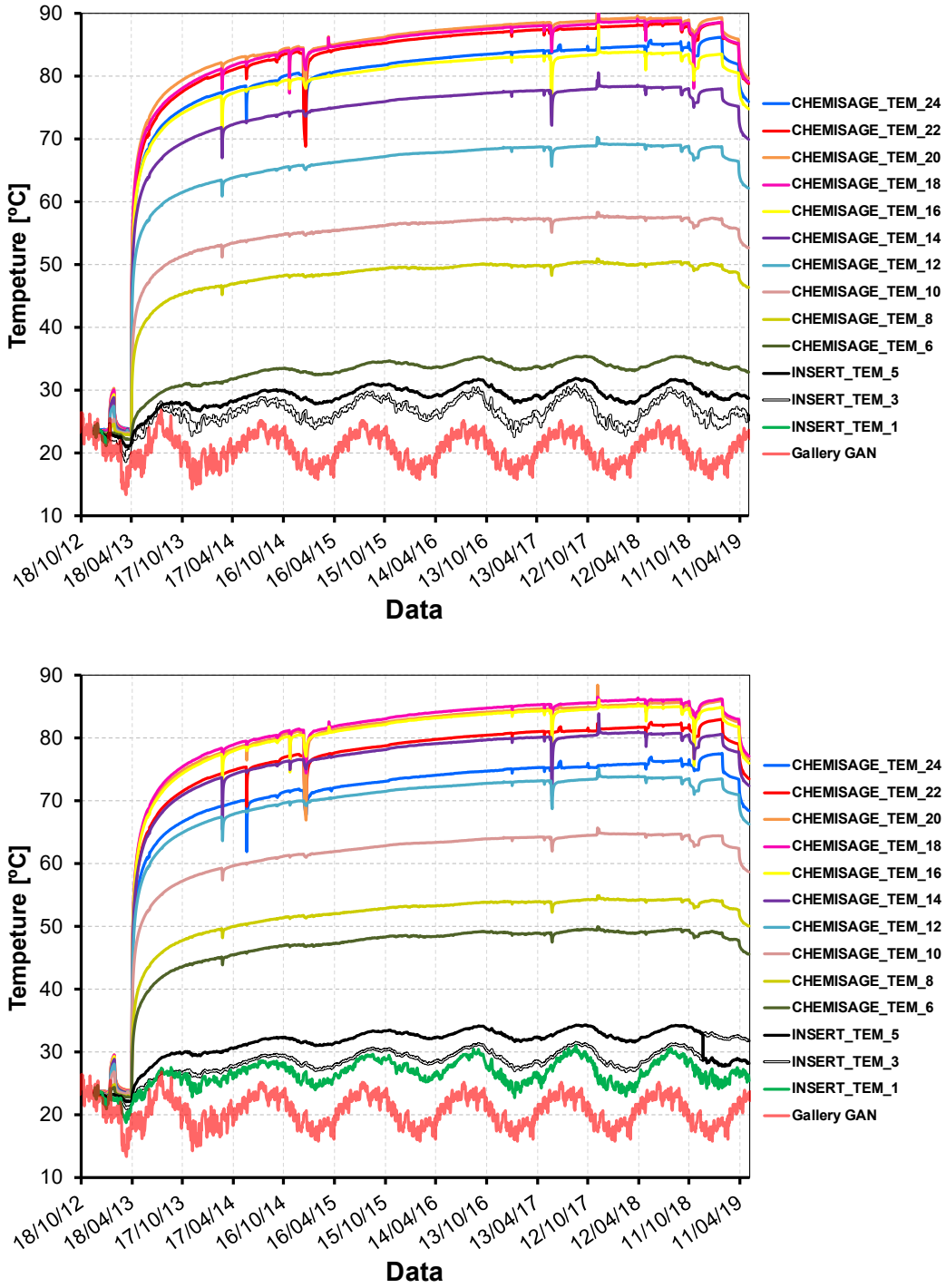

Figure 4-3. Evolution of temperature in the steel casing. Left: vertical measurements. Right: horizontal measurements. The temperature measured in the gallery GAN is also added, to show the influence of the gallery.

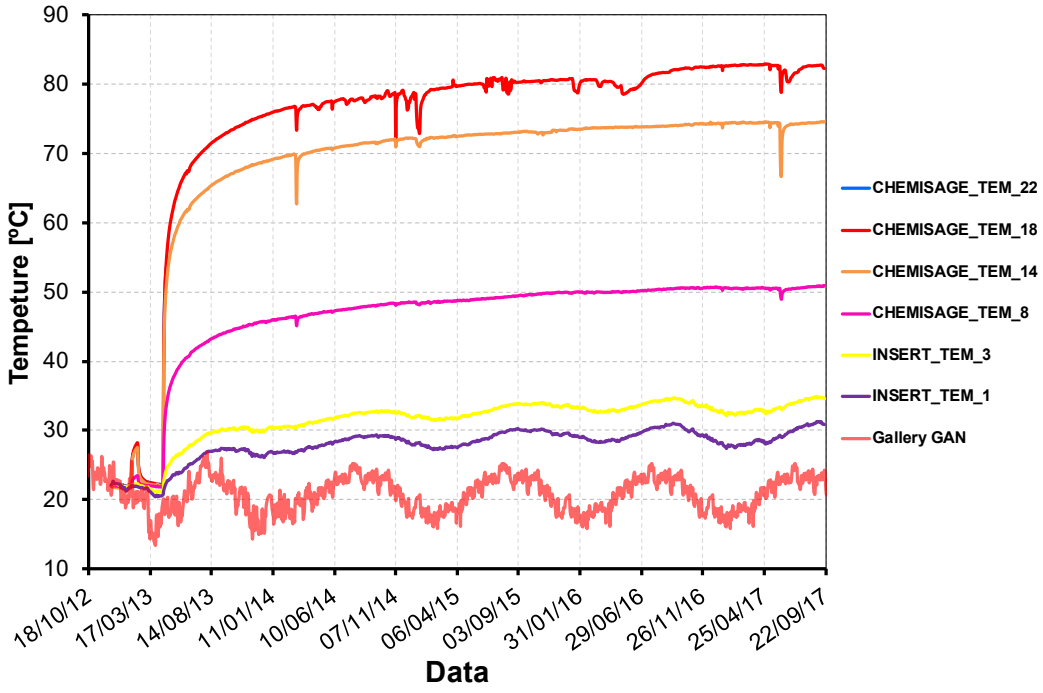

Figure 4-4. Evolution of temperature in the gap between the steel casing and the host rock. The temperature measured in the gallery GAN is also added, to show the influence of the gallery.

Figure 4-5 shows a comparison between two sensors located near (ALC4003_TEM_01) and far away (ALC4003_TEM_01) from the heaters. Both sensors indicate a marked increase in temperature when the input power started suggesting that the existence of a heat flow form the open part of the alveolus. This mechanism will be explored in detail during the numerical modelling.

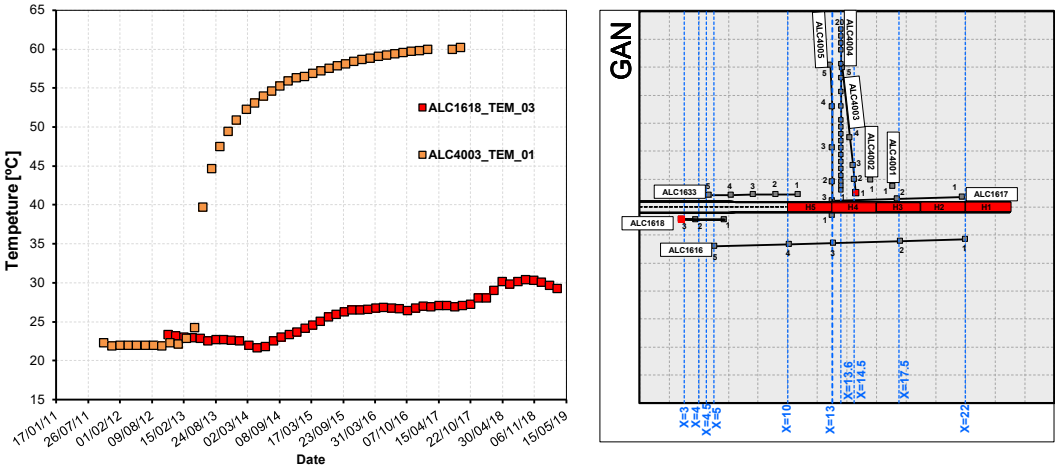

Figure 4-5. Evolution of temperature in the sensors ALC1618_TEM03 and ALC4003_TEM_01. Comparison between the heated and non-heated zone.

The influence of the input power of the heaters covers a large area around the alveolus. Figure 4-6 depicts the evolution of temperature at sensor ALC4003_TEM_05 located at 10 meters

from the heaters in a section at 13.6 m from the gallery wall. It experiences an increase of 4ºC since the input power activation. This observation will be used to define the size of the computational domain and put the boundary conditions at a distance where it is expected not to influence the temperature field during the whole test duration.. Temperature evolution also shows some small temporal variations generated by the influence of the niche NRD from which the borehole was drilled.

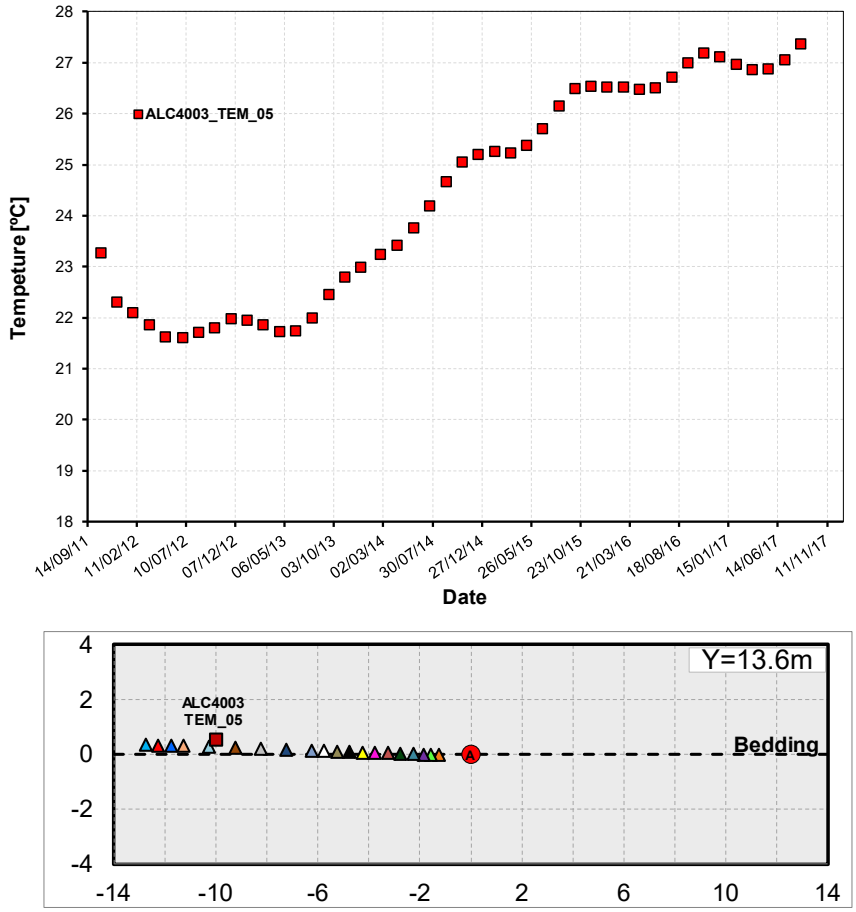

Figure 4-6. Evolution of temperature in the sensor ALC4003_TEM_05.

Conversely to TED experiment (Gens *et al.*, 2013), instrumentation was not designed to monitor a specific cross-section of ALC1604 experiment but to provide temperature measurements all around the test. A corollary of that is the difficulty to compare measurements at the same distance from the heaters and in different directions with respect to the bedding plane. As a matter of fact, only two sensors in the section located at 13 meters from the gallery wall (ALC1617_TEM_03 and ALC1616_TEM_03) obey to this criterion. Unfortunately, sensor ALC1617_TEM_03 became damaged and did not provide temperature evolution at the corresponding point (Figure 4-7). As a consequence, evidence of anisotropic thermal field can be only obtained by analysing the temperature output by numerical simulations that match the measurements.

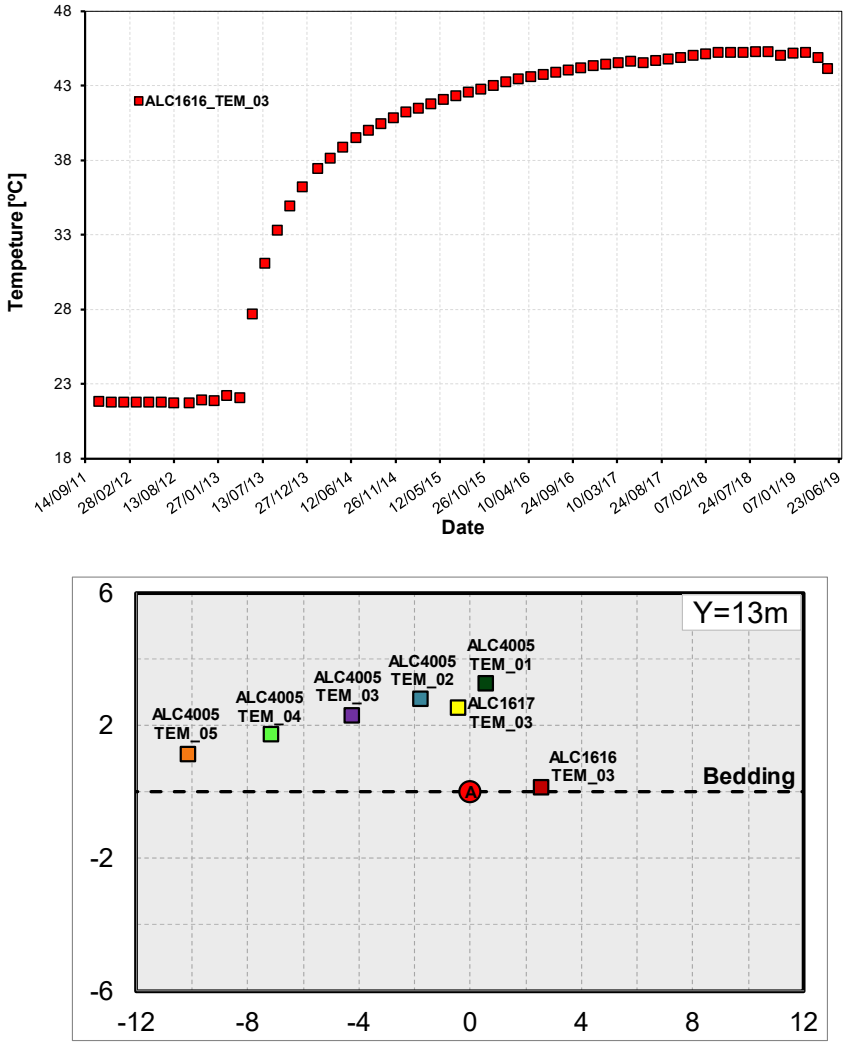

Figure 4-7. Evolution of temperature in the sensor ALC4003_TEM_05.

4.4 Thermal modelling

Although the finite element code CODE_BRIGHT allows for the performance of coupled Thermo-Hydro-Mechanical analysis, only the energy balance equation is solved at this stage of the work. From the thermal parameters determined in the TED experiment as a starting point, thermal computations have been carried out to determine the thermal parameters that exhibit the best agreement between the simulation and the measurements.

4.4.1 Domain discretisation

The heating experiment has been numerically simulated by use of a 3D model in order to reproduce the characteristic anisotropic features of the rock mass. The mesh used in this computation contains about 122 000 hexahedral elements and 129 000 nodes. The domain and the finite element mesh used are depicted in Figure 4-8.

The reference axis system corresponds to the local system defined for the HA ALC1604 experiment (Andra 2013): x-axis follows the centreline of the alveolus, y corresponds to the vertical axis and z is perpendicular to both. Origin is located at the alveolus section intersecting the GAN gallery. The computational domain has been divided into several parts that compose the alveolus, including the five sections that represent the heaters (H1 to H5). Finally, a section with the same length of the alveolus is considered in order to evaluate the heated zone in the host rock. The mesh has been refined near the gallery and near the alveolus, in order to be able to cope with the high temperature (and subsequently pore pressure) gradients in this zone.

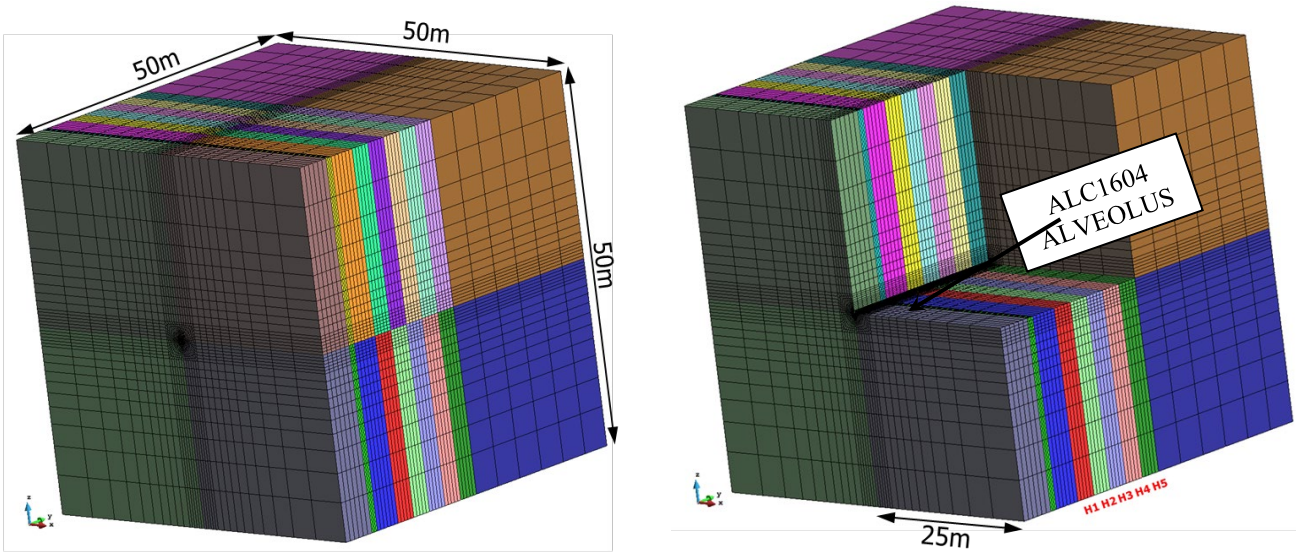

Figure 4-8. The geometry of the 3D mesh used for the purely thermal simulation. The alveolus ALC1604 is oriented parallel to the major horizontal stress direction.

Model includes the host rock domain, insert, steel lining and the gaps between the insert and the the COX, the iniset and the lining and the lining and the COx (Figure 4-9). For computational purposes, the gap will be dealt with as continuous medium. The discontinuous behaviour of this "material" at time of gap closure is modelled through a bi-linear elastic constitutive law. According to the experiment layout, the lining lies on the rock at the bottom of the alveolus. Thus both insert, lining and gaps are eccentric with respect to the centreline of the alveolus.

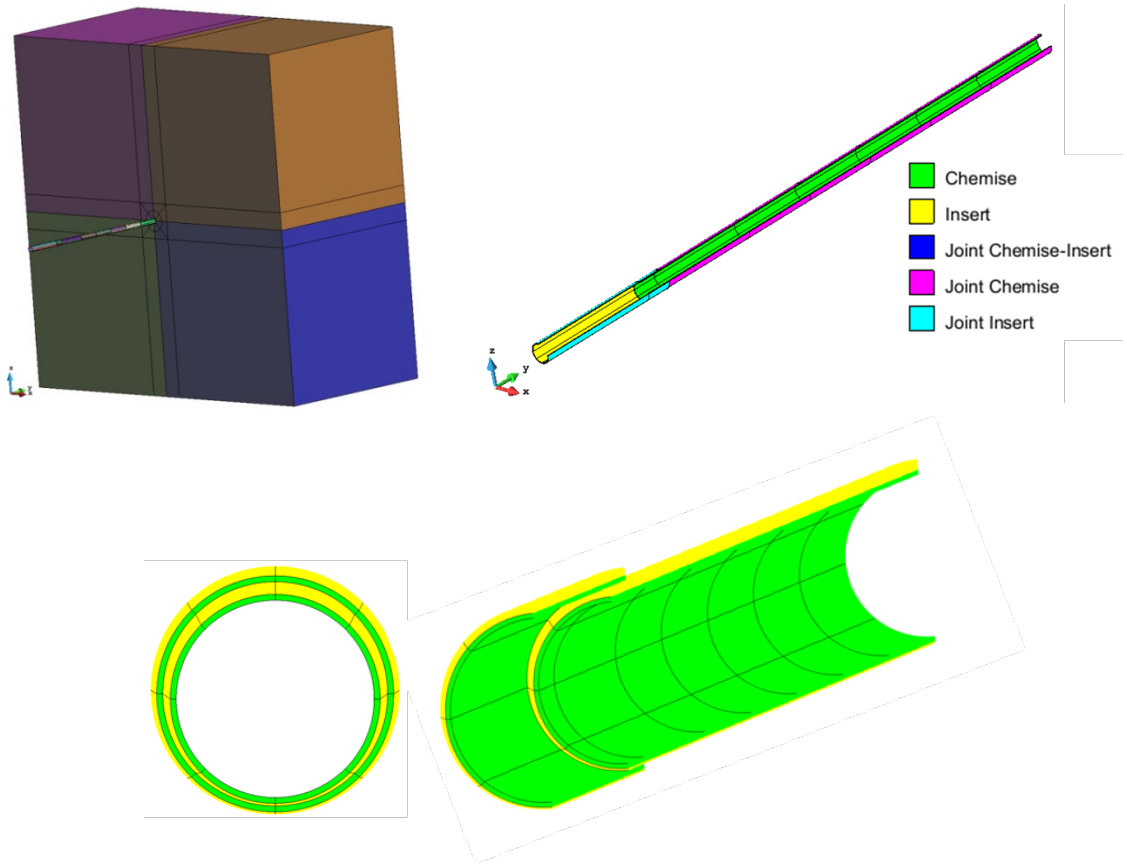

Figure 4-9. Geometry of the 3D model used for the steel casings and gap.

4.4.2 Initial and boundary conditions

The initial and boundary conditions are depicted in Figure 4-10. Heat fluxes have been prevented on all faces, except on the back, where the temperature is prescribed to 21.82 ºC.

A particular aspect relies on the influence of temperature changes of GAN and GRD galleries on the values of temperature at the sensors close to gallery wall. Consequently, a specific boundary condition has been applied at the loci corresponding to gallery walls (see Figure 4-10). It prescribes a continuous time evolution of temperature according to measurements taken

in gallery OHZ1690. This condition has been applied since 9th September 2010, date of GAN gallery excavation.

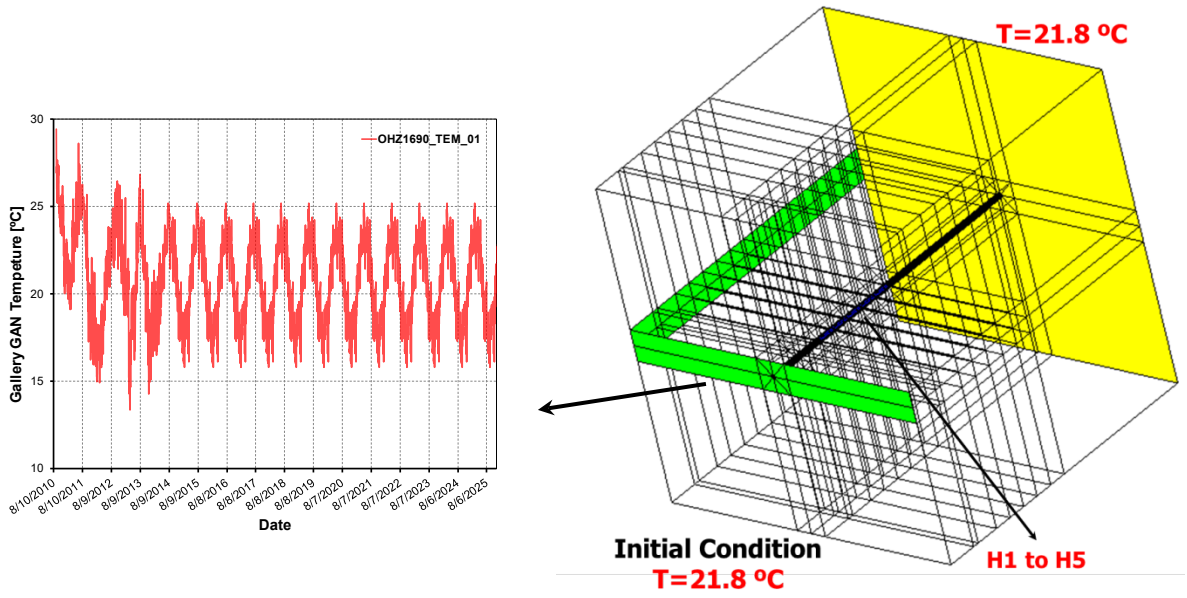

Figure 4-10. Initial and boundary conditions applied.

Another aspect corresponds to the boundary condition to prescribe in the non-heated part of the alveolus. As show in Figure 22, there no isolation between the heater and the non-heated part of the alveolus. As such, part of the power input will heat the air inside, leading to convective cells and some turbulent heat transfer processes toward this part of the alveolus.

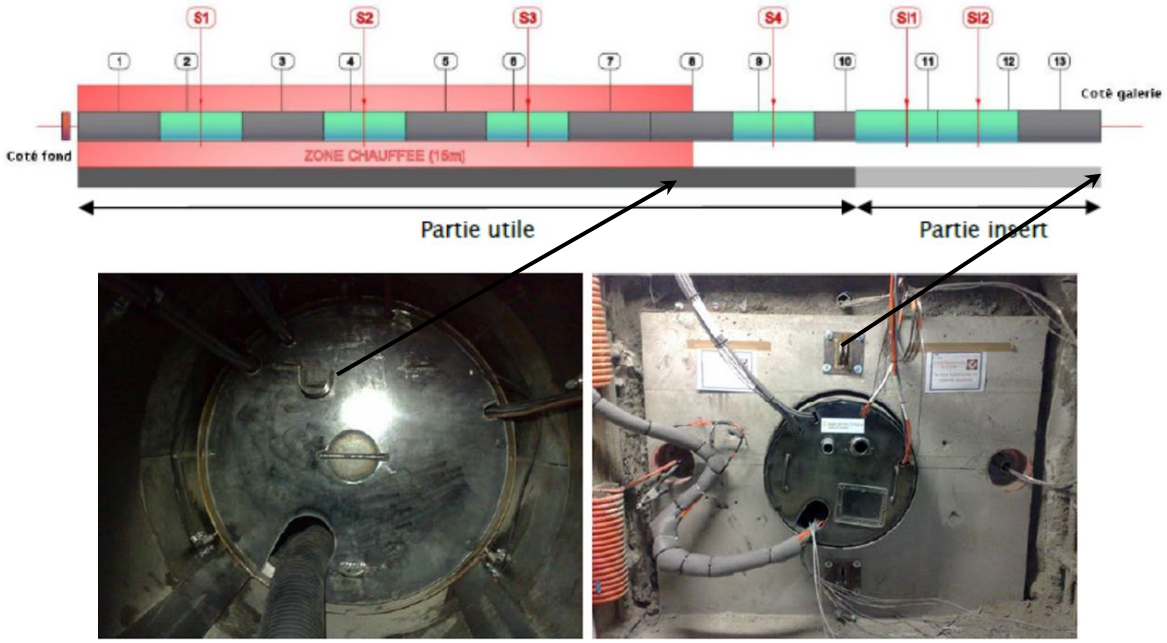

Figure 4-11. Parts of the alveolus. The heaters are not isolated; air convection occurs in the empty zone of the alveolus.

Since it is not possible to represent these processes with the formulation implemented in the model, several cases have been considered:

- The case in which the heaters are thermally isolated (Figure 4-12a). The total power input is applied directly in the heater zone. Results evidence that temperature measurement in front of the heated zone cannot be well-reproduced.
- Different cases where a small part of the power input to the heaters is removed from the heated zone and applied in the non-heated zone (Figure 4-12b). After an trial-error procedure based on the comparison between computed and measured temperatures in front of the heated and non-heated zone, the value of flux to apply in the non-heated zone has been determined.

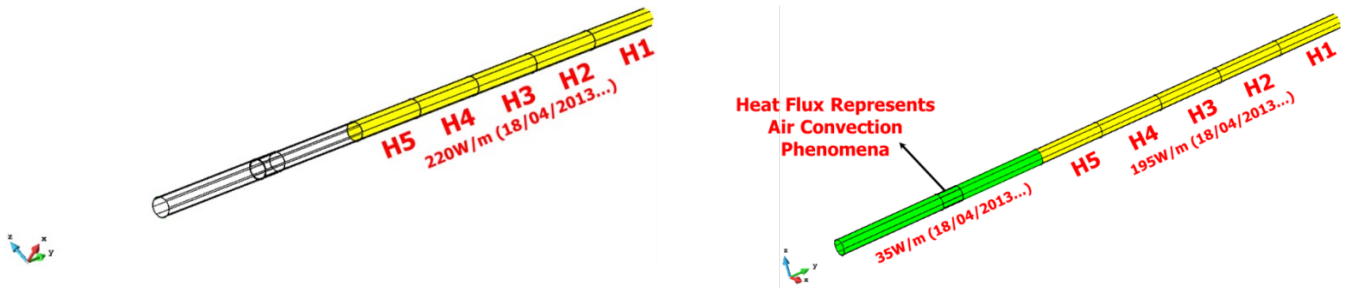

(a) (b)

Figure 4-12. Heat fluxes applied in the heating phase. a) Isolated heaters; b) Non-isolated heaters

4.4.3 Material Parameters

The thermal parameters of the Callovo-Oxfordian clay have been intensively investigated since 1990 by Andra (Andra, 2012). Table 4-1 compiles the values obtained in the laboratory for the thermal conductivity along and orthogonal to the bedding plane.

Table 4-1. Laboratory measurements of thermal conductivity in the Callovo-Oxfordian Clay in the TED area (Conil, Gatmiri and Armand, 2010).

		DBE	LAEGO
Thermal conductivity parallel to bedding	λ_{PL}[W/m/K]	1.96±0.07	1.89±0.05
Thermal conductivity perpendicular to bedding	λ_{PL}[W/m/K]	1.28±0.06	1.26±0.05

A specific heat equal to 1025 J/kgK for the saturated material (corresponding to a specific heat equal to 800 J/kgK for the solid phase) has been assigned to the host rock.

As discussed in part 4.1, values of the thermal conductivity along the bedding plane and orthogonal to it have been back-analysed to match temperatures at all the sensors. Values used for the final modelling are indicated in Table 4-2. They are 2.5% higher than the reference values (2 and 1.33 W/m/K, respectively) and within the range of values measured experimentally (Table 4-1).

The thermal parameters of the steel lining and gap are reported in Table 4-2. The low value of thermal conductivity assigned to the gap correspond to the air at 100 kPa.

Table 4-2. Reference parameters of the Callovo-Oxfordian clay adopted in the simulations

Properties	Parameters	Symbol	Value	Units
Physical	Porosity	ϕ	15	%
Thermal	Thermal Conductivity	$\lambda_{//}$	2.05	W/m/K
		$\lambda_{\perp}$	1.33	W/m/K
	Specific heat of solid	Cs	800	J/kg/K

Table 4-3. Reference parameters of the gaps and steel lining adopted in the simulations

	Porosity	Thermal Conductivity (W/m/K)	Specific heat of solid (J/kg/K)
Gaps	0.98	0.35	1100
Steel lining	0.01	80	550

4.4.4 Short overview of some numerical results

Before presenting in the next section a thorough comparison between computed and measured temperatures at all sensors, some aspects of the model are briefly discussed in this paragraph.

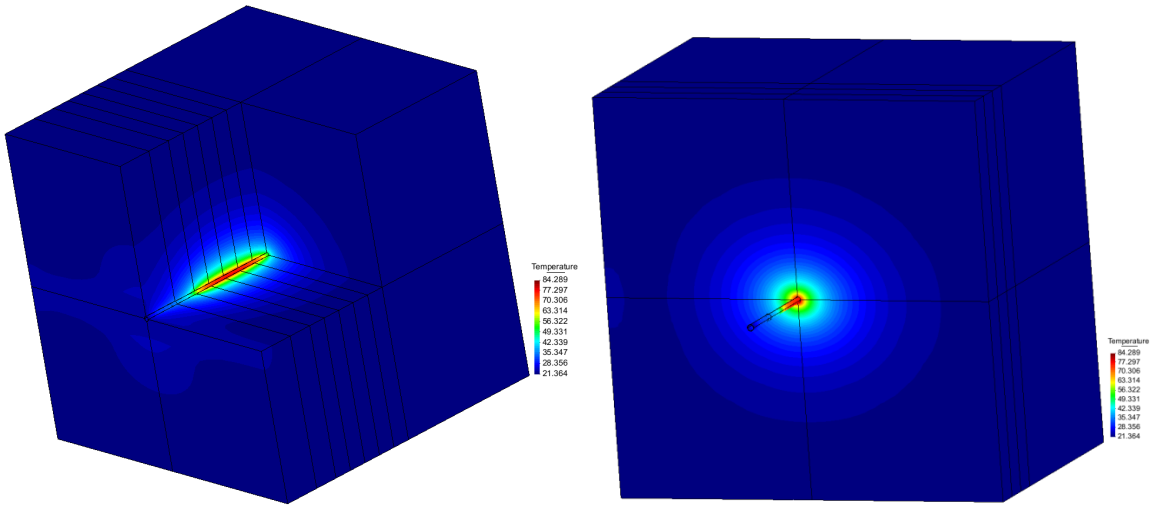

Figure 4-13. Three-dimensional view of computed contours of equal temperature at the end of the computation.

The first aspect concerns the anisotropic character of the thermal field. Figure 4-13a shows a three-dimensional intersection of the temperature bulb with three planes: 1) a horizontal plane passing through the centreline of the alveolus; 2) a vertical plane passing through the centreline of the alveolus and 3) a vertical plane orthogonal to the alveolus and passing through the end of heater. Figure 4-13b show the contour map of temperature iso-values for a vertical plane orthogonal to the alveolus and passing through the middle of the heaters. One can observe in the two figures the elliptical shape of the temperature bulb in the vertical plane.

The second aspect concerns the slight eccentricity of the temperature bulb due to the contact existing between the steel lining and the host rock at the bottom of the alveolus. Figure 4-14 shows a zoom of Fig. 4-13b close to the alveolus. One can appreciate that the width of the heated zone is slightly higher below the alveolus than on top of it.

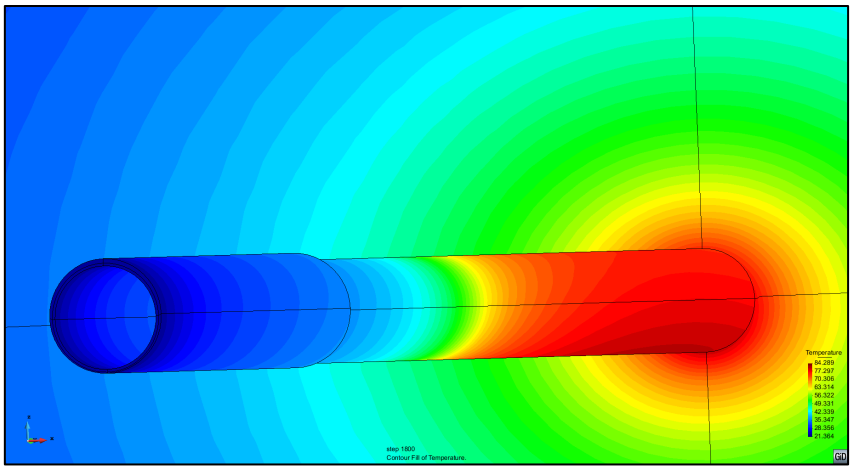

Figure 4-14. Three-dimensional view of computed contours of equal temperature in the steel casings. High temperature is obtained at the bottom of the heated zone due to the geometry of the gap.

The third aspect concerns the distribution of temperatures with and without application of a heat flux within the non-heated zone. Figure 4-15 shows the bulb of temperatures in both cases. Figure 4-16 shows a comparison of both models against temperatures measured in front of the non-heated zone (sensors ALC1616_TEM_05 and ALC1633_TEM_05) while Fig. 4-17 shows the same in front of the heated zone. In both cases, the discontinuous line corresponds to the model with heat flow applied in the non-heated zone. It fits much better the measurements than the model without heat flow (continuous line).

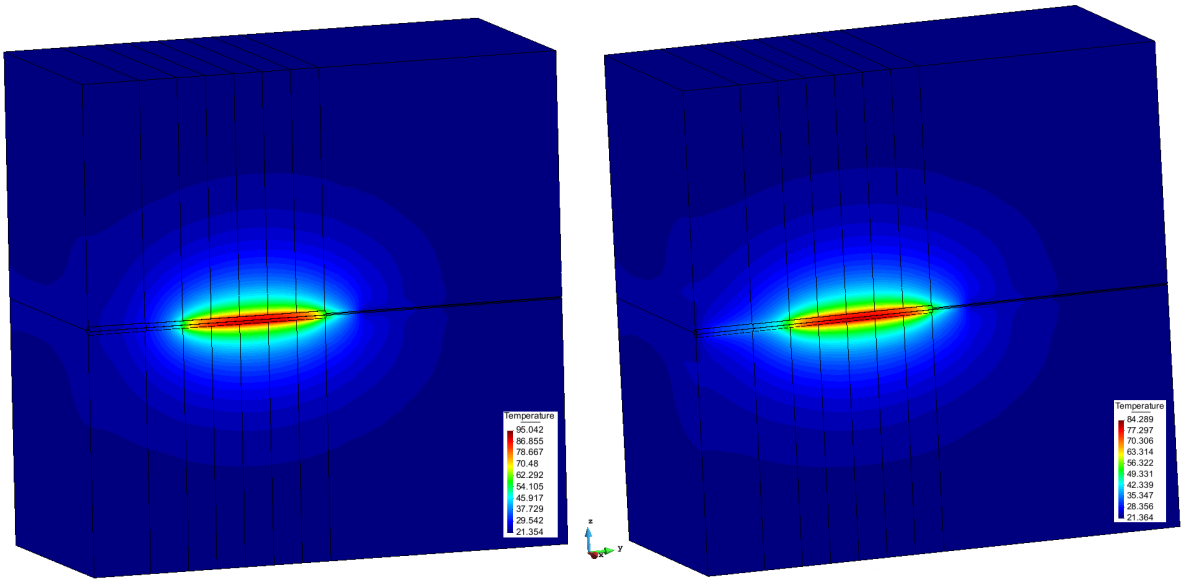

Figure 4-15. Three-dimensional view of computed contours of equal temperature at the end of the computation. Right: input power applied only in the heaters and left: input power applied according to the heat distribution in the alveolus.

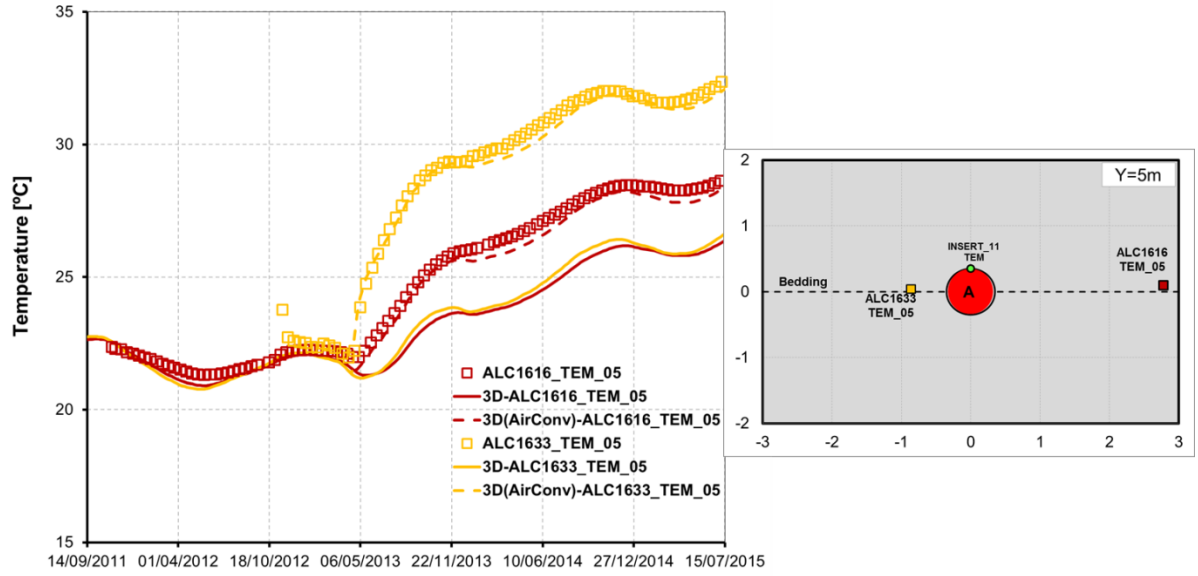

Figure 4-16. Temperature evolution of sensors located on the same section as the heaters (5 m deep from the gallery). The measurements (dots) are compared with the simulation (lines).

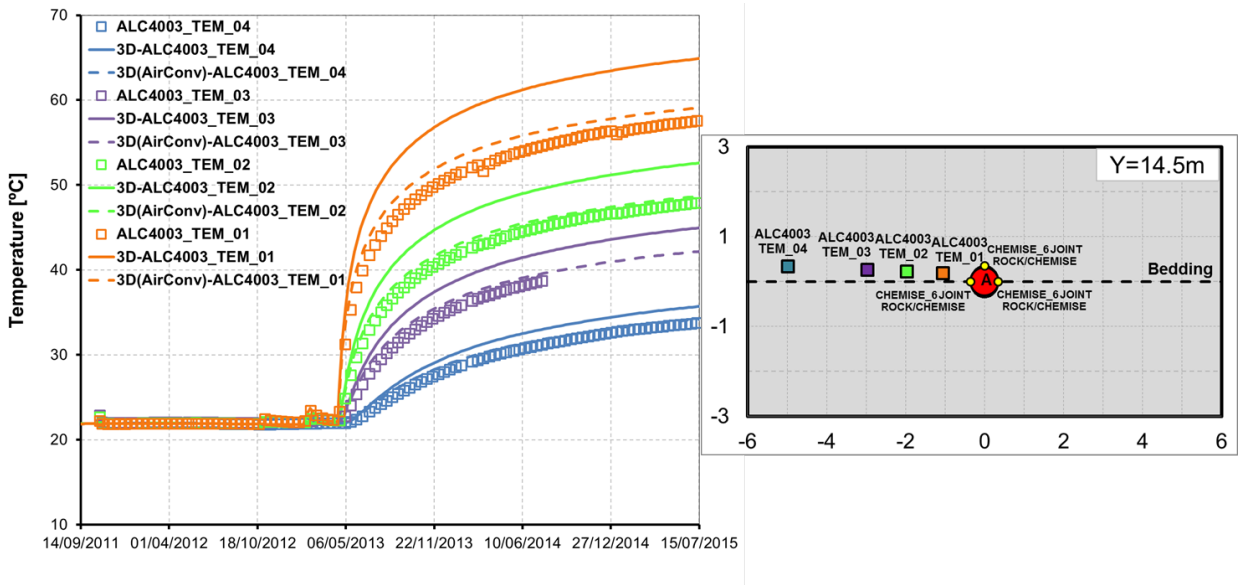

Figure 4-17. Temperature evolution of sensors located on the same section as the heaters (14.5 m deep from the gallery). The measurements (dots) are compared with the simulation (lines).

4.5 Comparison between simulation and measurements

This part contains the comparison between the numerical results of the final three-dimensional modelling (including heat flow within the non-heated zone) and the measurements at all the sensors in the host rock, on the steel lining and within the gap. Results are organized in two types of figures:

- Comparisons of temperature time evolution at all the sensors within specific vertical cross-sections orthogonal to the alveolus and located at Y = 3, 4, 4.5, 5, 10, 13, 13.6 14.5 and 17.5 m form the head of the alveolus at GAN gallery (Figure 4-19 - Figure 4-28).
- Comparisons of temperature time evolution and temperature profiles for all the sensors belonging to specific boreholes: ALC1616, ALC1617, ALC1618, ALC1633, ALC4001, ALC4002, ALC4003, ALC4004 and ALC4005 (Figure 4-29 - Figure 4-43).

A good agreement can be observed for all the measurements.

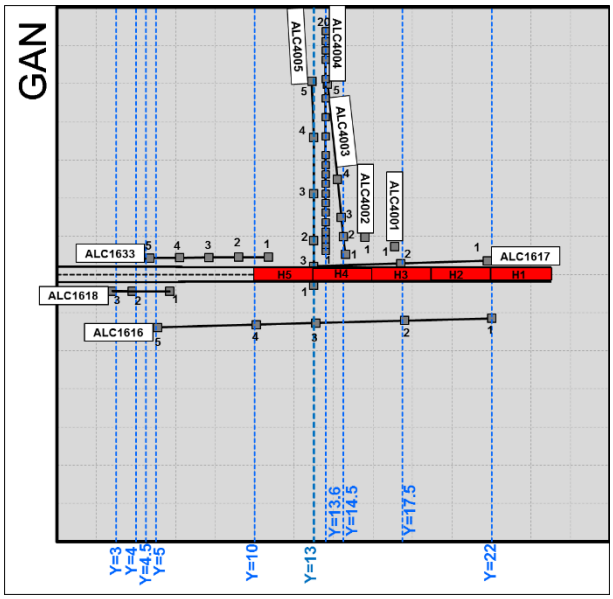

Figure 4-18. Horizontal view (bedding plane) of the instrumentation boreholes and perpendicular cross-sections.

4.5.1 Comparisons in sections perpendicular to the alveolus

Section Y=3m

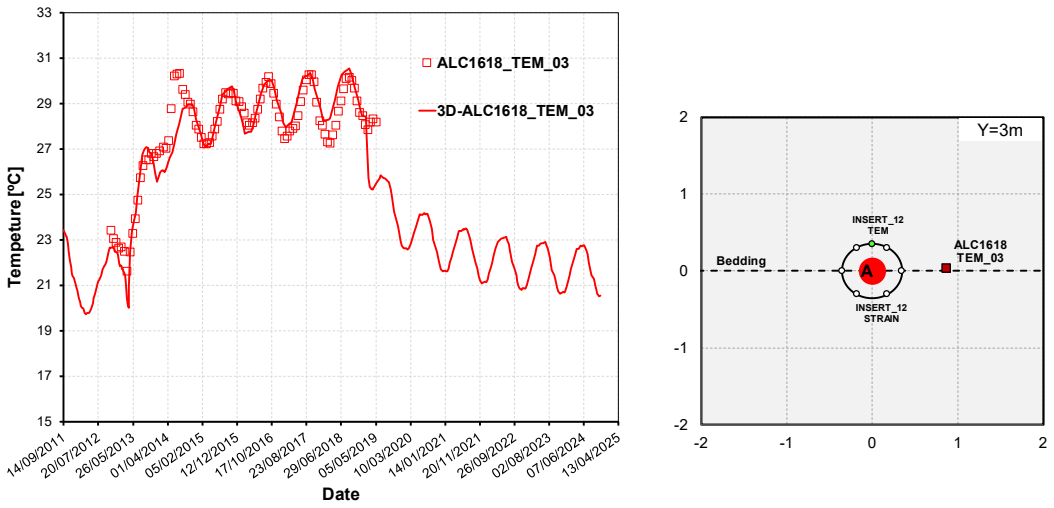

Figure 4-19. Temperature evolution at sensors located within the section at 3 m from the gallery. The measurements (dots) are compared with the simulation (lines).

Section Y=4m

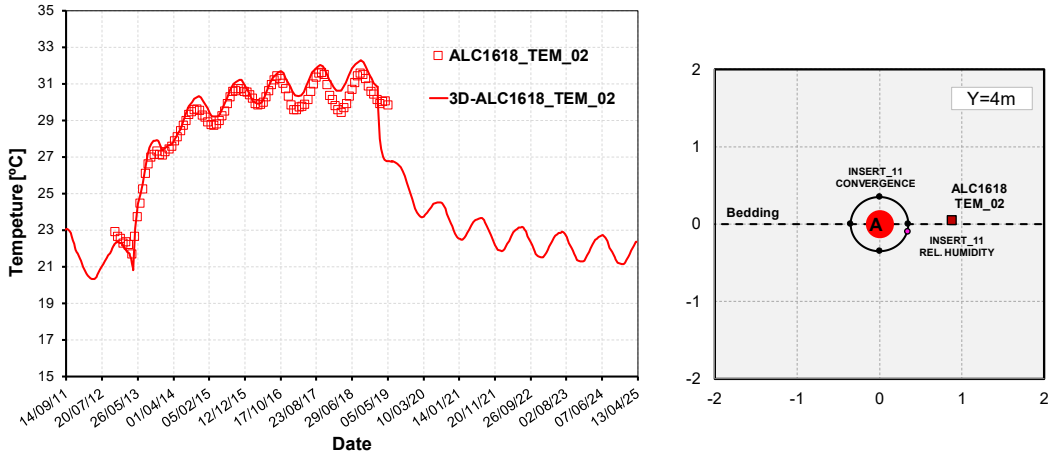

Figure 4-20. Temperature evolution at sensors located within the section at 4 m from the gallery. The measurements (dots) are compared with the simulation (lines).

Section Y=4.5m

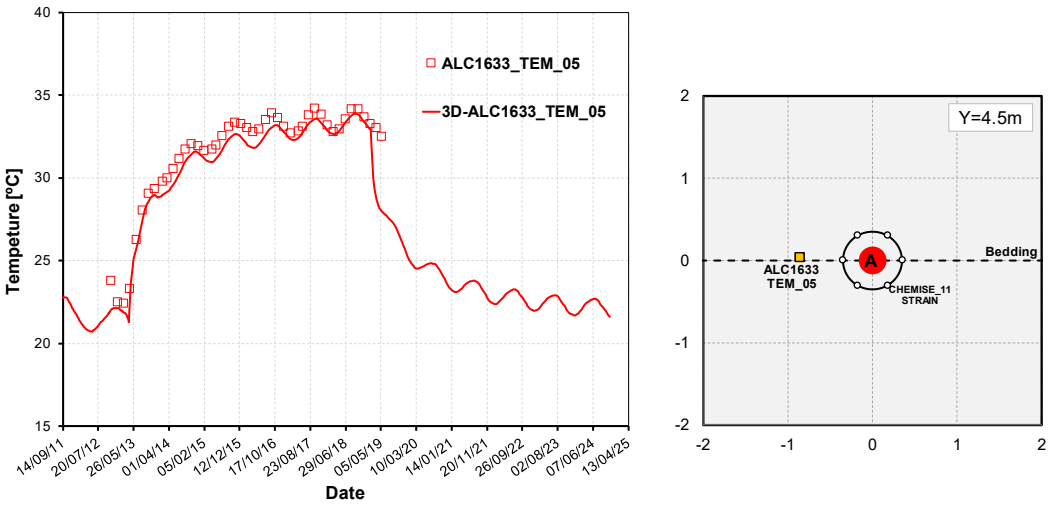

Figure 4-21. Temperature evolution at sensors located within the section at 4.5 m from the gallery. The measurements (dots) are compared with the simulation (lines).

Section Y=5m

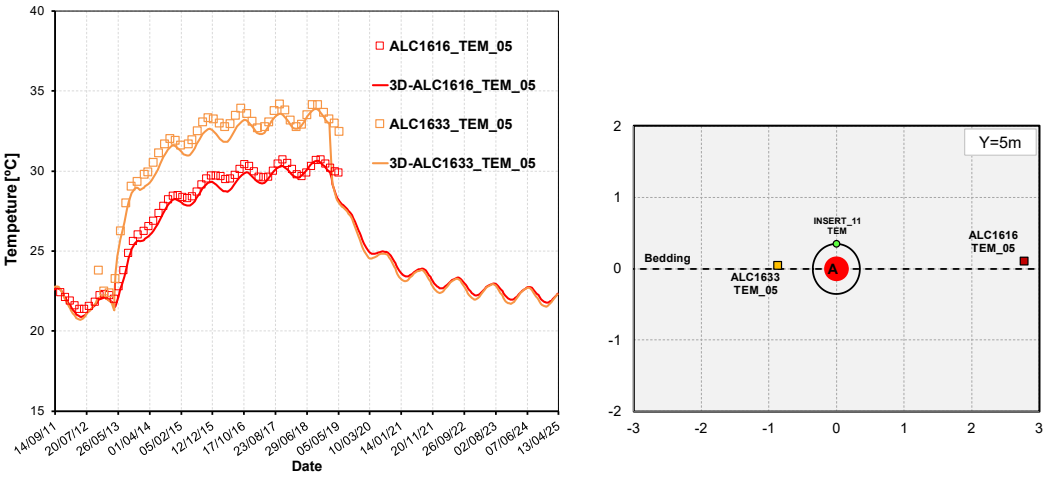

Figure 4-22. Temperature evolution at sensors located within the section at 5 m from the gallery. The measurements (dots) are compared with the simulation (lines).

Section Y=10m

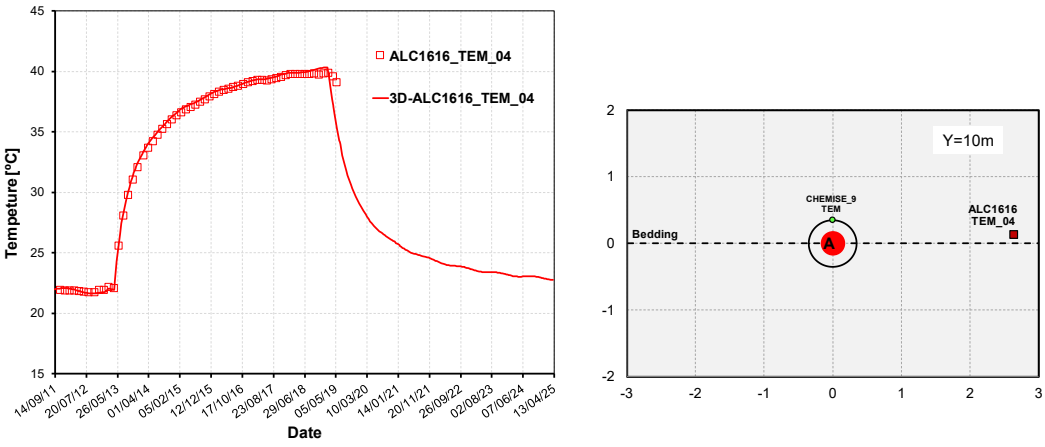

Figure 4-23. Temperature evolution at sensors located within the section at 10 m from the gallery. The measurements (dots) are compared with the simulation (lines).

Section Y=13m

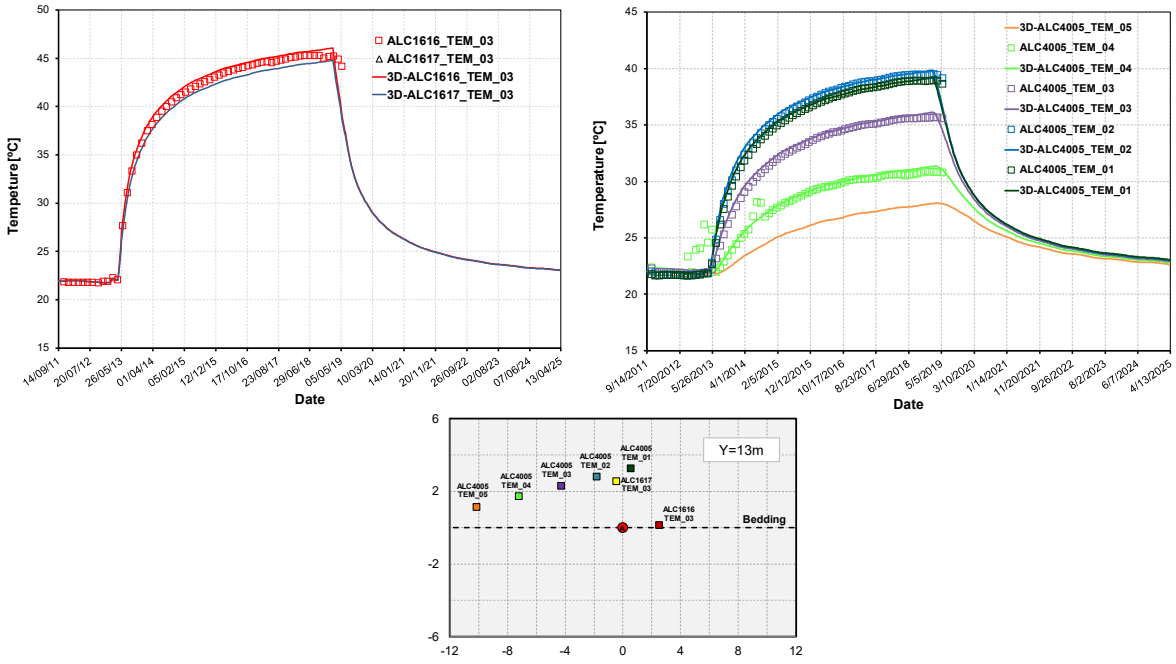

Figure 4-24. Temperature evolution at sensors located within the section at 13 m from the gallery. The measurements (dots) are compared with the simulation (lines).

Section Y=13.6m

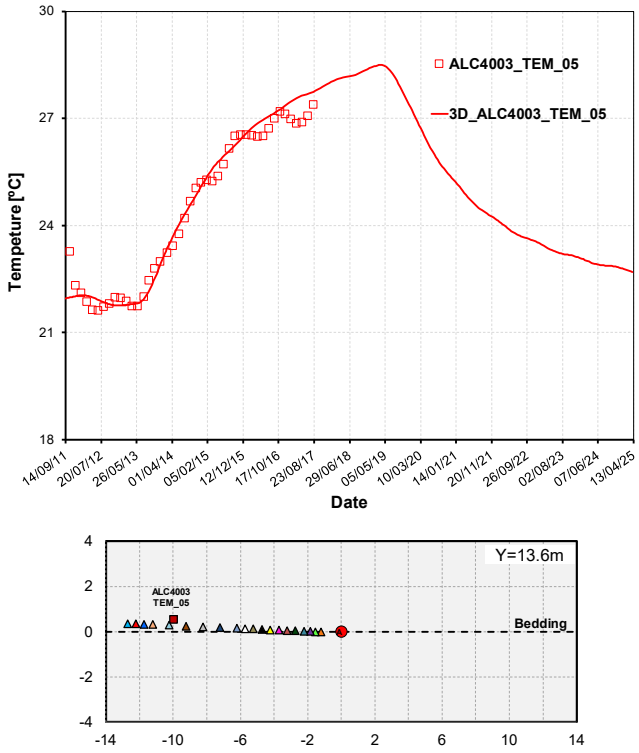

Figure 4-25. Temperature evolution at sensors located within the section at 13.6 m from the gallery. The measurements (dots) are compared with the simulation (lines).

Section Y=14.5m

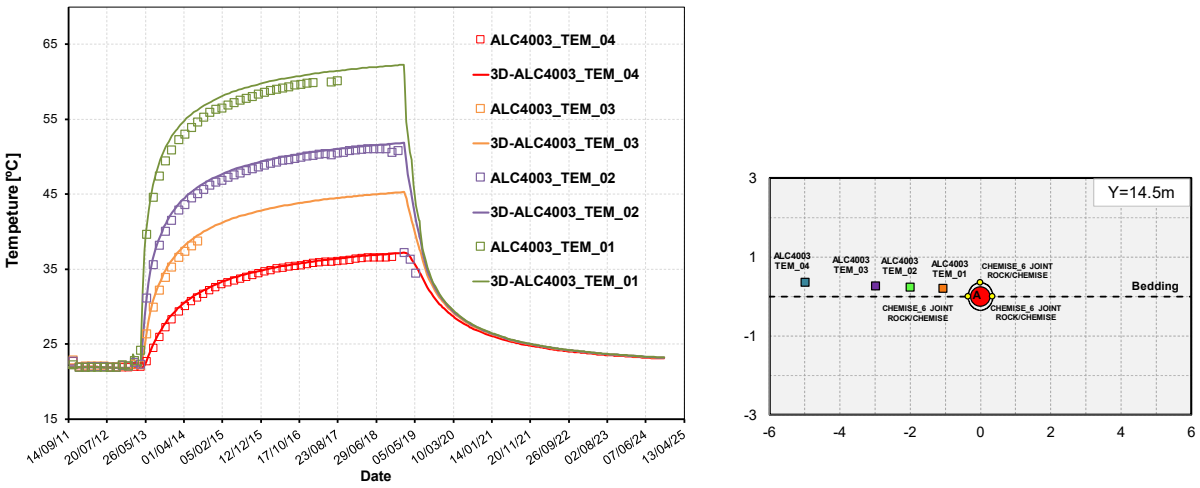

Figure 4-26. Temperature evolution at sensors located within the section at 14.5 m from the gallery. The measurements (dots) are compared with the simulation (lines).

Section Y=17.5m

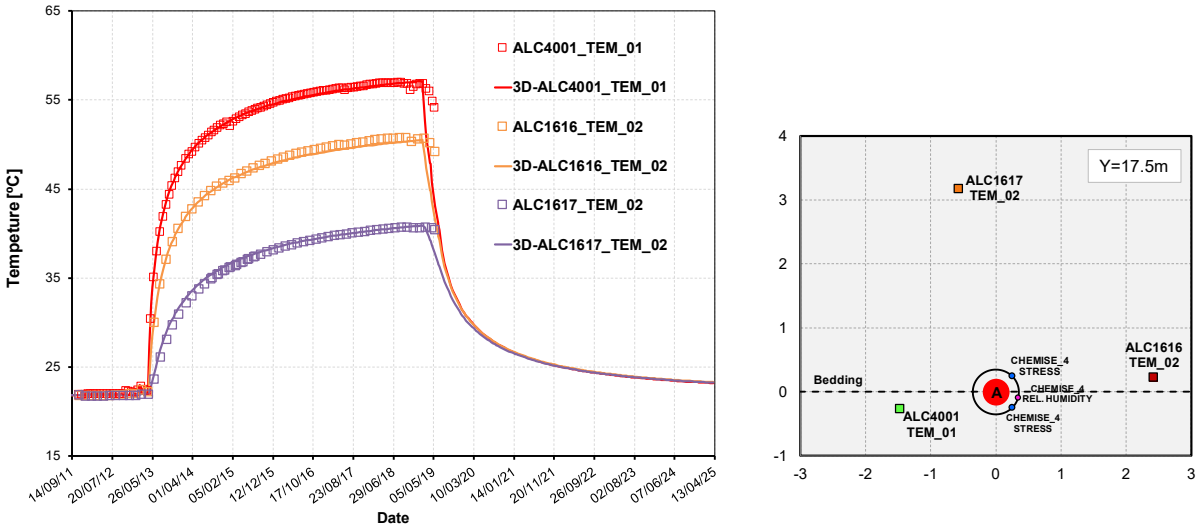

Figure 4-27. Temperature evolution at sensors located within the section at 17.5 m from the gallery. The measurements (dots) are compared with the simulation (lines).

Section Y=22m

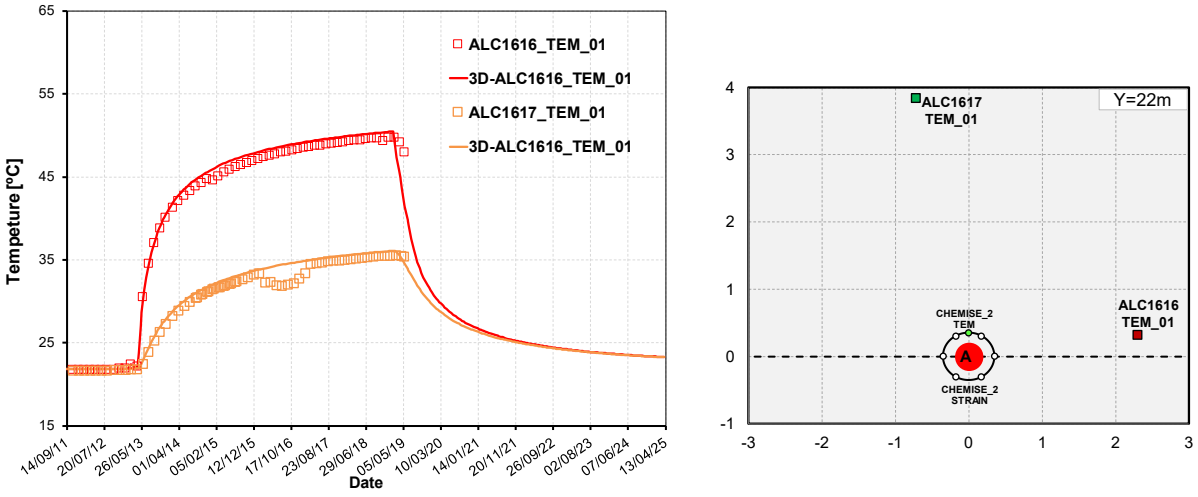

Figure 4-28. Temperature evolution at sensors located within the section at 22 m from the gallery. The measurements (dots) are compared with the simulation (lines).

4.5.2 Comparisons along boreholes

Borehole ALC1616

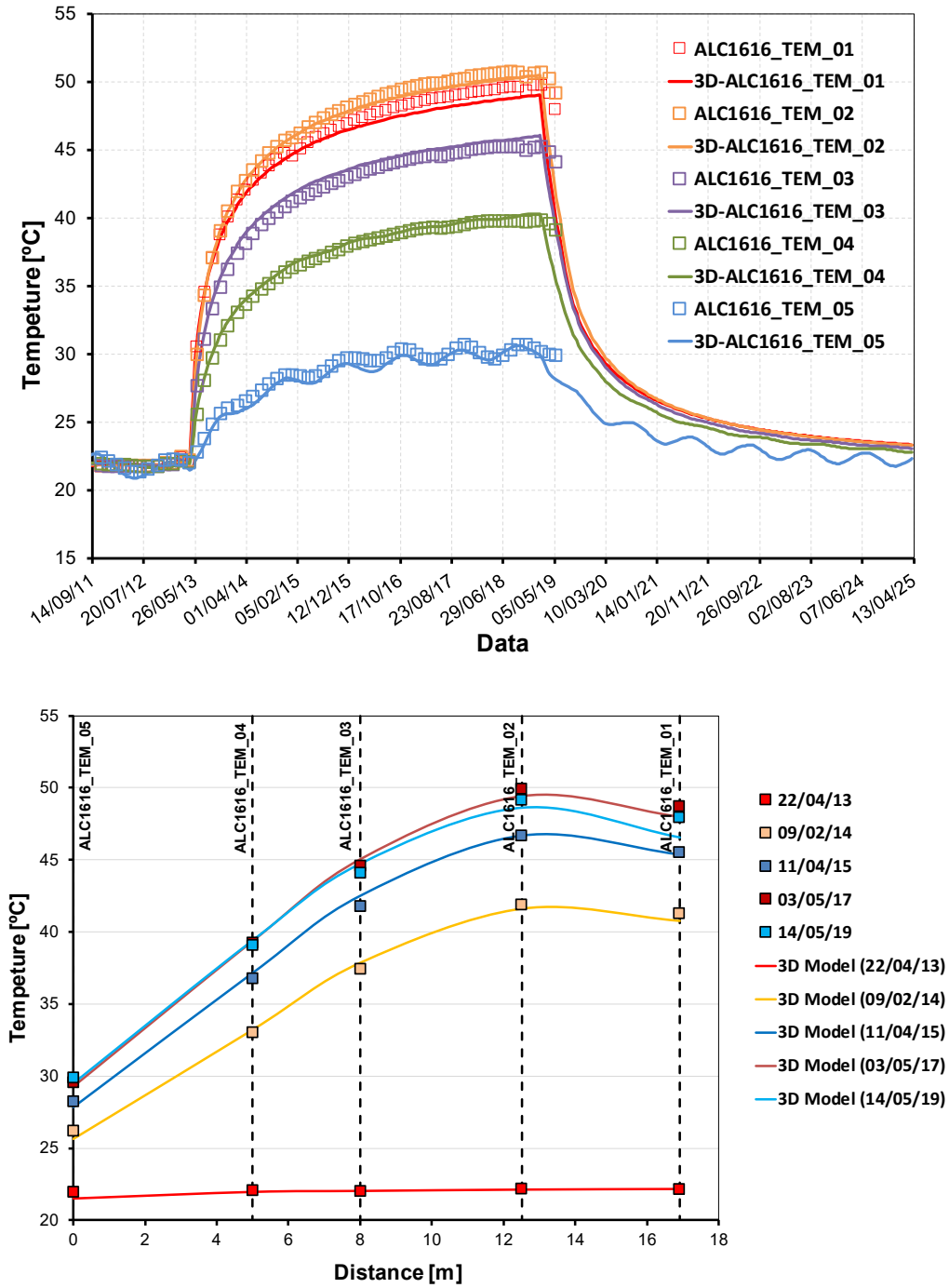

Figure 4-29. Temperature a) time evolution and b) profiles at sensors along borehole ALC1616. The measurements (dots) are compared to the simulation results (lines).

Borehole ALC1617

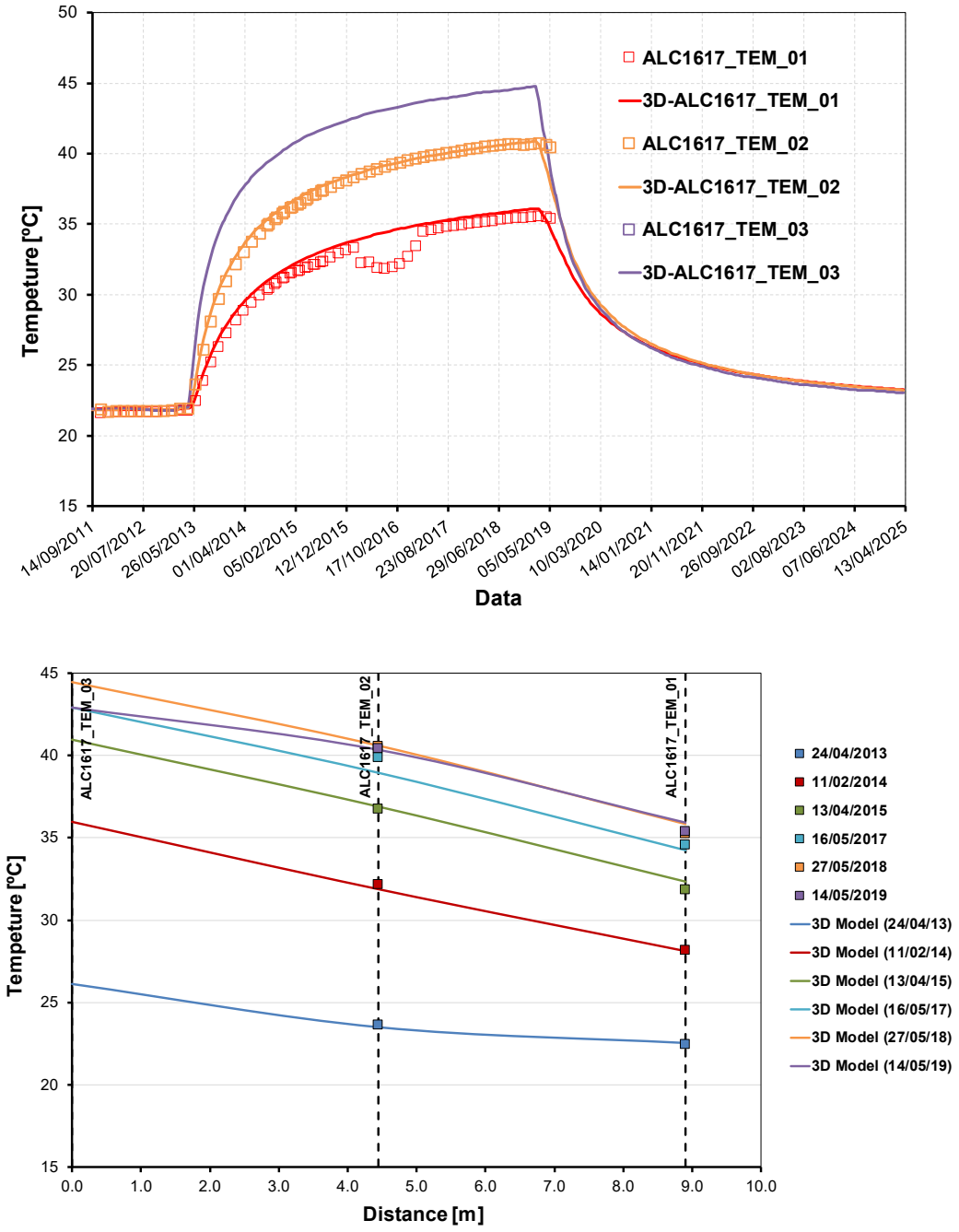

Figure 4-30. Temperature a) time evolution and b) profiles at sensors along borehole ALC1617. The measurements (dots) are compared to the simulation results (lines).

Borehole ALC1618

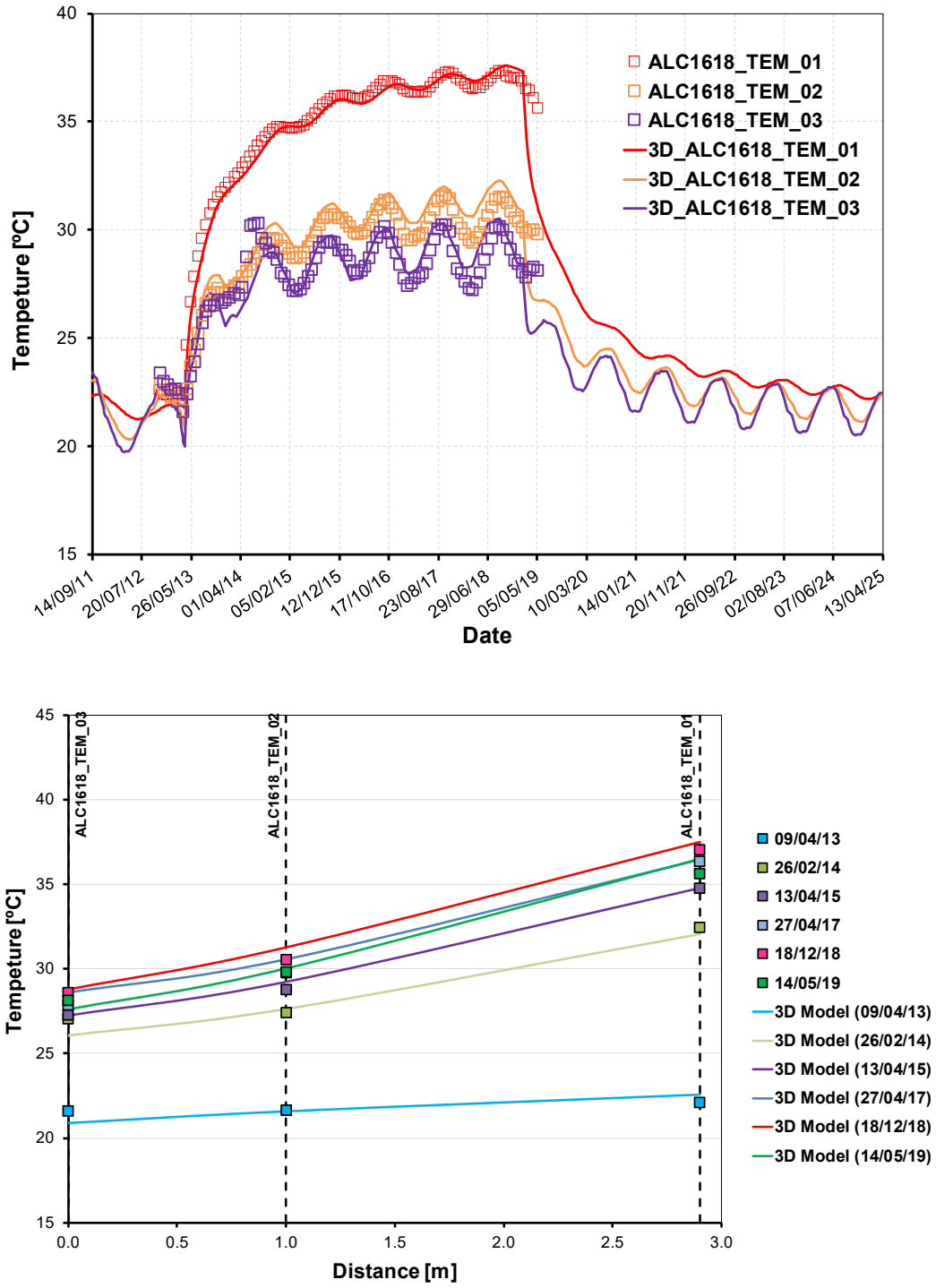

Figure 4-31. Temperature a) time evolution and b) profiles at sensors along borehole ALC1618. The measurements (dots) are compared to the simulation results (lines).

Borehole ALC1633

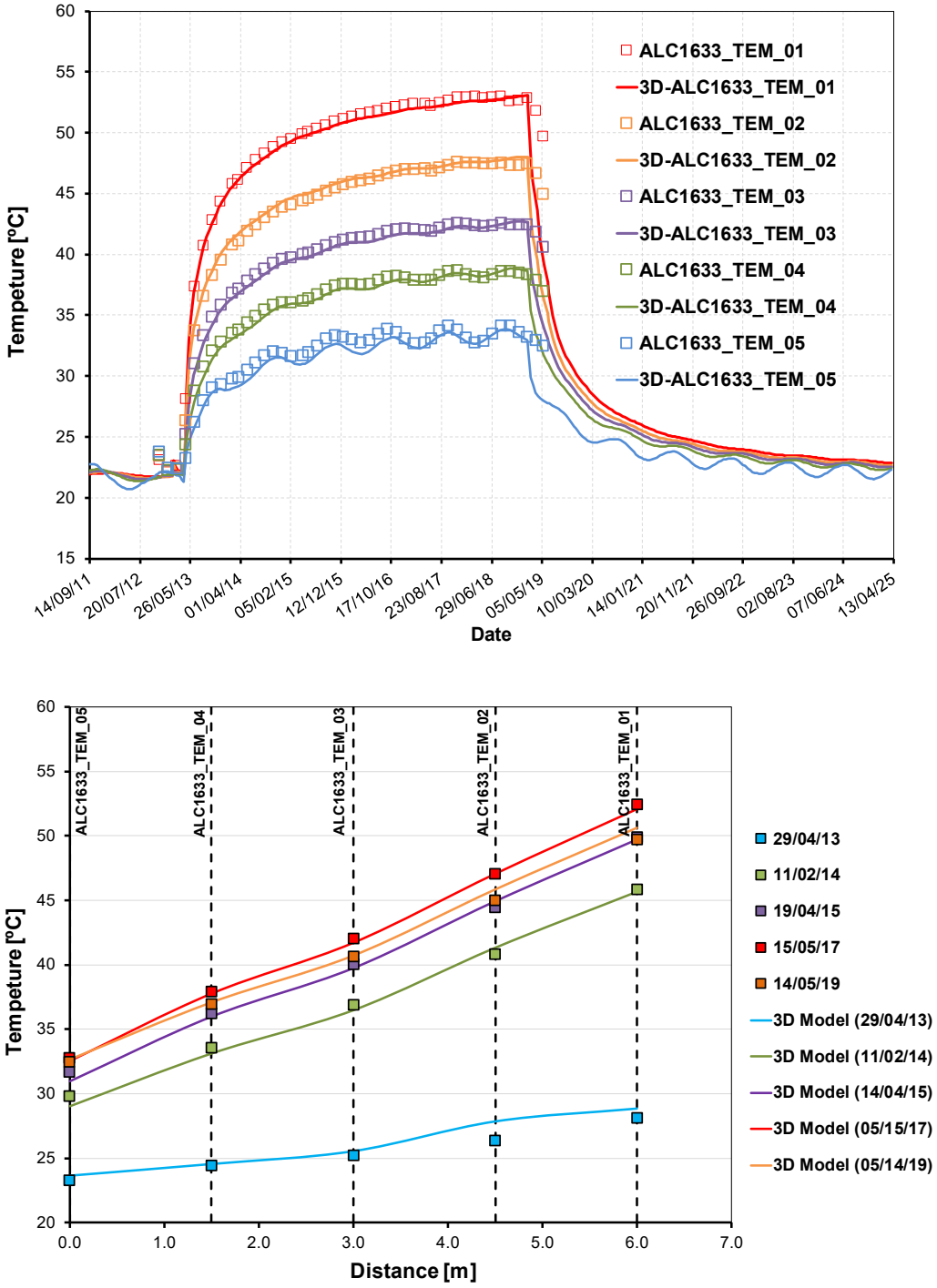

Figure 4-32. Temperature a) time evolution and b) profiles at sensors along borehole ALC1633. The measurements (dots) are compared to the simulation results (lines).

Borehole ALC4003

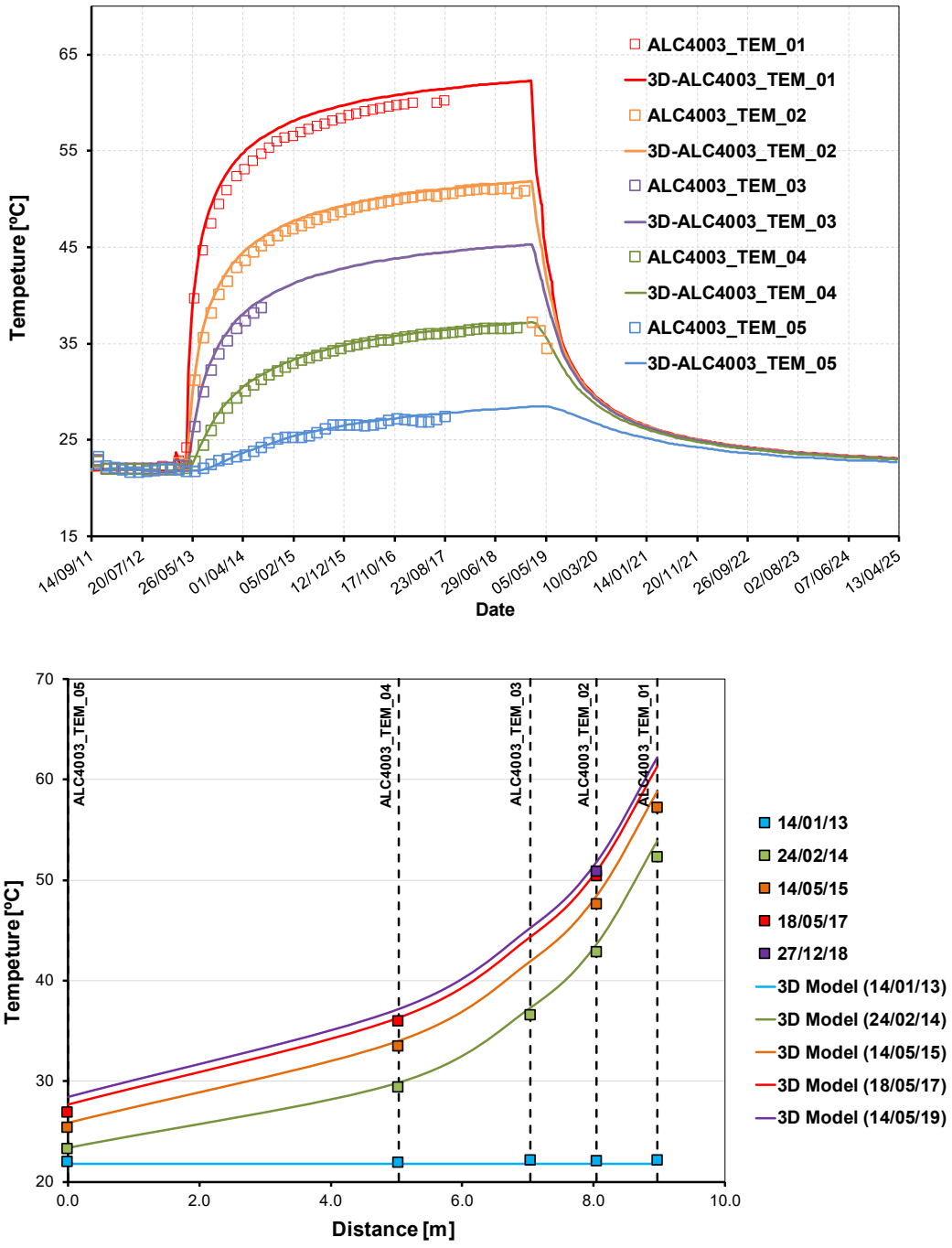

Figure 4-33. Temperature a) time evolution and b) profiles at sensors along borehole ALC4003. The measurements (dots) are compared to the simulation results (lines).

Borehole ALC4005

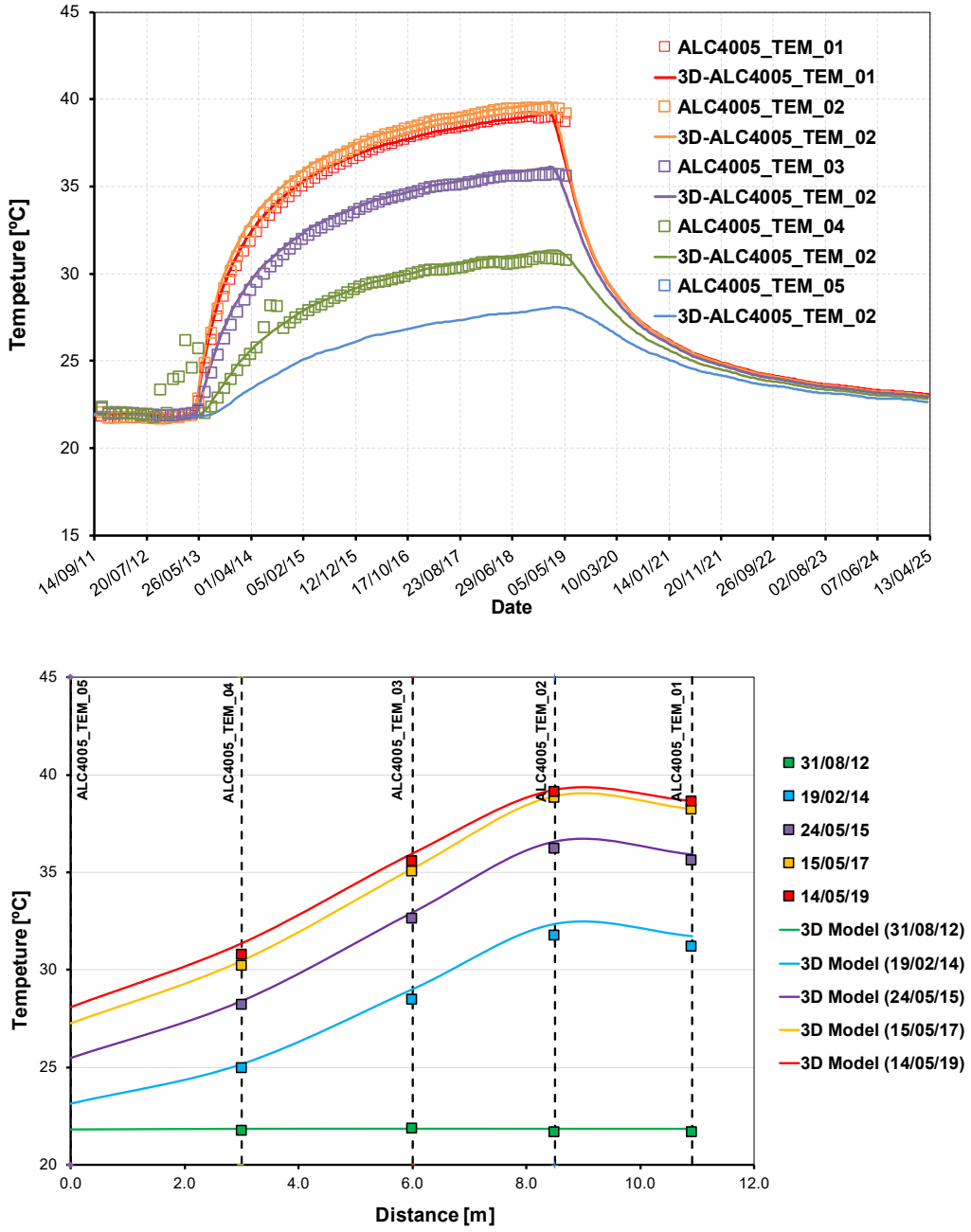

Figure 4-34. Temperature a) time evolution and b) profiles at sensors along borehole ALC4005. The measurements (dots) are compared to the simulation results (lines).

Borehole ALC4001

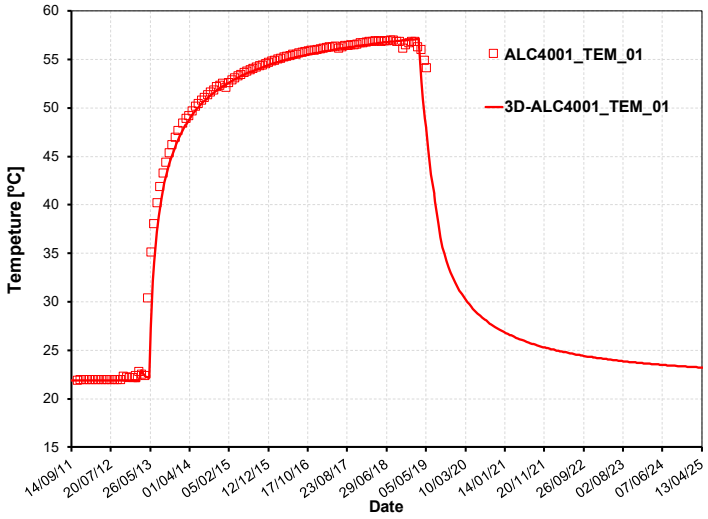

Figure 4-35. Temperature a) time evolution and b) profiles at sensors along borehole ALC4001. The measurements (dots) are compared to the simulation results (lines).

5.5.3 Comparison on the steel lining

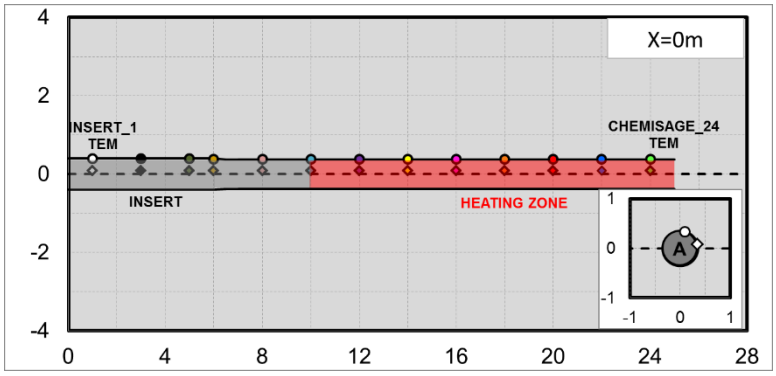

Figure 4-36. Temperature sensor located at steel casings.

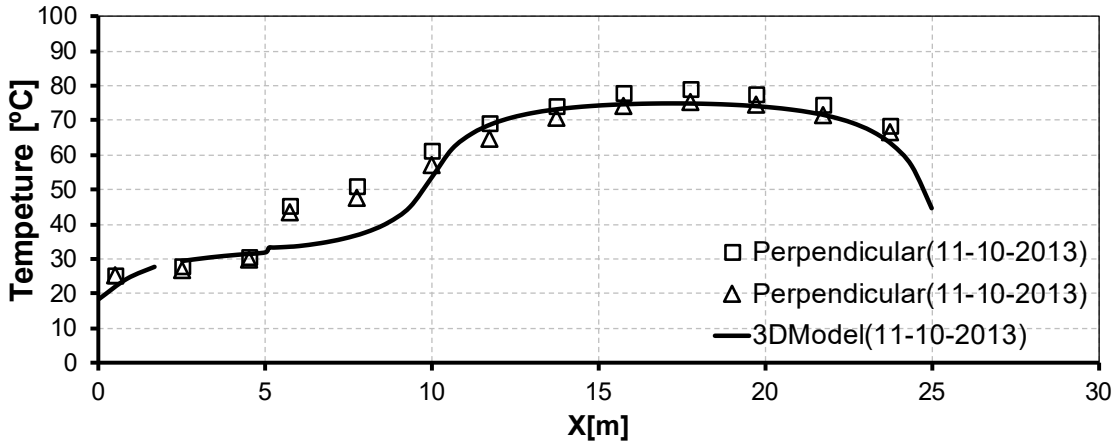

(a)

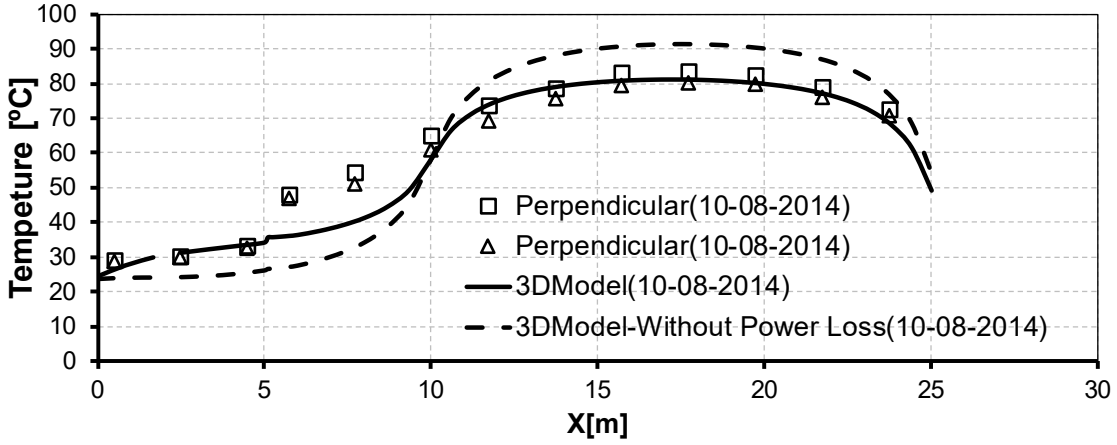

(b)

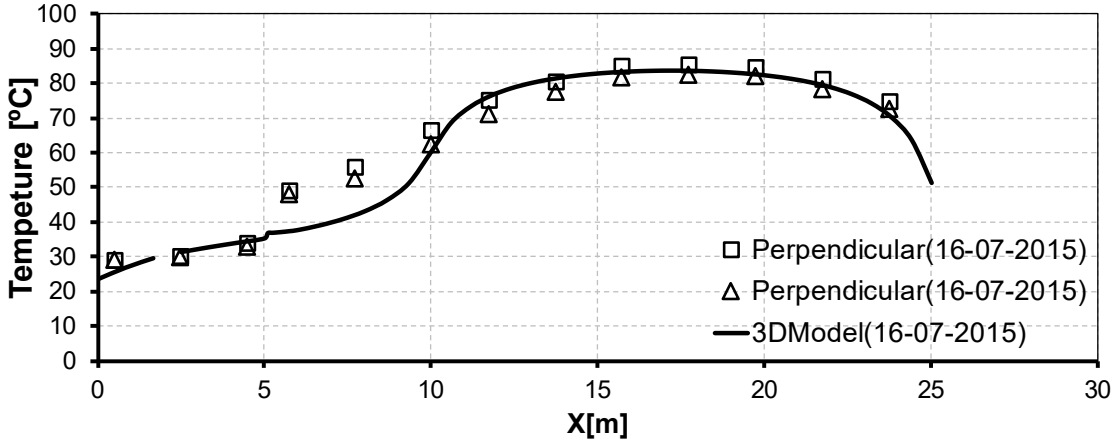

(c)

Figure 4-37 Temperature profile on steel lining. The graph (b), 10 August 2014, shows the comparison with a model in which the heated zone is isolated (dot line). The measurements (dots) are compared to the simulation results (lines).

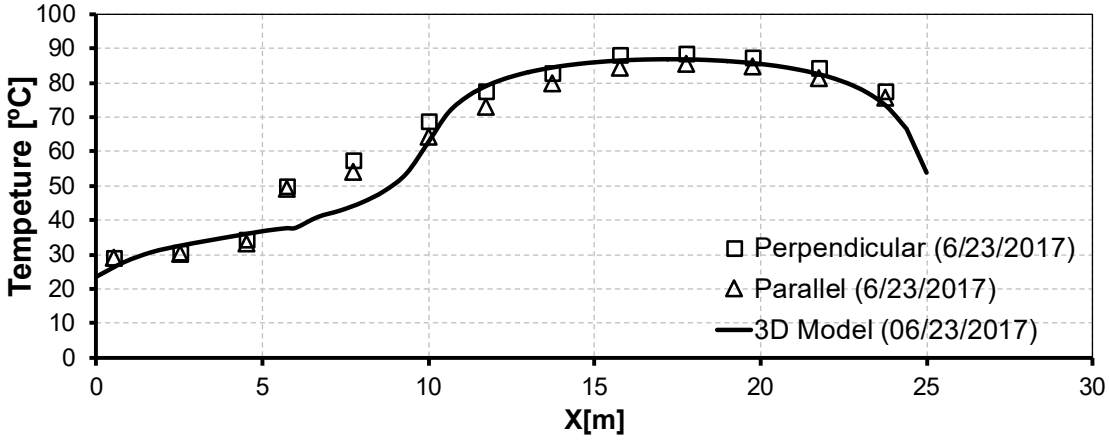

(a)

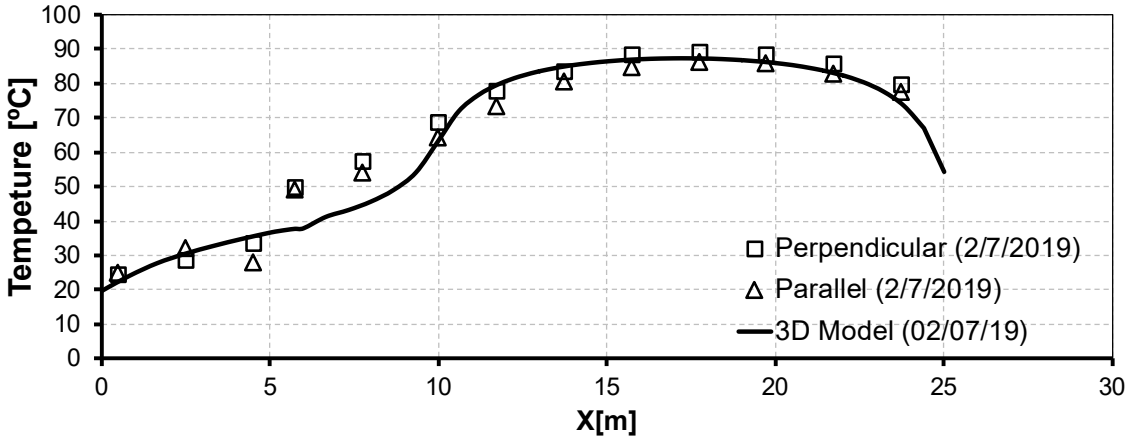

(b)

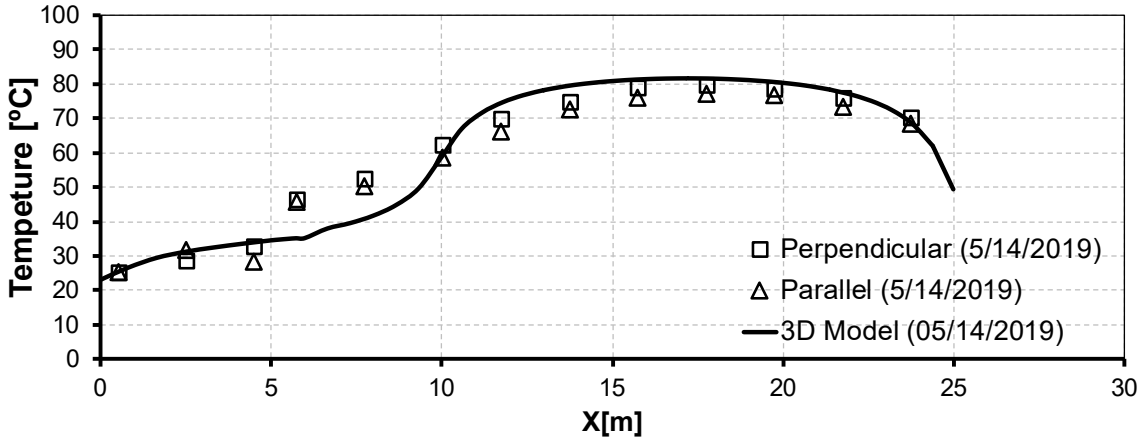

(c)

Figure 4-38. Temperature profile on steel lining. The graph (b), 10 August 2014, shows the comparison with a model in which the heated zone is isolated (dot line). The measurements (dots) are compared to the simulation results (lines).

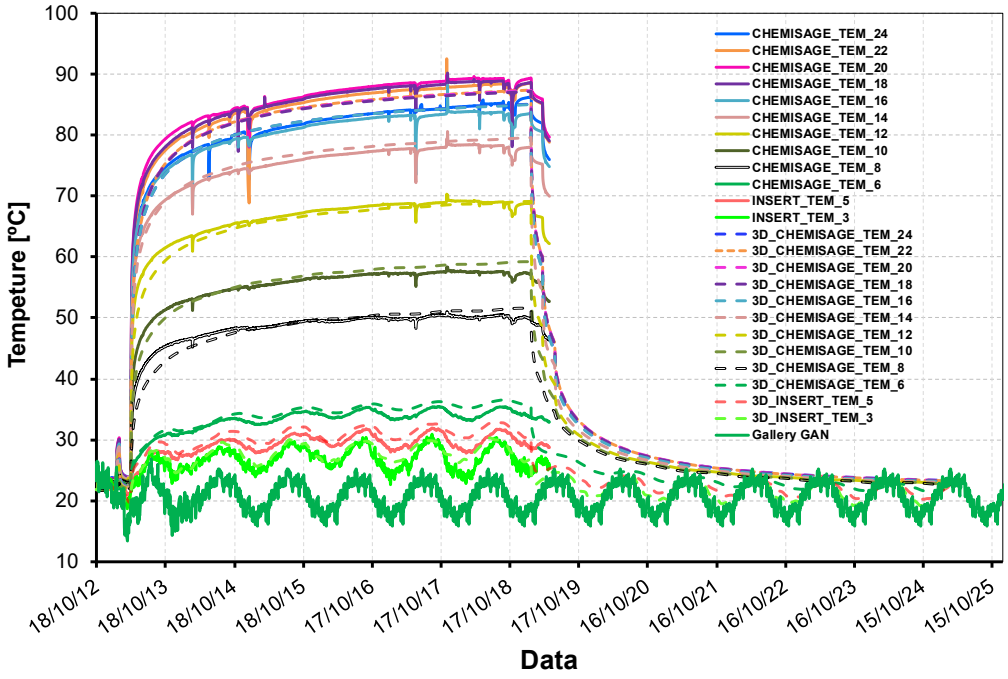

Figure 4-39. Temperature evolution of the vertical sensors at steel casing. The measurements (lines) are compared to the simulation results (dotted lines).

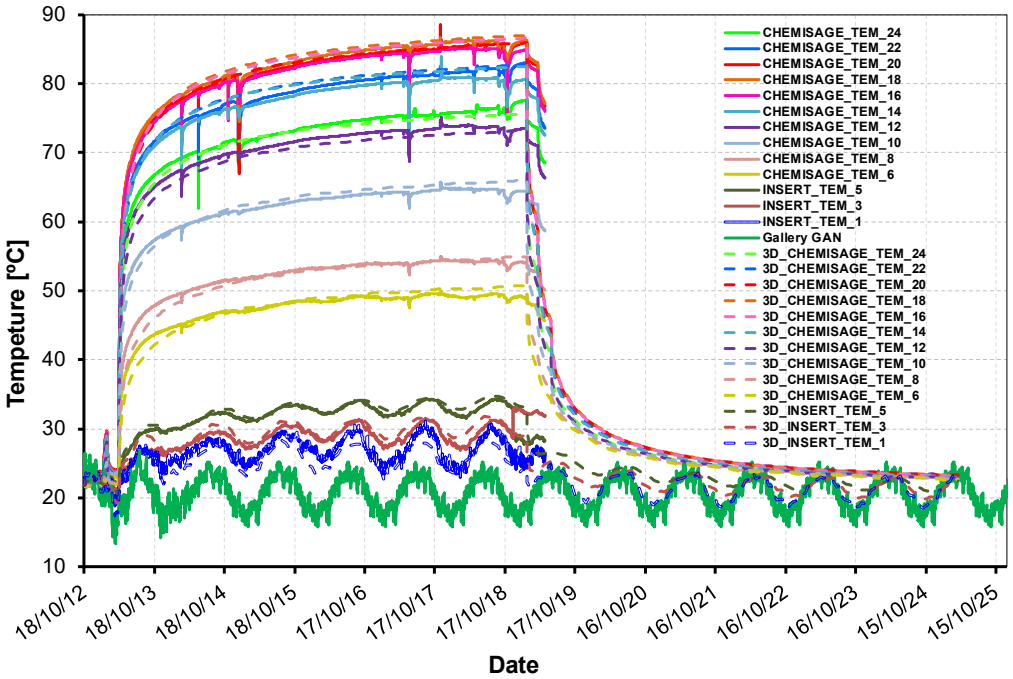

Figure 4-40. Temperature evolution at the lateral sensors on steel lining. The measurements (lines) are compared to the simulation results (dotted lines).

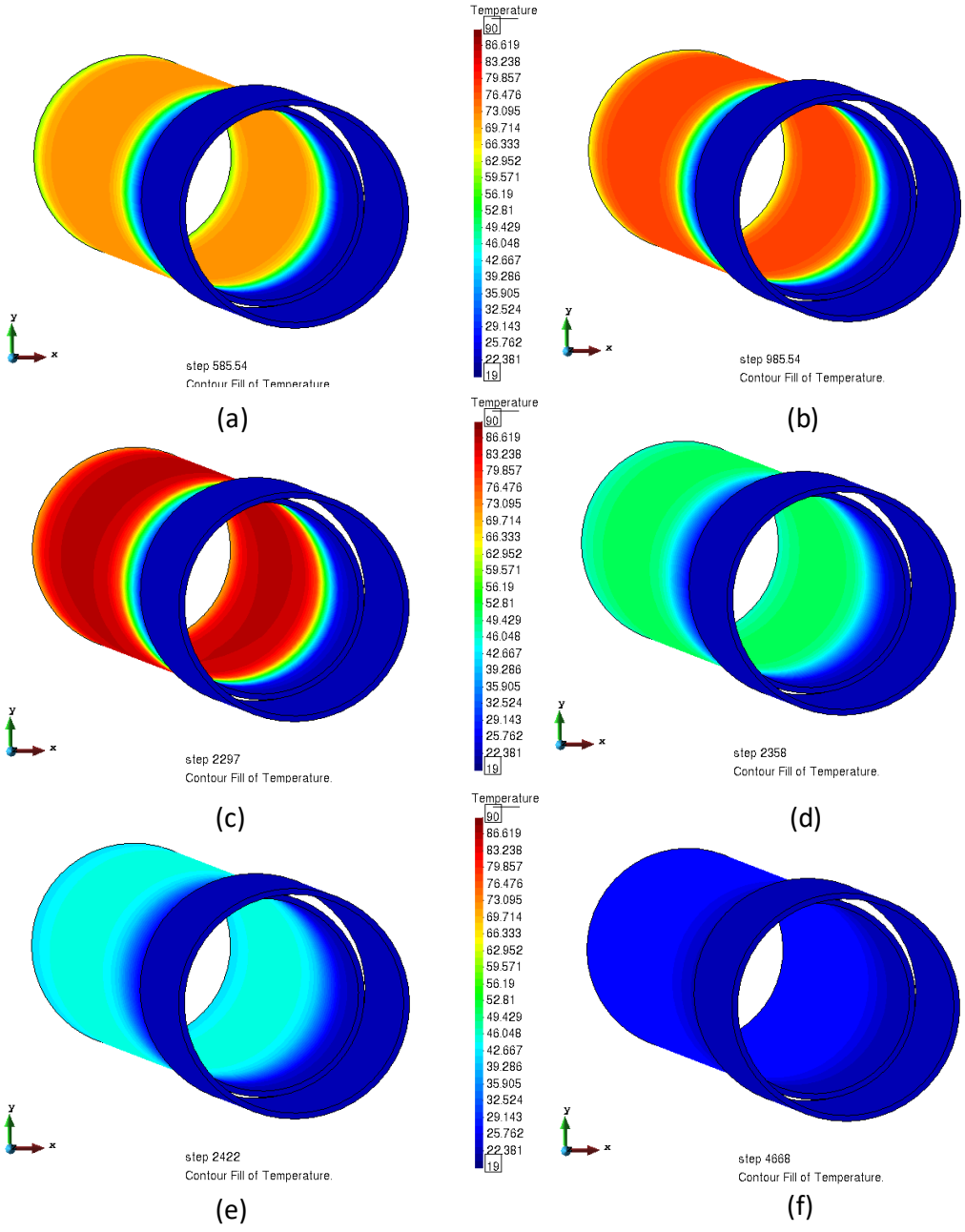

Figure 4-41 3D view of computed contours of equal temperature for (a) 585 days (one-year heating); (b) 985 days (two years heating); (c) 2297 days (end of heating phase); (d) 2358 days (end of first cooling phase) ; (d) 2422 days (end of second cooling phase) ; (d) 4668 days (6 years cooling).

4.5.3 Joint temperature measurement and simulations

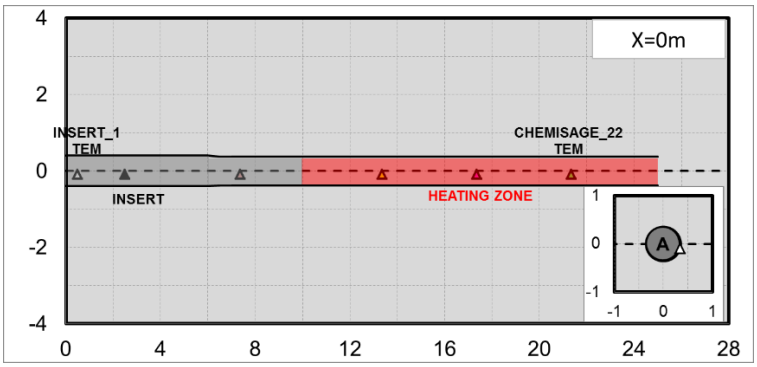

Figure 4-42. Temperature sensor located at the gap between steel casings and COx.

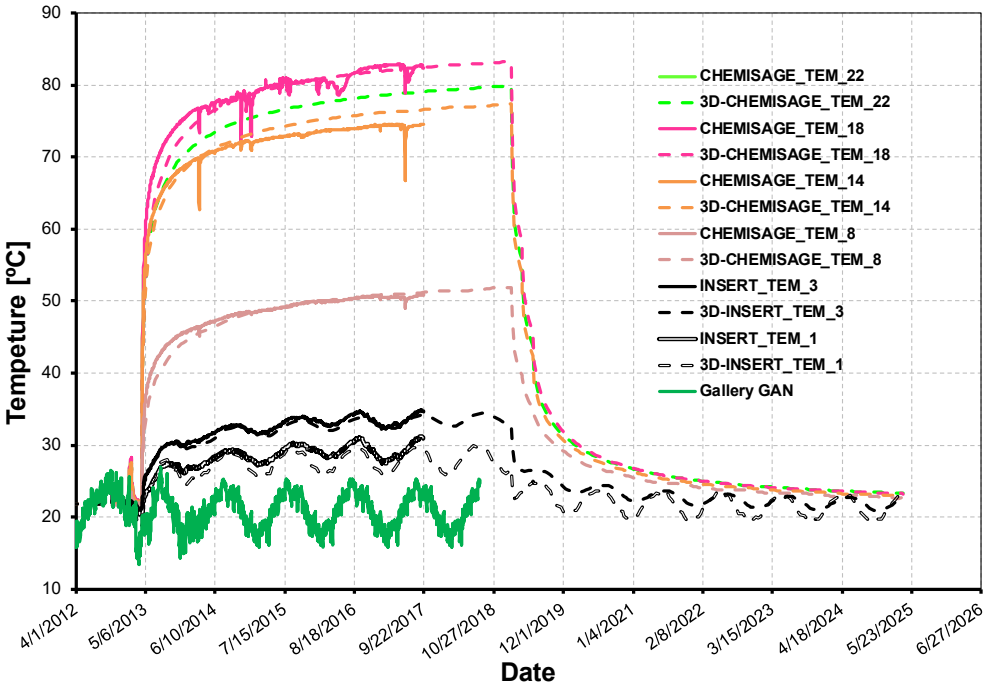

Figure 4-43. Temperature evolution of the sensors at the gap. The measurements (lines) are compared to the simulation results (dotted lines).

5. Analysis of the thermo-hydro-mechanical behaviour

This section presents the thermo-hydro-mechanical modelling of the HA-ALC1604 experiment. After a short description of the evolution of pore pressures registered by the sensors around the experiment (section 5.1), the model itself is presented (section 5.2). It corresponds to the final 3D model carried out of the work, which includes most of experiment geometrical features (host rock, alveolus, insert, steel lining and the gaps between the steel lining and the host in the operative zone, the steel lining and the insert and the insert and the host rock in the alveolus head), includes the thermo-hydraulic influence of the surrounding GAN and GRD gallery, as well as all experiment phases since the excavation of the alveolus (included). Section 5.3 presents the comparison of numerical results with all experiment measurements: temperatures, pore pressures, sleeve convergences and mechanical signatures. In some figures, results of the 3D model is compared with those output by a 2D model focusing a two vertical cross sections orthogonal to the alveolus, to emphasize the importance of three dimensional effects.

5.1 Description of the pore pressure field

As described in Section 2, there are 18 piezometers installed in the rock mass to monitor the pore pressure evolution (Figure 5-1).

- Two boreholes with one piezometer chamber (ALC4001 and ALC 4002),
- Two boreholes with three piezometer chambers (ALC1617 and ALC1618),
- Two boreholes with five piezometer chambers associated with temperature sensors to measure the pressure gradient from the gallery into the rock mass and the pressure evolution near to the heated zone. (ALC4005 and ALC 1616).

These boreholes are backfilled with resin in order to ensure that they are impervious and with low incompressibility.

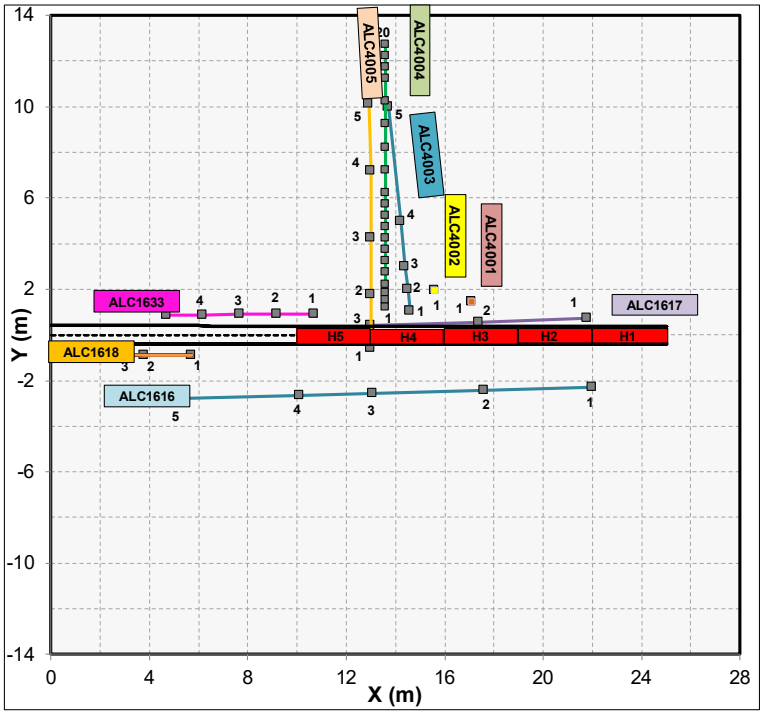

Figure 5-1 Horizontal cross-section indicating of instrumentation. ALC1633 and ALC1618 boreholes are located on the non-heated zone of the ALC1604 experiment and contain various piezometer chambers.

5.1.1 Pore pressure response to a thermal load

The pore pressure response to a thermal load has been described in Section 3.1. As expected, temperature increases triggered a significant increase in pore pressures. The increasing temperature affects rock mass behaviour with the generation of overpressures and associated mechanical effects.

Figure 5-3 shows the evolution of pore pressure in all sensors within the vertical cross-section located at 13 m from GAN gallery. The influence of the thermal load is evident in most of sensors, with the exception of sensor ALC4001 PRE 05, positioned 10 m away from the

alveolus. For the nearest sensors, combined effect of distance and orientation can be appreciated: Sensor ALC4005_PRE_01 and ALC1607_PRE_03, oriented in the direction orthogonal to the bedding present the higher increase in pore pressure and the slowest dissipation, while ALC1616_PRE_03 experiences a lower increase in pore pressure (although closer to the heater) and a quickest dissipation. Other ALC4005 sensors exhibit a response intermediate between the two previous one. This is a clear indication of a higher permeability along the bedding plane. Farthest sensor ALC4001 PRE 05 show a response similar to the sensors located in the non-heated zone in front of the alveolus head (ALC1633 and ALC1618) It is interesting to note that the temperature variations imposed by the presence of GAN gallery induce as well small variations of pore pressure.

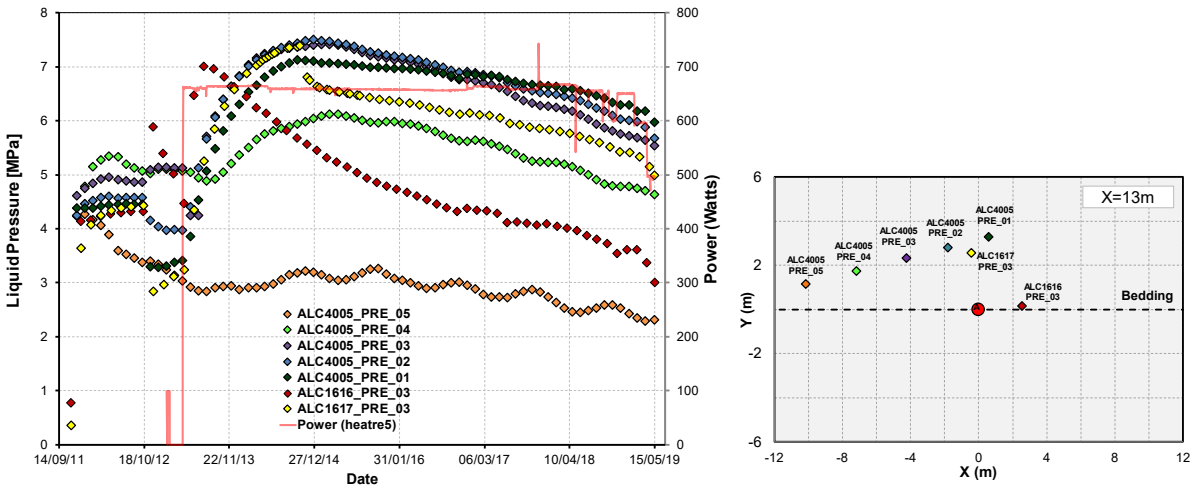

Figure 5-2 Pore pressure measured on sensors ALC4005_PRE_01 to PRE_05, ALC1616_PRE_03 and ALC1617_PRE_03 during all the experiment. The red line indicates changes of power injected in the heaters.

Of more interest, and more challenging, are the observations and predictions of the pore pressures evolution inside the host rock (COx) during excavation. A good understanding of the pore pressure response due to excavation operations is also a major concern in the experiment. As shown below, hydro-mechanical coupling, and particularly the configuration and extent of the EDZ, play a major role in the pore pressure response. Figure 5-3 shows the variation with time of pore pressures, measured with capacitive sensors in section 17.5m deep. The same graph is shown in Figure 5-4, but with an emphasis on the first days. Water pressure raises at those locations as the excavation front approaches the measurement points up to a value of about 8 MPa, i.e. 3.3 MPa above the initial value. After that, pressure drops rapidly to 2MPa as soon as the excavation front passes the corresponding measuring points. In the zone above the tunnel crown, pressures decrease. However, the EDZ barely grows in this direction. Also, permeability remains almost constant. Figure 5-3 shows the evolution of pore pressures at the borehole ALC1617 that is located in the vertical plane of the tunnel, 3.2 m away from the wall outside the EDZ. There is a slight increase of pore pressures as the excavation front approaches the measurement points, which was captured by the analysis. Also, the pressure drop is underestimated by the simulation. A possible explanation for this difference is that, under plane strain conditions, the out-of-plane deformation component can be neglected.

As expected, temperature increases during the thermal load trigger a significant upsurge of pore pressures. It is noticeable that the pore pressure responds to the temperature rise immediately and the higher the temperature change, the stronger the response. The maximum pore pressure increase, in this case, is 7.5 MPa, a significant magnitude. It can also be observed that the pore pressure evolution does not precisely match that of temperature; at some time the pore pressure stops rising, even though temperatures increase further. Dissipation by liquid flow overcomes the thermal effect. This phenomenon is especially noticeable at two points located in the bedding plane (ALC1616 and ALC4001). Although the overpressure peak was observed in the tunnel´s horizontal plane in the 140 days after heating began, this peak had not yet been reached in the vertical plane above the tunnel crown after more than 800 days. The difference between the times taken to reach the overpressure peak in the vertical and horizontal planes can again be explained by the anisotropic thermal and hydraulic properties of the rock.

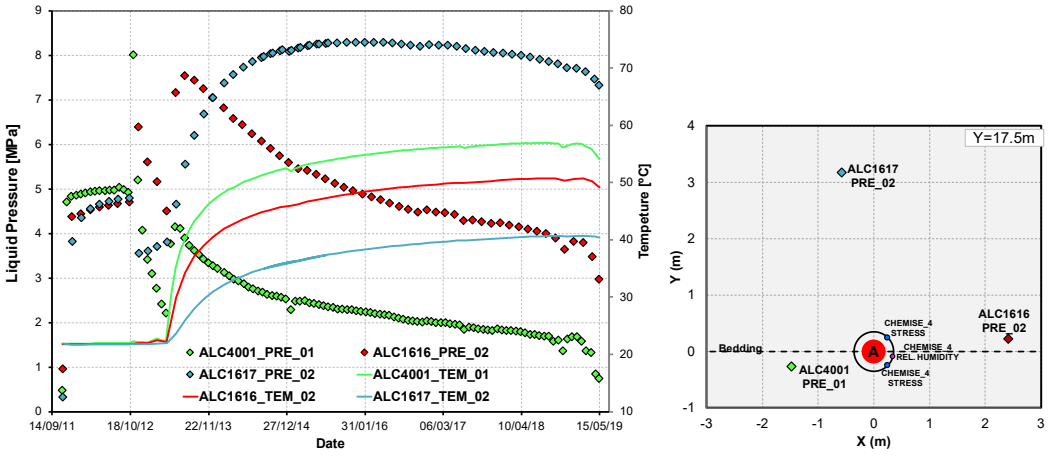

Figure 5-3 Pore pressure and temperature evolution measured in sensors ALC1616_PRE_02, ALC1617_PRE_02 and ALC4001_PRE_01 located on the same section as the heaters (17.5 m deep from the gallery).

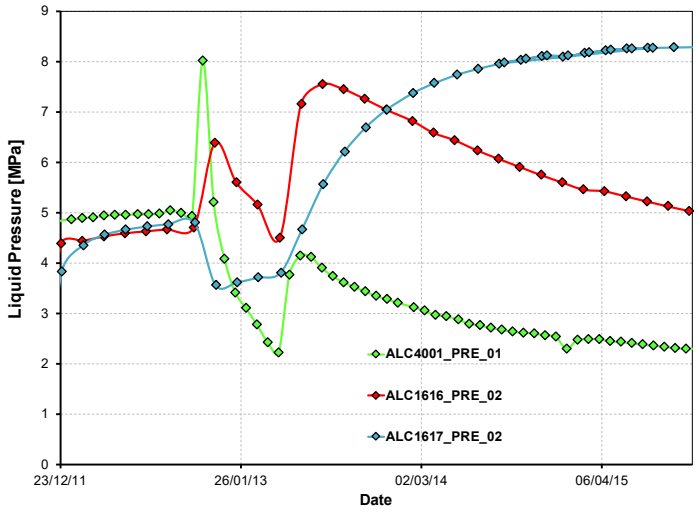

Figure 5-4 Pore pressure and temperature evolution measured in sensors ALC1616_PRE_02, ALC1617_PRE_02 and ALC4001_PRE_01 located on the same section as the heaters (17.5 m deep from the gallery).

5. 2 Thermo-hydro-mechanical numerical modelling

The numerical analysis has been carried out using the same mesh used for the 3D thermal analysis. More detail about the model are given hereinafter.

5.2.1 Material parameters

5.2.1.1 Parameters of the Callovo-Oxfordian claystone (COx)

Table 5-1 presents the values of all the THM parameters used for the Callovo-Oxfordian in the model, and the sources cited. The mechanical model is described in section 3.3 and Appendix I. It consists of an anisotropic visco-elasto-plastic model with creep. The transverse elasticity has been used in previous experiment, either in Callovo-Oxfordian (TER and TED experiments) or in the Opalinus clay (HE-D).

Rock strength anisotropy was defined by adopting scaling factors c_N = 1.33 and c_S = 1.0, selected to obtain a reasonable configuration of the damaged zone. The stratification planes in the COx formation are nearly horizontal; therefore the angles α and β (Figure I. 5) were set equal to zero.

According to measurements of wave velocities in cubic samples (Armand *et al.*, 2013), the ratio between horizontal and vertical Young's modulus has been set to 1.3. Young's modulus and permeability results from a back-calculation of the evolution of pore pressures measured in the HA-ALC1604 experiment. Values obtained were $E_{//}$ = 5200 MPa, $E_{\perp}$ = 4000 MPa for the Young modulus and $k_{//}=2\times10^{-20}$ m^2, $k_{\perp}=1\times10^{-20}$ m^2 for the permeability. Stiffness values differ slightly from the ones used in the simulation of TED experiment ($E_{//}$ = 6000 MPa, $E_{\perp}$ = 3000 MPa). Discrepancy is higher for the permeability, since it is 3 times lower than the one used in TED experiment.

Parameters used for the viscoplastic and creep part of the model come from the modelling of CGS excavation performed by (Mánica *et al.*, 2016). The change in permeability in the Excavation Damage Zone, given by parameter η has been back-analysed in the present modelling to match pore pressure during the excavation phase.

Thermal parameters are the ones back-analysed during the three-dimensional thermal modelling. Solid thermal expansion comes from (Auvray, 2004) and the previous modelling of TER and TED experiments.

Table 5-1 Callovo-Oxfordian claystone parameters used in the simulations.

properties	Parameter	Orientation*	Value	
Mechanical	Young's Modulus, E: MPa	Parallel	5200	Back-analysis of ALC1604 test.
		Perpendicular	4000	
	Poisson's ratio, ν	Parallel	0.25	Reference value
		Perpendicular	0.35	
	Peak friction angles, φ_{peak}	-	22.0	Calibration of the constitutive model (Miguel Mánica; *et al.*, 2016)
	Initial friction angles, φ_{ini}	-	9.35	
	Mobilised friction angles, φ_{res}	-	14.74	
	peak cohesion, c_{peak} : MPa	-	3.55	
	Constant that controls the curvature of the function in the hardening branch, a_{hard}	-	0.0035	
	Constant that controls the curvature of the function in the softening branch, a_{soft}	-	0.07	
	Coefficient of non-associativity, ω	-	0.6	
	Equivalent plastic strain at which the maximum strength is reached, ξ_1 : MPa	-	0.005	
	Equivalent plastic strain at which softening begins, ξ_2 : MPa	-	0.006	
	Equivalent plastic strain at which the residual strength is reached, ξ_3 : MPa	-	0.06	
Mechanical (Time-dependent mechanism)	The threshold from which viscoplastic strains are activated, σ_s : MPa	-	4.0	
	Viscosity parameter, γ : day^{-1}	-	1x10^{-7}	
	Material constants, n	-	3.37	
	Material constants, m	-	530	
Hydraulic	Intrinsic Permeability, k	Parallel	2·10^{-20}	Back-analysis of ALC1604 test
		Perpendicular	1·10^{-20}	
	Material parameters, A		1.0	
	Material parameters, Λ		3.0	
	Model parameter, P : MPa		14.3	
	Material parameters, λ		0.33	
TM	Linear Thermal expansion coefficient of the rock, α_T: K^{-1}	-	1.4·10^{-5}	Auvray (2004)
HM	Biot Coefficient, b	-	0.6	Reference value
	Constant controls the rate of change of intrinsic permeability, η	-	300	Back-analysis of ALC1604 test
	Threshold in the plastic multiplier for the change in permeability	-	1.2e-4	
Thermal	Linear Thermal expansion coefficient of the solid grain, α_T: K^{-1}	-	1.4·10^{-5}	Value and anisotropic ratio from Auvray (2004)
	Thermal Conductivity, λ: W/m/K	Parallel	2.05	Anisotropic back-analysis of thermal field
		Perpendicular	1.33	
	Specific heat capacity of the solid, c_s: J/kg/K	-	800	Auvray (2004)
Petrophysical	Solid compressibility, β_s	-	2.5·10^{-5}	From mineral composition
	Specific weight, ρ_s: kg/m3	-	2.7	Reference value
	Porosity, ϕ	-	0.173	Martin & Lanyon (2003)

5.2.1.2 Parameters for the sleeve and the air gap

The selected steel lining has a sufficiently high yield strength (above 400 MPa) to reduce the risk of early-stage plasticity due to host rock anisotropic convergence and to overcome Stress Corrosion Cracking (SCC) (Bumbieler *et al.*, 2015). The sleeve is considered to be linear elastic with parameters E, ν and α, respectively, for Young's (elastic) modulus, Poisson's ratio and the coefficient of thermal expansion. Mechanical and thermal properties of steel lining are listed in Table 5-2.

As stated above, the model contains a gap between the host rock and the sleeve. This gap is modelled as a material with very high porosity and permeability (several orders of magnitude larger than the other materials, see Table 5-3). The retention curve is also considered but with a very low value of the reference air entry capillary pressure P_o (P_o = 0.001 MPa), as the gap corresponds is in essence a material with very large pores. This implies that saturation takes place sharply as capillary pressure vanishes. To avoid numerical convergence problems, the porosity has been set to a high value (0.8) but less than one. Dependency of both permeability and air entry pressure on porosity has been considered in order to model their evolution towards host rock values when the gap closes.

From the mechanical point of view, the gap was modelled using a bilinear elastic model that uses two values of Young's modulus, one for the opened gap and the other for the closed gap. A large value of Young's modulus (E_c) was used for the closed gap (representing the contact between gap surfaces), and a relatively low value (E_o) was used for the open gap (Figure 5-5). The volumetric strain was used to check whether the gap was open or closed. As, during the calculations, the gap undergoes a path from an initial open state towards a closed state as the casing expands, the approximation considered was deemed adequate.

Table 5-2 Steel lining properties adopted in the THM analysis.

properties	Parameter	Value
Thermal	Thermal Conductivity, λ : (W/m/K)	80
	Specific heat of solid (J/kg/K)	550
	Linear Thermal expansion coefficient, α_T: K^{-1}	$1.4 \cdot 10^{-5}$
Mechanical	Young's Modulus, E: MPa	0.005
	Poisson's ratio, ν (-)	0.3

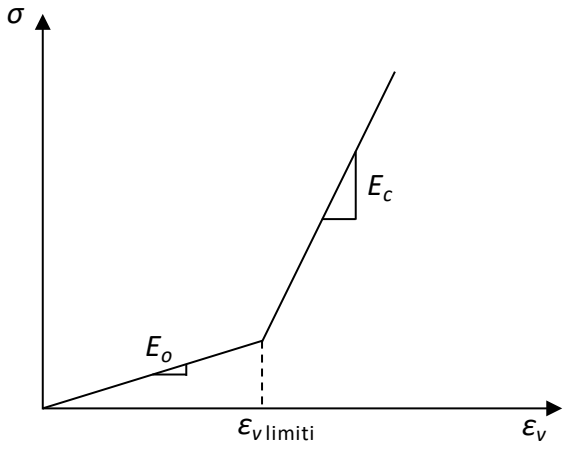

Figure 5-5 Bilinear elastic model.

Heat transfer across the gap will take place by conduction, radiation and convection. At the local scale, the state of the gap (i.e. open/closed gap and degree of saturation) is expected to be an important factor controlling the maximum temperature of the COx and sleeve. For the conductive flux, the Fourier law is used. In this study, the combined effects of conduction and radiation are included in the conductive flux using an equivalent conductivity. Moreover, thermal conductivity varies with saturation. When the gap is dry, the thermal conductivity is set to 0.035 W/mK (mixture of air and water vapour) and to 0.6 W/mK (liquid water) when saturated. Table 5-3 summarises air gap parameters used in the analysis.

Table 5-3 Air-gap element properties adopted in the 2D THM analysis.

properties	Parameter	Value
Thermal	Thermal Conductivity λ_{dry} : (W/m/K)	0.035
	Thermal Conductivity, λ_{sat} : (W/m/K)	0.6
Hydraulic	Intrinsic permeability, k_0 : (m2)	10^{-16}
	Porosity, ϕ_0 (-)	0.8
	Parameter for van Genuchten model, λ (-)	0.5
	Measured P at certain temperature, $P_0(MPa)$ $P_0(\phi) = P_0 \exp[\alpha(\phi_0 - \phi)]$	0.001
	Parameter for van Genuchten model, α (-)	10
Mechanical	Young's Modulus, E_c: MPa	200
	Young's Modulus, E_o: MPa	1.0
	Strain limit, $\varepsilon_{v\,limit}$ (-)	0.005
	Poisson's ratio, ν (-)	0.3

5.2.1 Domain discretisation

A three-dimensional coupled THM analysis has been performed in order to incorporate the anisotropic properties of the COx and the anisotropy of the in-situ stress state.

The model domain and the finite element mesh used is depicted in Figure 5-6. Dimensions are 50 m × 50m ×50 m, and the reference axis system has been taken equal to the local system defined for the HA-ALC1604 test (see section 4.4.1 of thermal modelling). The mesh has been

refined near the gallery and near the micro-tunnel, in order to be able to cope with the high temperature (and subsequently pore pressure) gradients in this zone. The distance to the boundary is 25 m, which corresponds to the distance from the micro-tunnel axis to the gallery GRD. Besides the host rock domain, the model includes the geometry of the sleeve and the air gaps formed by the sleeve and the Cox, the sleeve and the insert and the insert and the COx. According to the experimental layout, the sleeve is supported on the bottom of the excavation, and then the sleeve, insert and gaps are eccentric with respect to alveolus centreline. This aspect is represented in the geometry.

The mesh used in this computation contains about 3312 tetrahedral elements and 6720 nodes. The domain and the finite element mesh used are depicted in Figure 58. The initial and boundary conditions are depicted in Fig 59 and summarized in table 4.1.

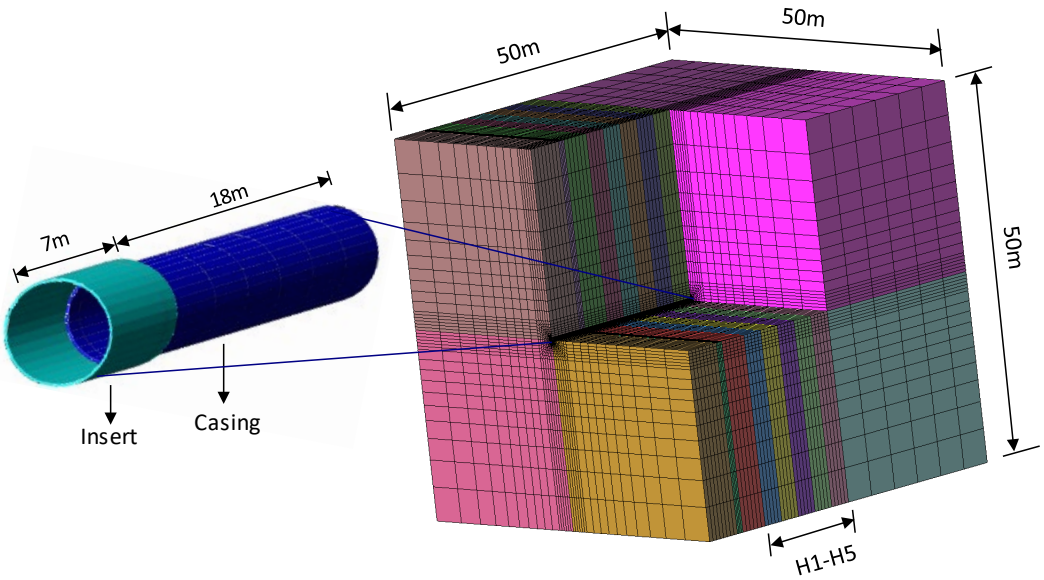

Figure 5-6 Geometry and mesh used for 3D THM simulation. The alveolus ALC1604 is oriented parallel to the major horizontal stress direction.

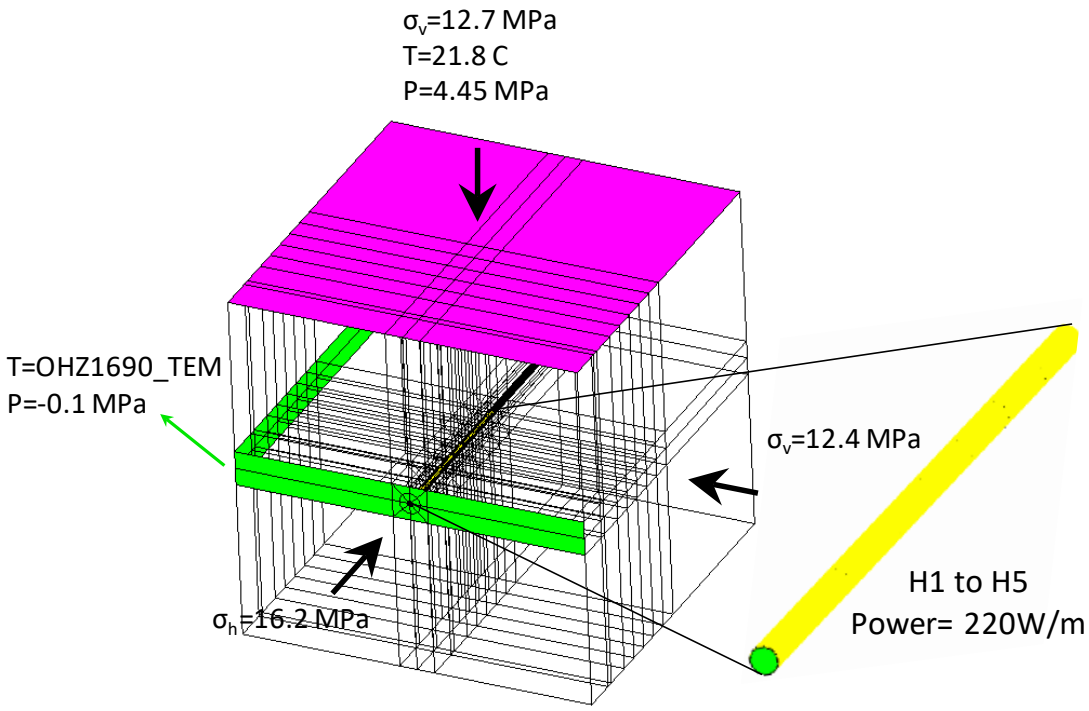

Figure 5-7 Initial and boundary conditions applied for 3D THM simulation.

An initial constant temperature of 21.8°C has been assumed throughout the geometry. A hydrostatic distribution of water pressure was initially defined, with a value equal to the field value (4.7 MPa) at HA-ALC1604 experiment level. Fully anisotropic lithostatic stress distribution has been initially prescribed. Values at experiment level are 16.2 MPa, 12.4 MPa and 12.7 MPa for the vertical, the major and minor horizontal components, respectively. Porosity was set to 17.3% in the COx.

Table 5-4 Initial and boundary conditions applied

	Condition	Parameters	First point	Final point	Distribution
COx	Initial Liquid pressure	Pl [MPa]	4.45	4.95	Linear
	Initial Temperature	T [^{0}C]	21.82		Constant
	Initial Porosity	ϕ	0.15		Constant
	Initial Stress	X Stress	-9.937	-14.0625	Linear
		Y Stress	-9.937	-14.0625	Linear
		Z Stress	-13.216	-18.703	Linear

The different phases of numerical analyses have mimicked the different stages of the experiment listed in Table 2-1. The analysis started simulating the tunnel excavation followed by the construction of the sleeve and the insertion of the heater. After the installation of heaters, an isothermal period of three months was simulated.

Afterwards, the main power was applied to the heaters. During the heating stage of the experiment, the input power will be maintained long enough to achieve a quasi-permanent state, in order to separate the transitory and the steady-state. As for the thermal analysis, a small part of the heat input has been prescribed in the non-heated zone to simulate the heating of this zone by conduction/radiation and air convection.

For reference, two 2D plane strain analyses have been performed and the results compared with those of the 3D simulation. The model domain, finite element meshes and main boundary conditions (B.C.) adopted are depicted in Figure 5-8. The analysis "A1" has been run for the section located at a depth of 17.5 m (Cross-section across Heater 3) which is the location of the three boreholes that contain temperature sensors and piezometers. A second analysis "A2" has been run with a different value of heat flux for the section located at a depth of 13 m, which is the location of the three boreholes that contain temperature sensors and piezometers.

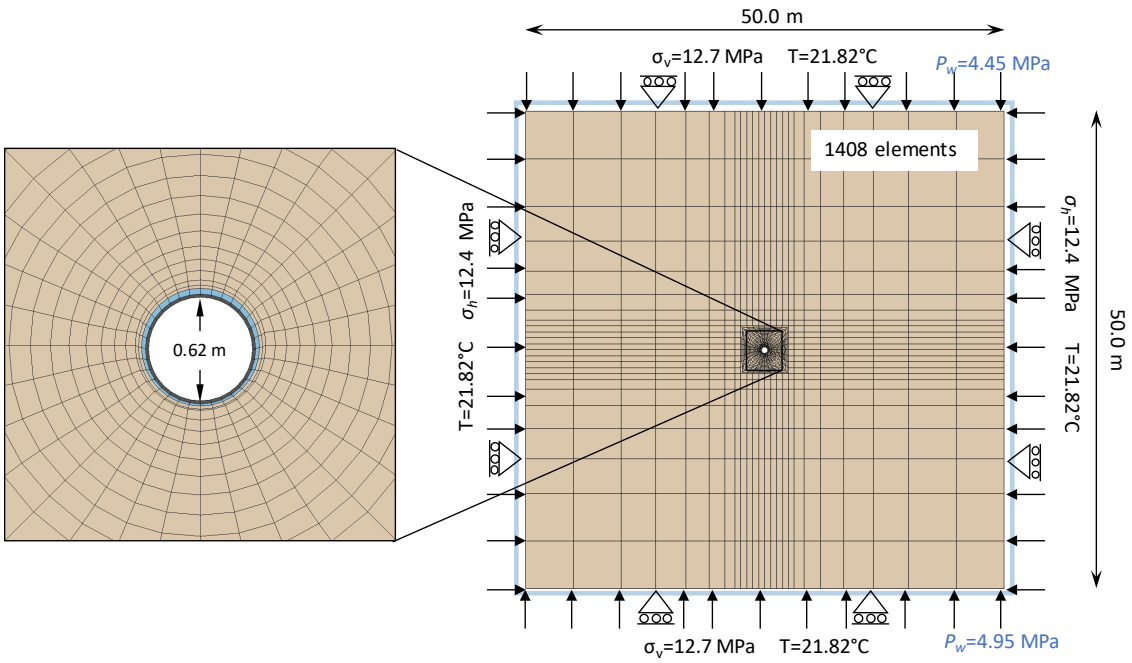

Figure 5-8 Geometry, mesh and boundary conditions from the 2D THM analysis of HA-ALC1604 in situ heating test.

5.3 Comparison of measurements and simulations

5.3.1 Thermal results

There were three sensors in section A1 and seven sensors in Section A2, located at different orientations with respect to the bedding plane (Figure 5-9**)**. The evolution of temperatures at Section A and Section B are shown in Figure 5-9**,** and compared with the results of the 2D and 3D analyses. It can be noted that, after about one year of heating, temperatures generally rise very slowly throughout the COx claystone. Moreover, anisotropic effects are noticeable: temperature along the bedding increases more rapidly than in the orthogonal direction. As expected the 3D THM output the same temperature field and the T-analysis and captures consequently well temperatures variations at all sensors. It is worth noting that the observed

stabilization of temperatures at the end of the heating phase (1st semester 2019) and well-captured by the 3D model cannot be reproduced by the 2D models. This indicates that heat dissipation along the Y-direction (direction of alveolus) has a major effect on the temperature field in the rock.

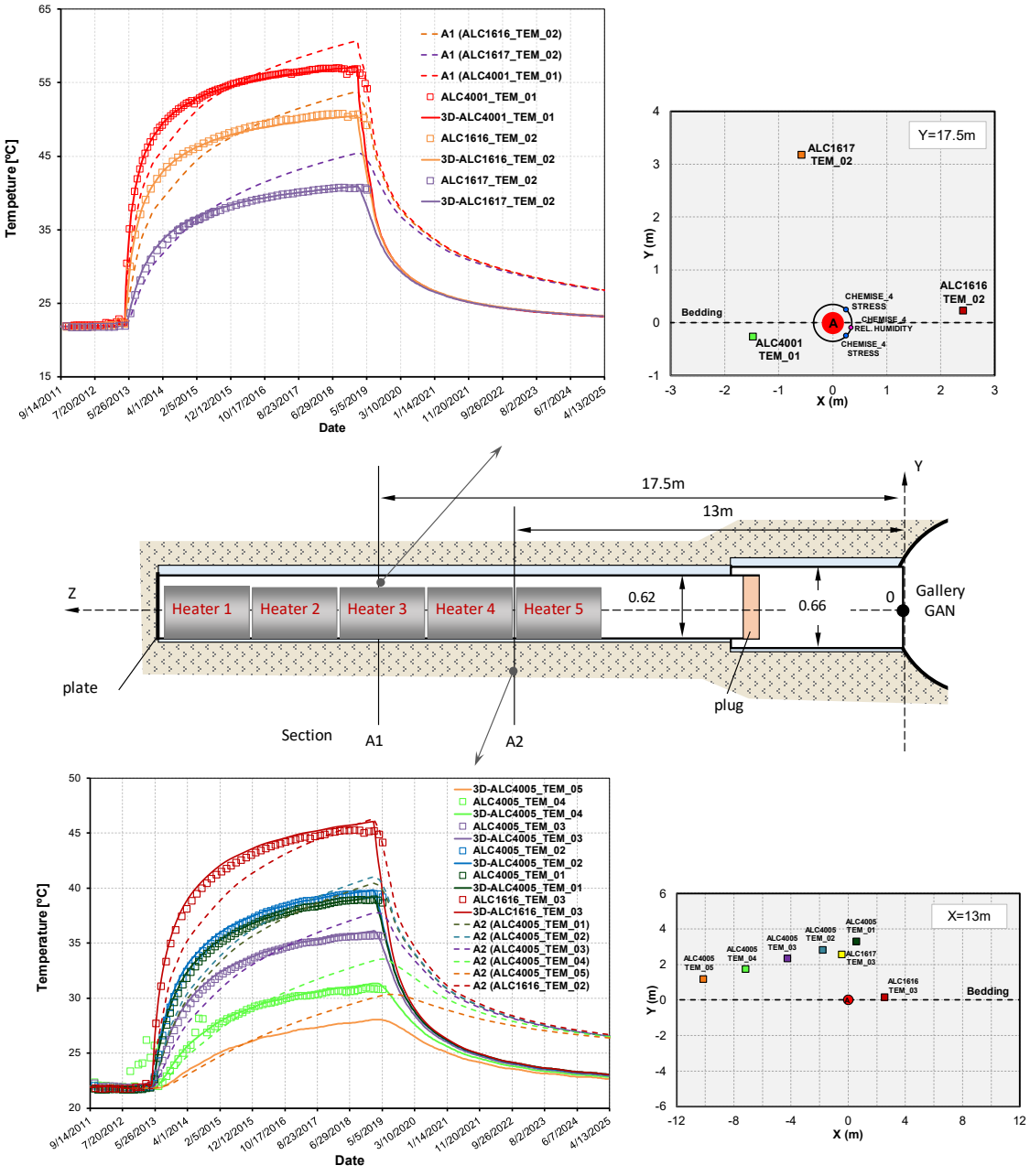

Figure 5-9 Evolution of temperatures in COx, observations and computed results: (a) Section "A1", z 17.5 m; (b) section A2, z 13 m.

More information about the 3D shape of temperature bulb is given in Figure 5-10 and Figure 5-11 by plotting contours of temperature isovalues at different in a vertical cross-section orthogonal to heater 3 (labelled section "A"). The following times have been selected: 114 days

(end of the first heating stage); 260 days (time at which maximum pore pressures are achieved); 960 days (two years heating); and 2000 days (five years heating, at the end of the simulation). The anisotropic temperature distribution is apparent, with higher temperatures being reached in the direction of the bedding planes. Similar information is presented in Figure 5-11 in a three-dimensional view. Profiles of temperatures within section "A" are plotted in Figure 5-12 for the same times. The progressive rise of temperature can be readily observed. It is interesting to note that the region with a significant temperature increase appears to be limited to a radius of about 5 m around the main borehole.

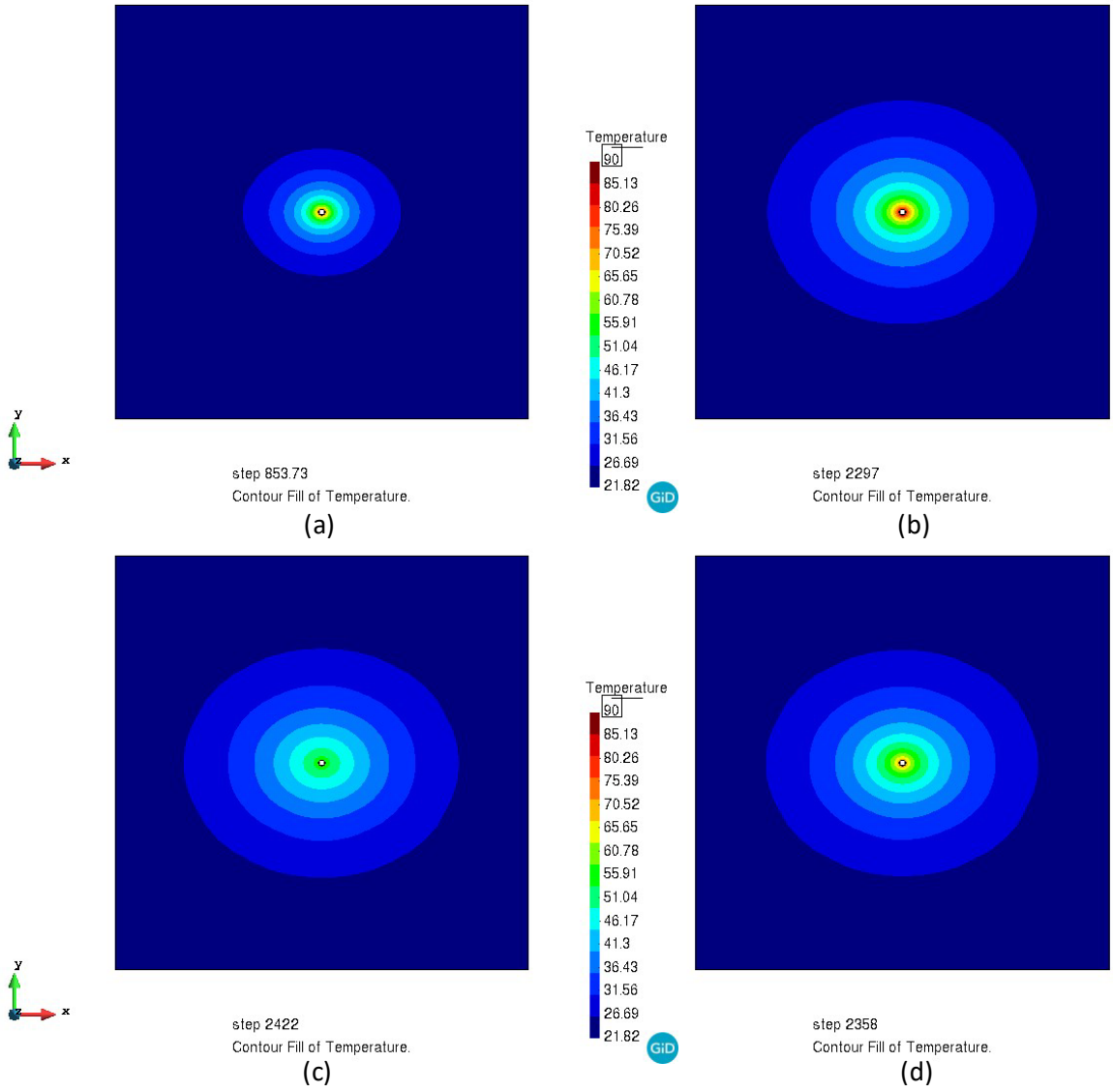

Figure 5-10 Computed contours of equal temperature (^{0}C) in a cross-section across Heater 3 for (a) 985 days (two years heating); (b) 2297 days (end of heating); (c) 2358 days (end of first cooling phase); (d) 2422 days (end of second cooling phase).

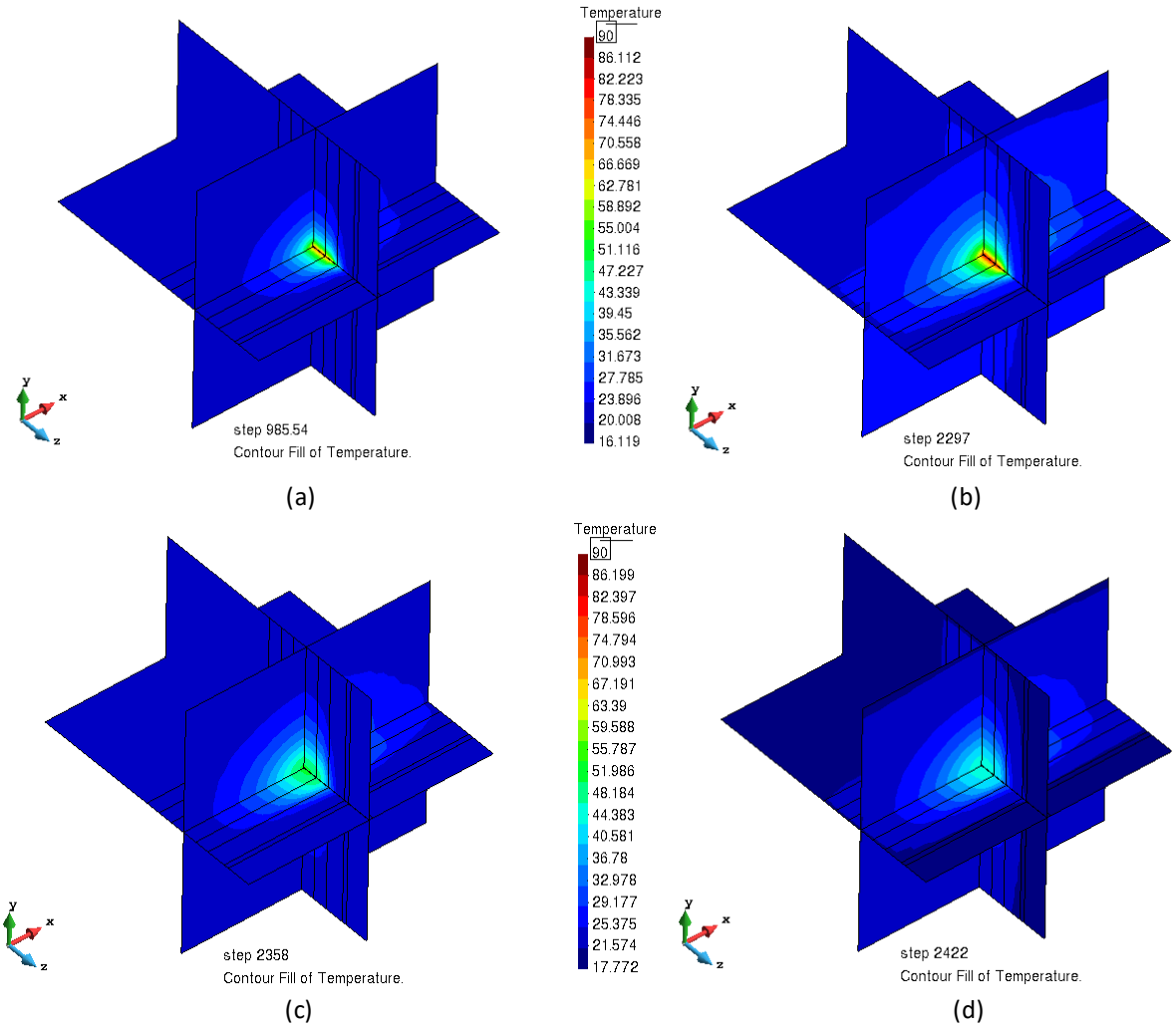

Figure 5-11 Three-dimensional views of computed contours of equal temperature (°C) on section A for (a) 985 days (two years heating); (b) 2297 days (end of heating); (c) 2358 days (end of first cooling phase); (d) 2422 days (end of second cooling phase).

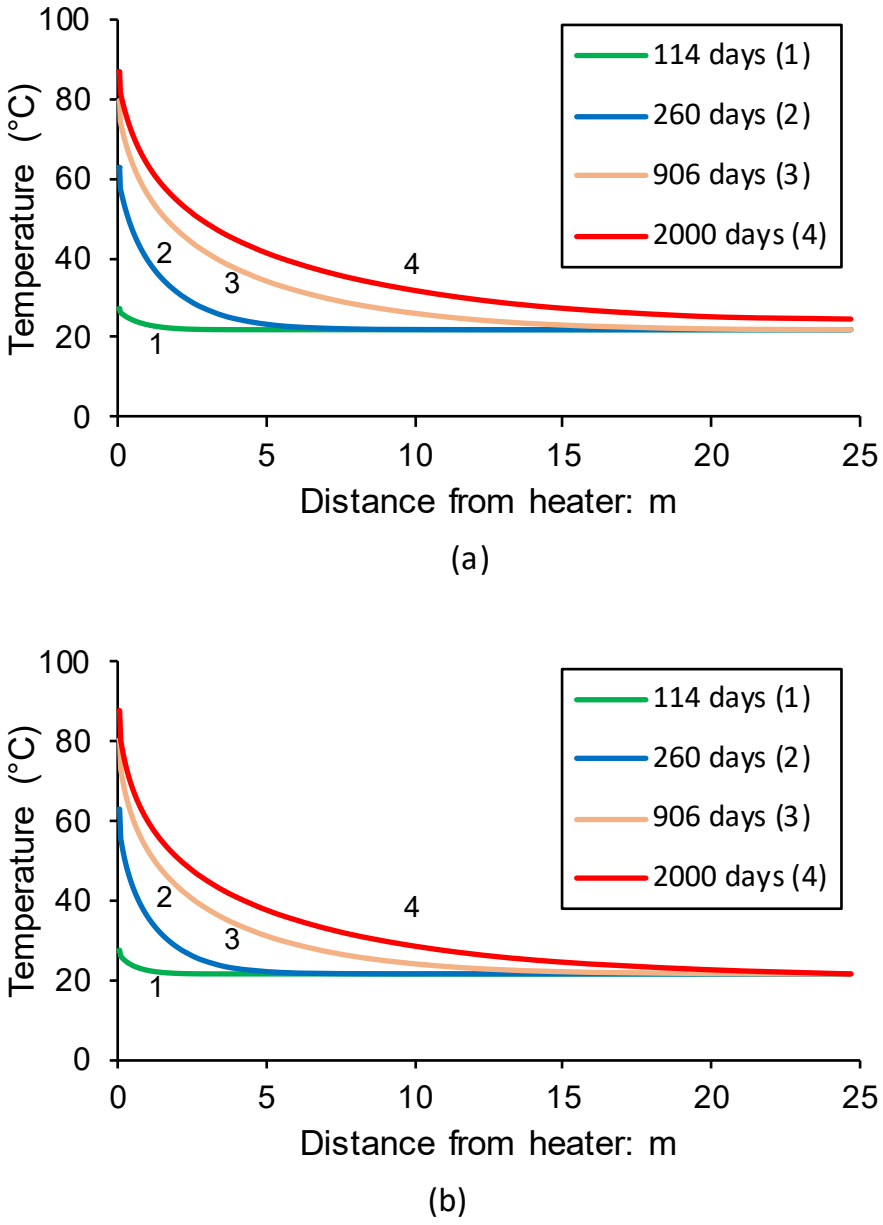

Figure 5-12 Computed temperature distributions at various times on section A: (a) bedding plane direction; (b) perpendicular to bedding plane direction.

5.3.2 Excavation damaged zone

The experiments have revealed that excavation operations induce damage and fracturing around the galleries (Armand *et al.*, 2014), creating a zone known as the excavation damaged zone (EDZ), where significant changes in flow and transport properties take place (Tsang, Bernier and Davies, 2005). The observed configuration of the EDZ depends on the orientation of the excavation concerning the anisotropic in-situ stress state. The EDZ is identified as one of the critical issues affecting the long-term behaviour of the tunnel near-field (Blümling *et al.*, 2007). Significant efforts have been made to simulate these experimental excavations (Seyedi and Gens, 2017) and to gain insights into the design of the actual repository.

As stated above, the ALC1604 cell is parallel to the major horizontal stress σ_H and has a nearly isotropic stress state in the plane normal to the tunnel axis. Despite of that, the EDZ extends further in the horizontal direction (Figure 5-13a), suggesting strong anisotropic characteristics of the rock mass. An estimate of the configuration of the excavation-damaged zone can be obtained by plotting contours of the cumulative plastic multiplier as it is directly related to the magnitude of irreversible strains (Figure 5-13b). The lateral extent of the shear fractures zone for smaller opening is almost equal to one diameter of the opening (Armand et al. 2014). Model results suggest that a plastic zone of up to 0.7 m away from the micro-tunnel wall is formed. At the point with the higher plastic multiplier, much more substantial mechanical effects on rock deformability and hydraulic diffusion will be identified. It can be seen that the configuration of the damaged zone is similar to that observed in the previous micro-tunnels with the same orientation, extending more in the horizontal direction (Armand et al. 2014, 2017).

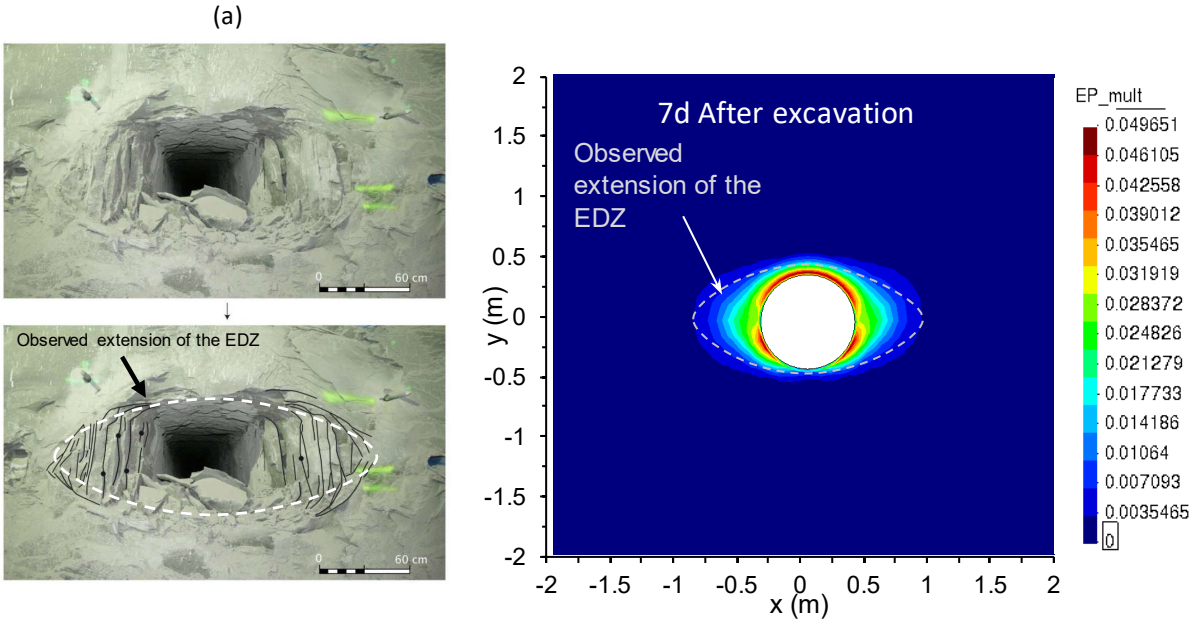

Figure 5-13 (a) Extension of the damaged zone around a full-scale HLW cell parallel to major horizontal stress (b) Obtained configuration of the EDZ in terms of the plastic multiplier in the section A1 at the end of the heating phase.

Figure 5-14 illustrates the evolution of damage around the tunnel at different times. After seven days from the excavation, almost all the damage has developed in the zone where stresses are higher than the available anisotropic strength. Afterwards, damage process slowly continues as the result of creep, consolidation and heating. At the end of the heating phase, after six years, the size of the damaged zone has only marginally increased. However, inside it, the intensity of damage was increased. After about 6 years cooling, the EDZ will either barely change or not alter at all.

Figure 5-15 shows horizontal profiles of accumulated plastic multiplier and intrinsic permeability on the right side of the alveolus. They evidenced the dependency of permeability on damage introduced in the model and whose coefficient has been back-analysed to reproduce correctly the pore pressure around the excavation. Permeability reaches a maximum value near the cell wall where it appears to increase of five orders of magnitude during excavation and one

additional order of magnitude during heating. These values should not be considered as quantitatively relevant but essentially indicate a high permeable zone because of fracturing close to the excavation wall. More important for an adequate capture of the pore pressures measured in the rock during the HA-ALC1604 experiment is the distance within the EDZ at which permeability experiences a change of at least one order of magnitude.

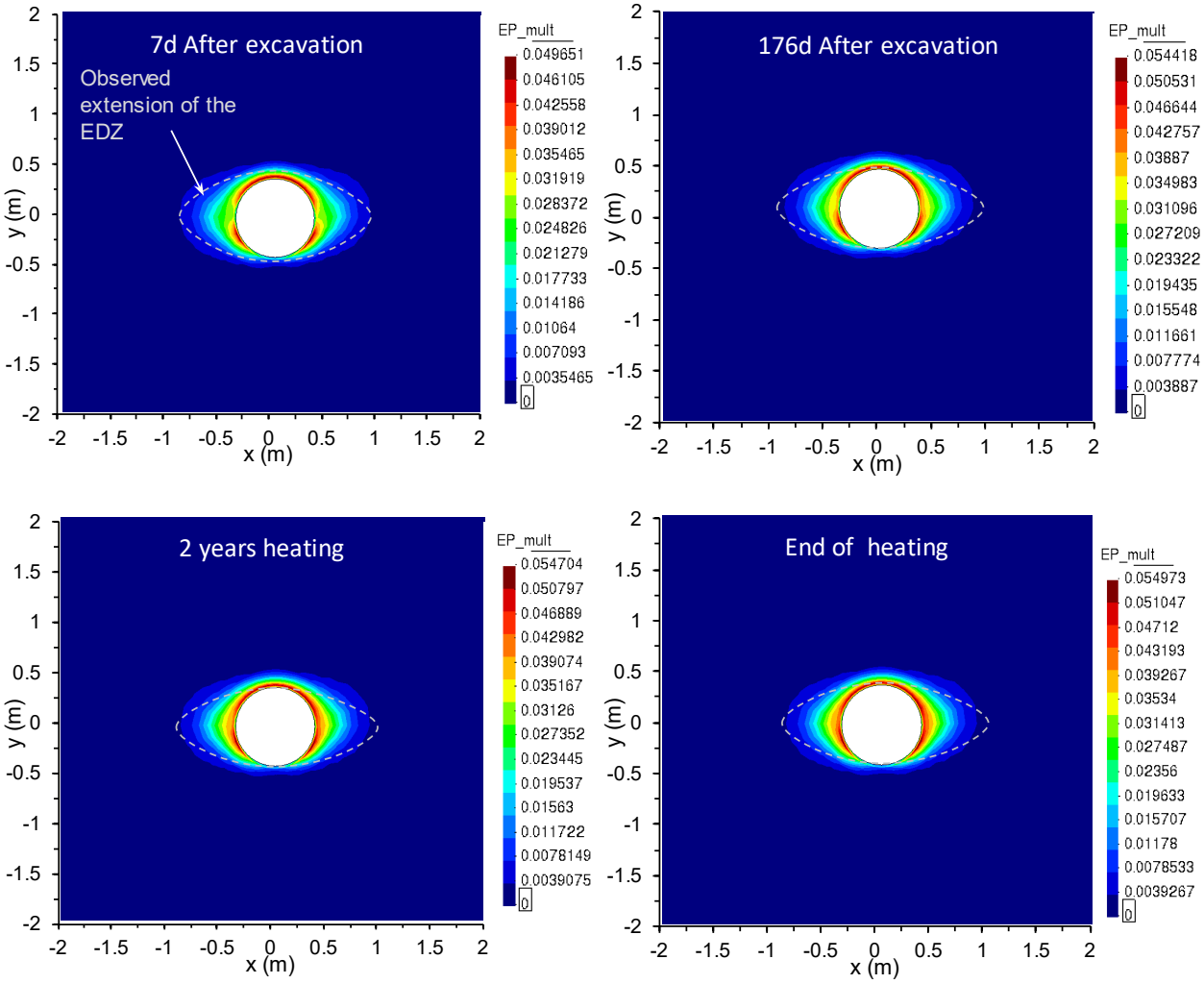

Figure 5-14 Damage distribution evolution in the model at different times.

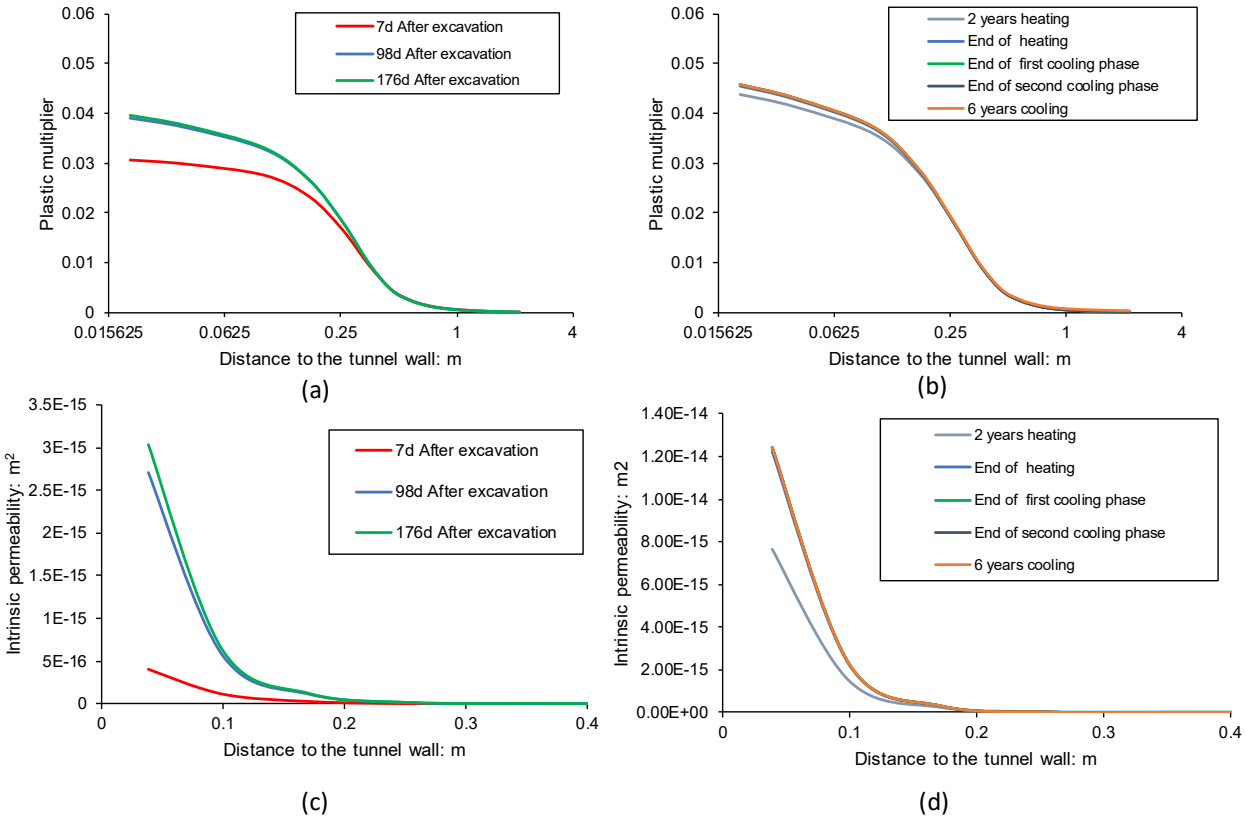

Figure 5-15 Computed Plastic multiplier and permeability increment distributions at various times (Horizontal distance to tunnel wall).

5.3.2 Pore pressures

Fig. 5-16 presents a comparison between the results of the 3D analysis and pore pressure measurements within vertical cross-section at 17.5 and 13 m. The results of the two 2D analyses have also been added for reference. It is apparent that pore pressure increase is reasonably well captured by the model for both the excavation and heating phases. The pore pressure rise registered during heating stage by sensor ALC1616_PRE_02 is however sharper than in the model. This could be due to the spatial discretization considered. Discrepancy is not observed for the two other sensors of the same sections.

In Figure 5-16 shows with grey lines the times of peak in pore pressure in the section at 17.5 m. Time becomes larger as the distance to the main borehole increases. These results from the combined effect of the movement of temperature rise outwards and pore pressure dissipation from the inner zones. This evolution can easily be observed in Figure 5-17, where profiles of pore pressure are plotted for various times. The two distributions plotted correspond to two orthogonal directions, one along the bedding plane and the other normal to the bedding. Differences can be observed between the two sets of distributions.

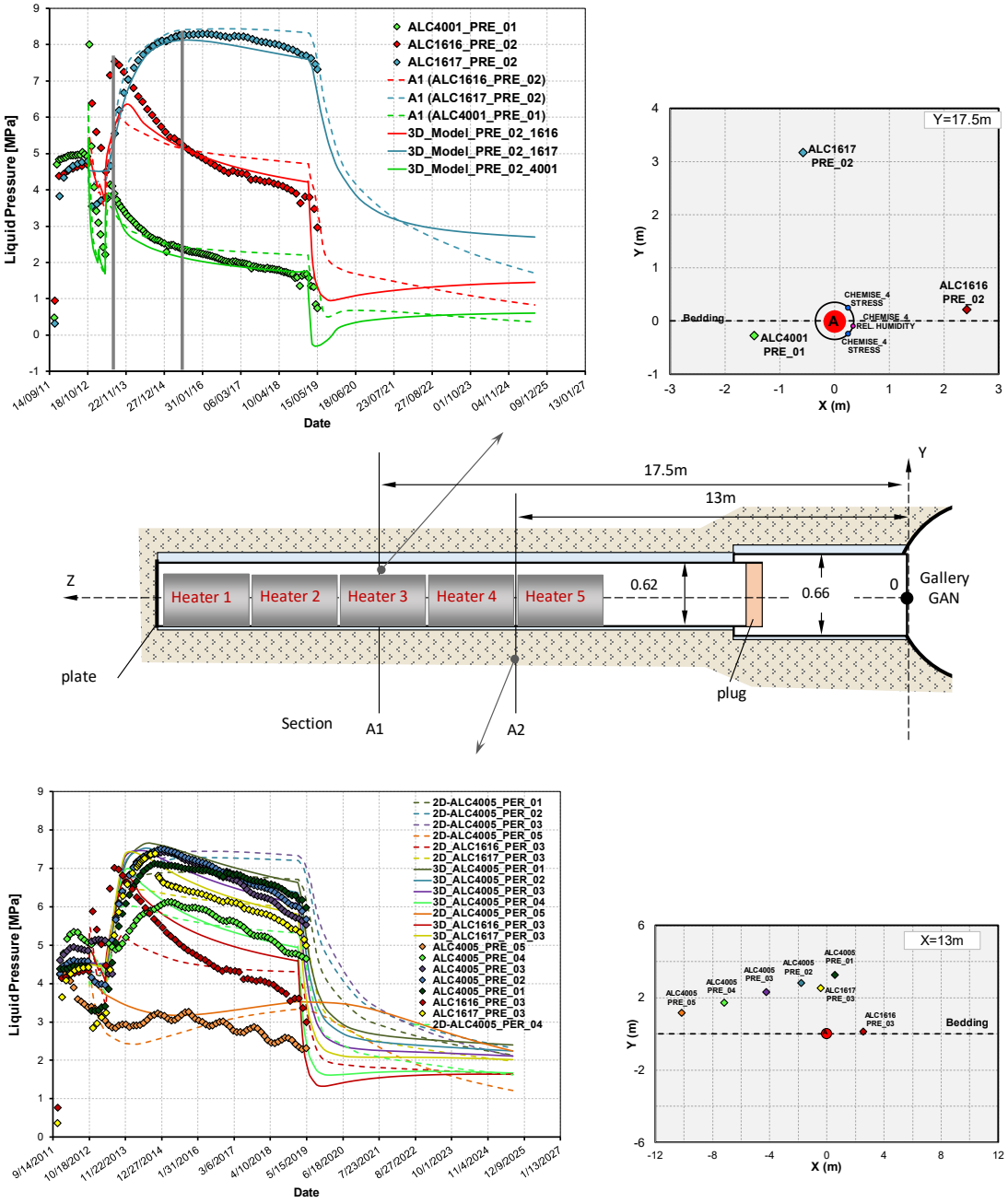

Figure 5-16 Evolution of pore pressure increments at various points in the clay: observed and computed results.

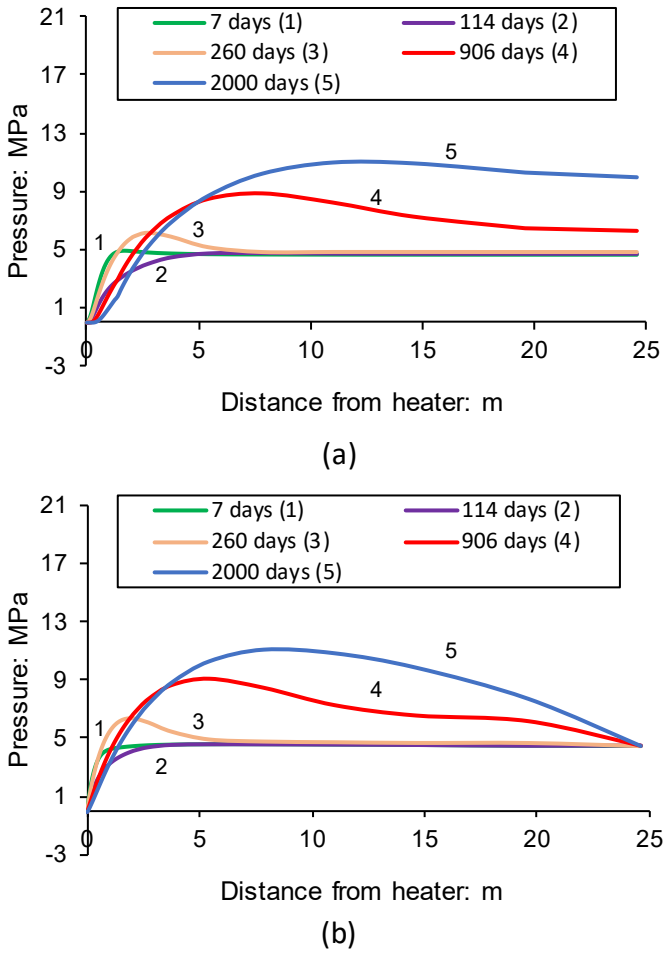

Figure 5-17 Computed pore pressure increment distributions at various times on section A1: (a) bedding plane direction; (b) perpendicular to bedding plane direction.

Finally, a general overview of pore pressure field around the experiment is shown in Figure 5-18, 5-19 and 5-20. Movement of the locus of maximum pore pressure away from the micro-tunnel as time goes on is readily apparent. Figure 5-18 also evidences the draining effect of GRD gallery at 2297 d.

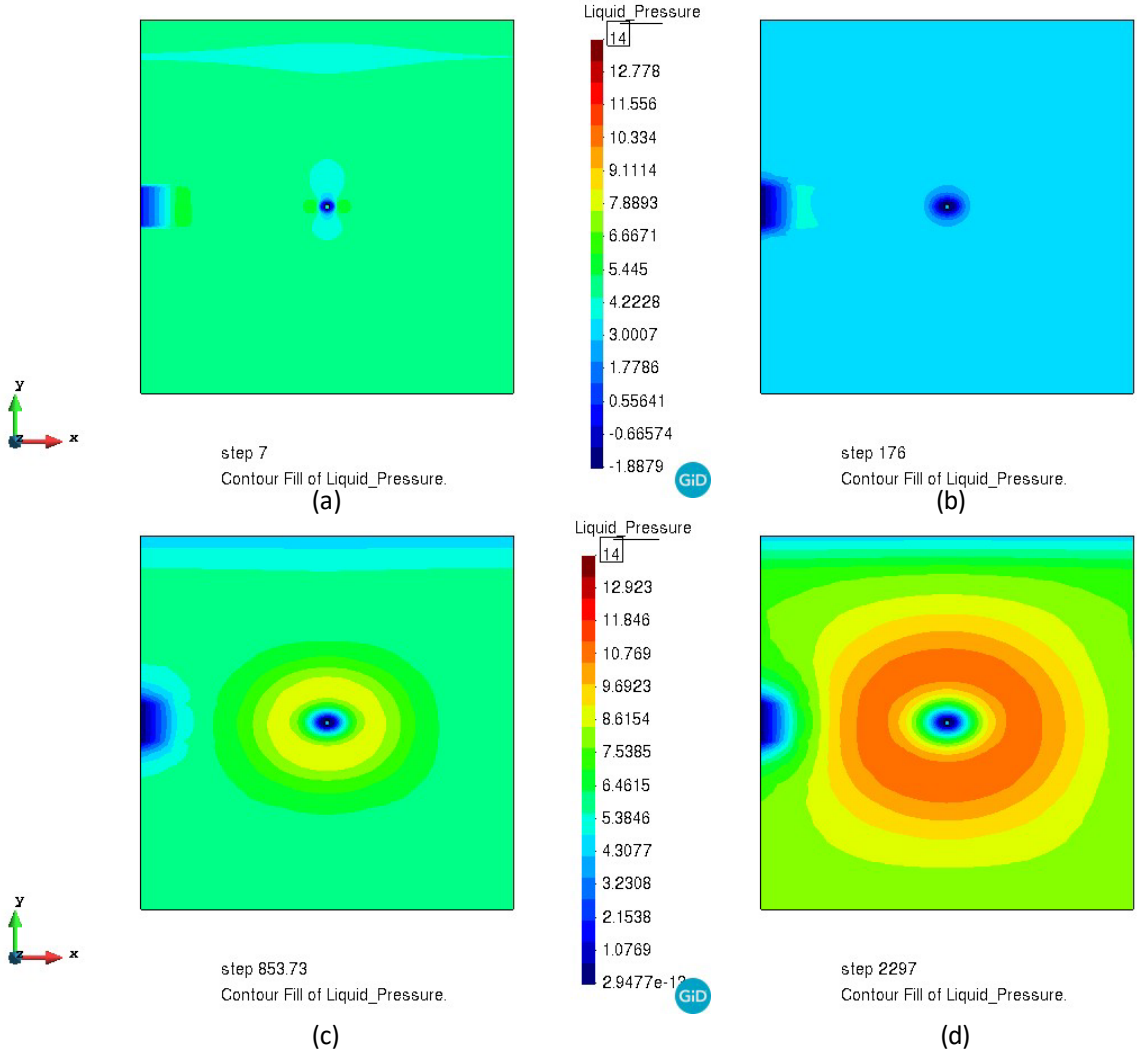

Figure 5-18 Two-dimensional view of computed contours of equal liquid pressure (MPa) in a cross-section across Heater 3 for: (a) 7 days (After excavation); (b) 176 days (end of heating test); (c) 853 days two years heating); (d) 2297 days (end of heating).

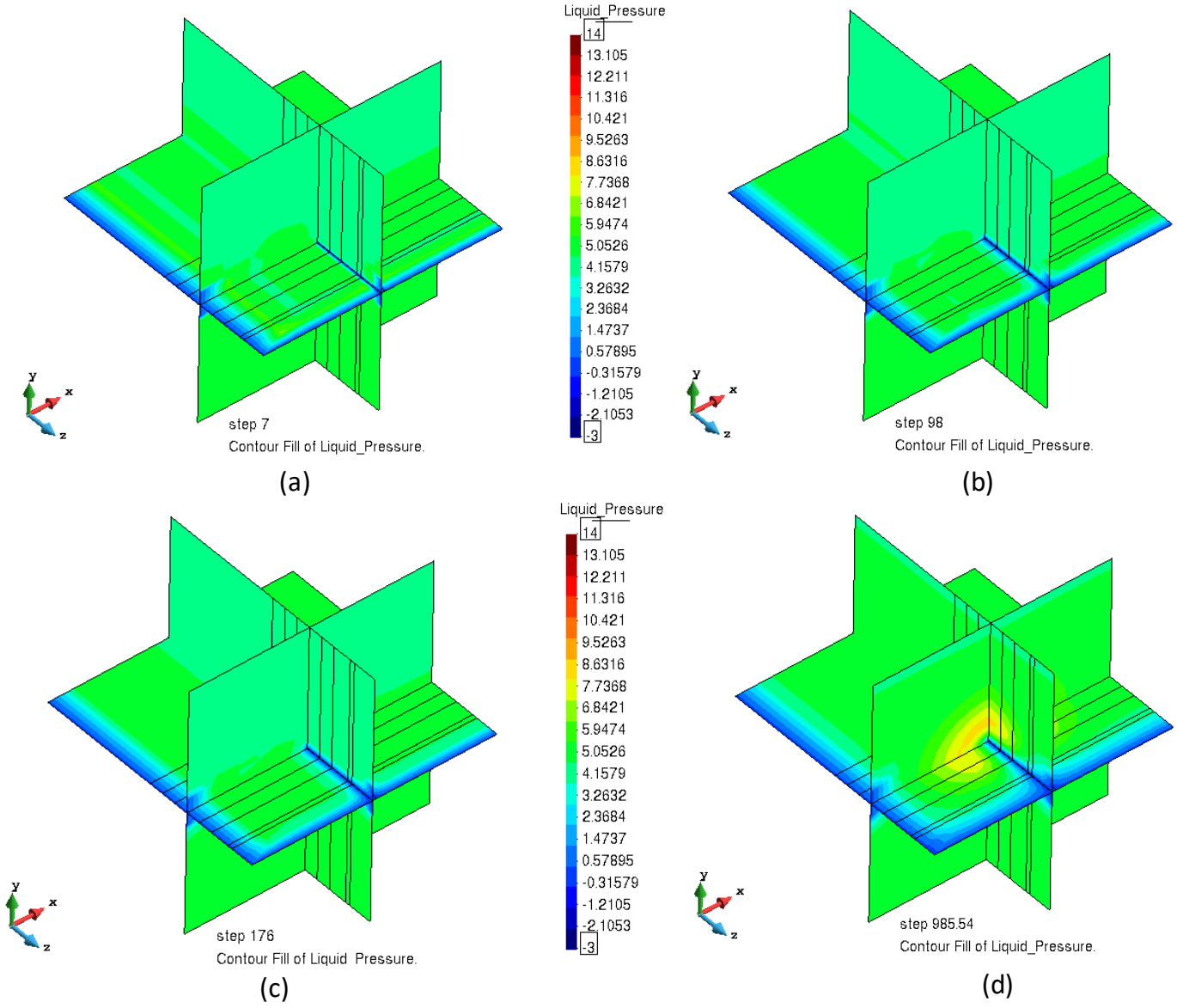

Figure 5-19 Computed contours of equal pore pressure increase (MPa) for: (a) 7 days (After excavation); (b) 98 days; (c) 176 days (end of heating test); (d) 985 days (2 years heating).

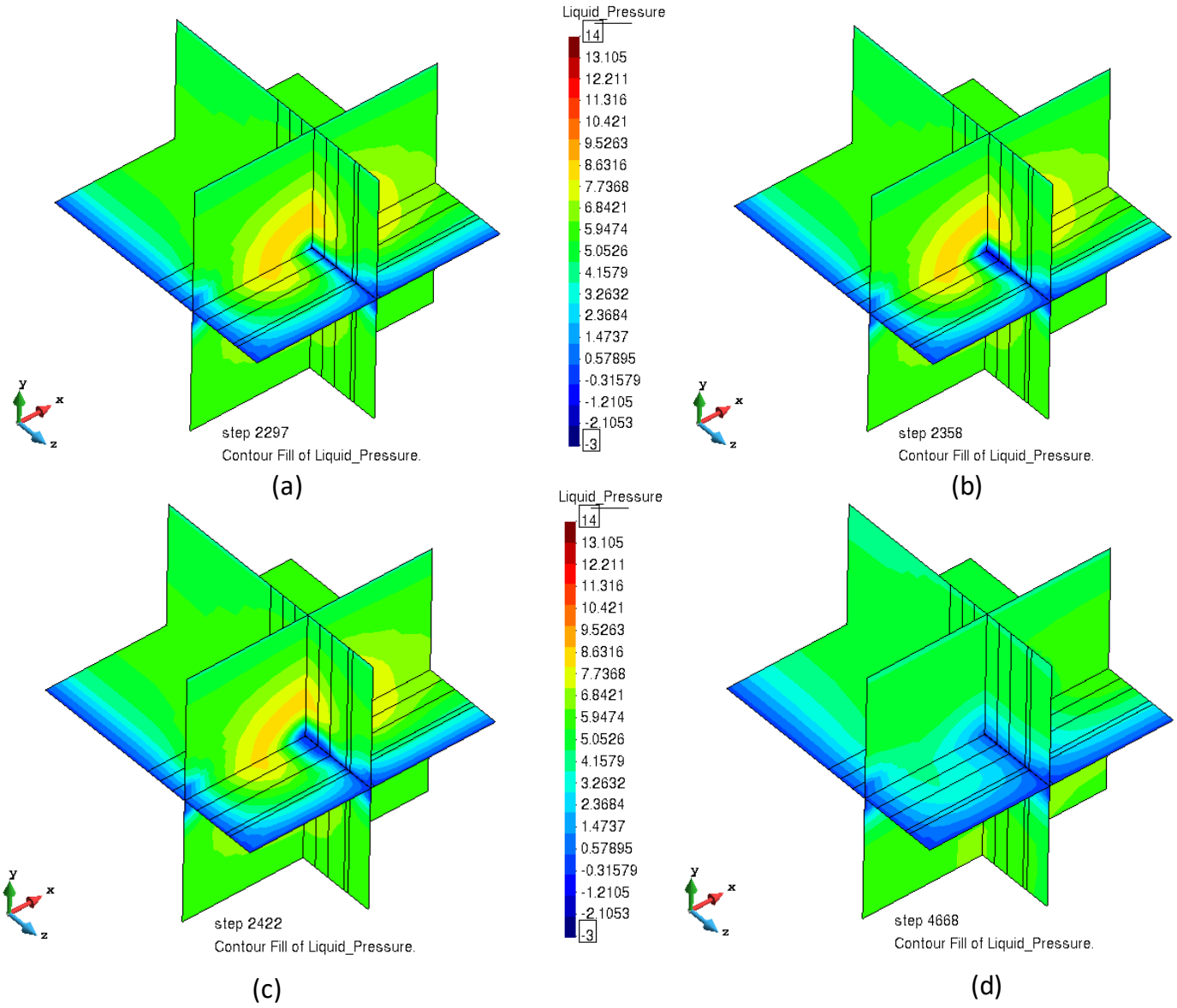

Figure 5-20 Computed contours of equal pore pressure increase (MPa) for: (a) 2297 days (End of heating); (b) 2358 days (End of first cooling phase); (c) 2422 days (End of second cooling phase); (d) 4668 days (6 years cooling).

In the remaining part of the section, a comprehensive comparison between computed and measured pore pressures at all the sensors is presented to highlight the consistence of the model. Two sets of results will be output:

- Pore pressures within the sections perpendicular to the bedding planes: Y = 13 m, (Figure 5-22) and Y = 17 m (Figure 5-25). These plots have been already discussed in Figure 5-16.
- Pore pressures along the boreholes lines: ALC1616 (Figure 5-24) and ALC1617 (Figure 5-25). Time evolutions and profiles at different times are shown.

For the sake of clarity, Figure 5-21 summarizes again the location of instrumentation around HA-ALC1604 experiment.

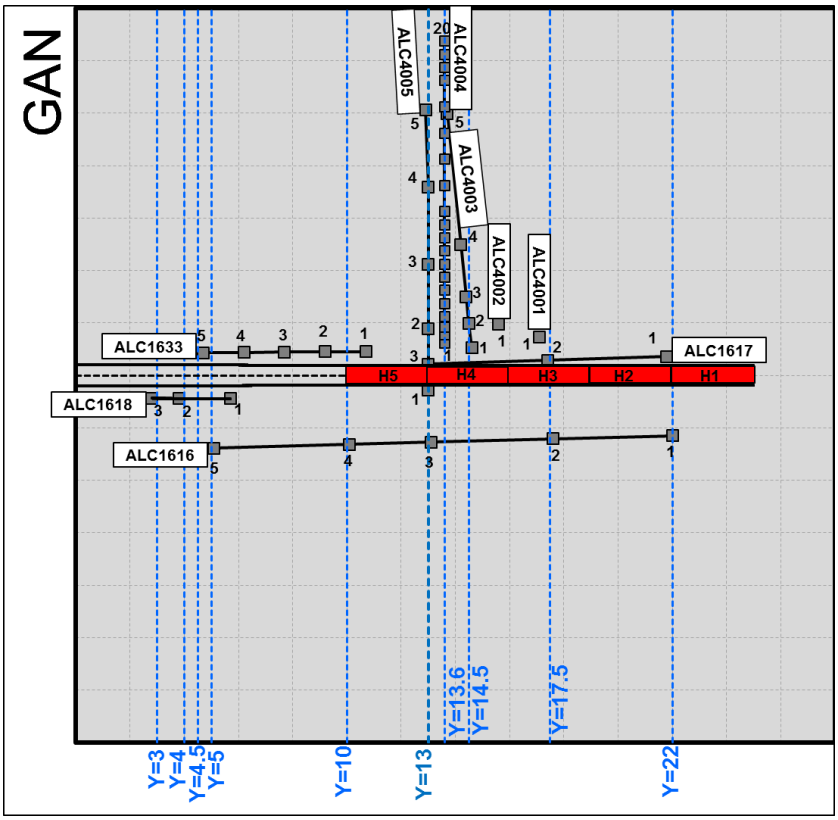

Figure 5-21. Horizontal view (bedding plane) of the instrumentation boreholes and perpendicular sections.

Section Y=13m

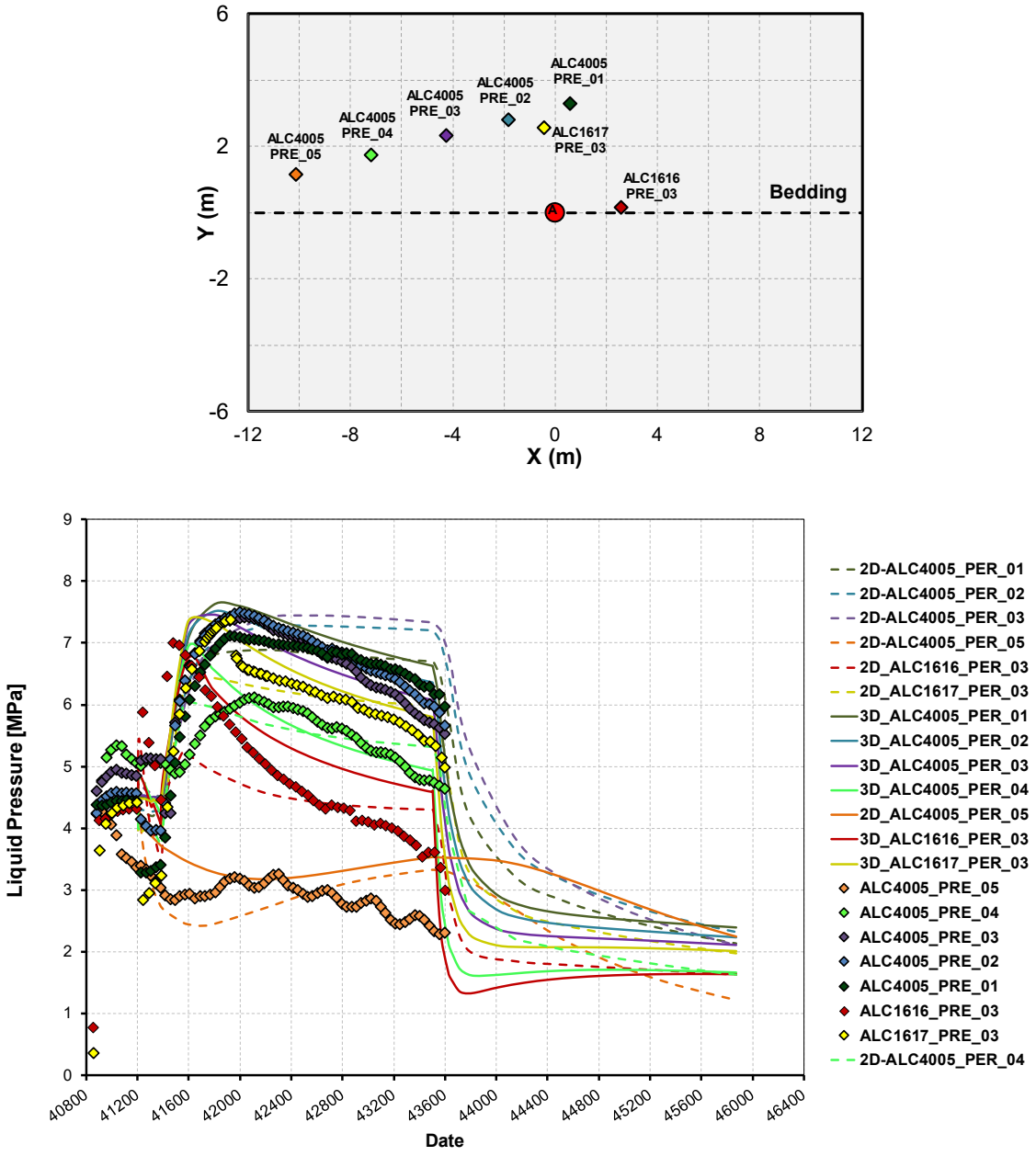

Figure 5-22 (a) Pore pressure evolution of sensors located in borehole ALC4005, ALC1616 and ALC1617 in section A2 at 13m from the entrance of the tunnel. (b) Pore pressure profile of sensors located in borehole ALC1616. The measurements (lines) performed are compared to the simulation results (dots).

Section Y=17.5m

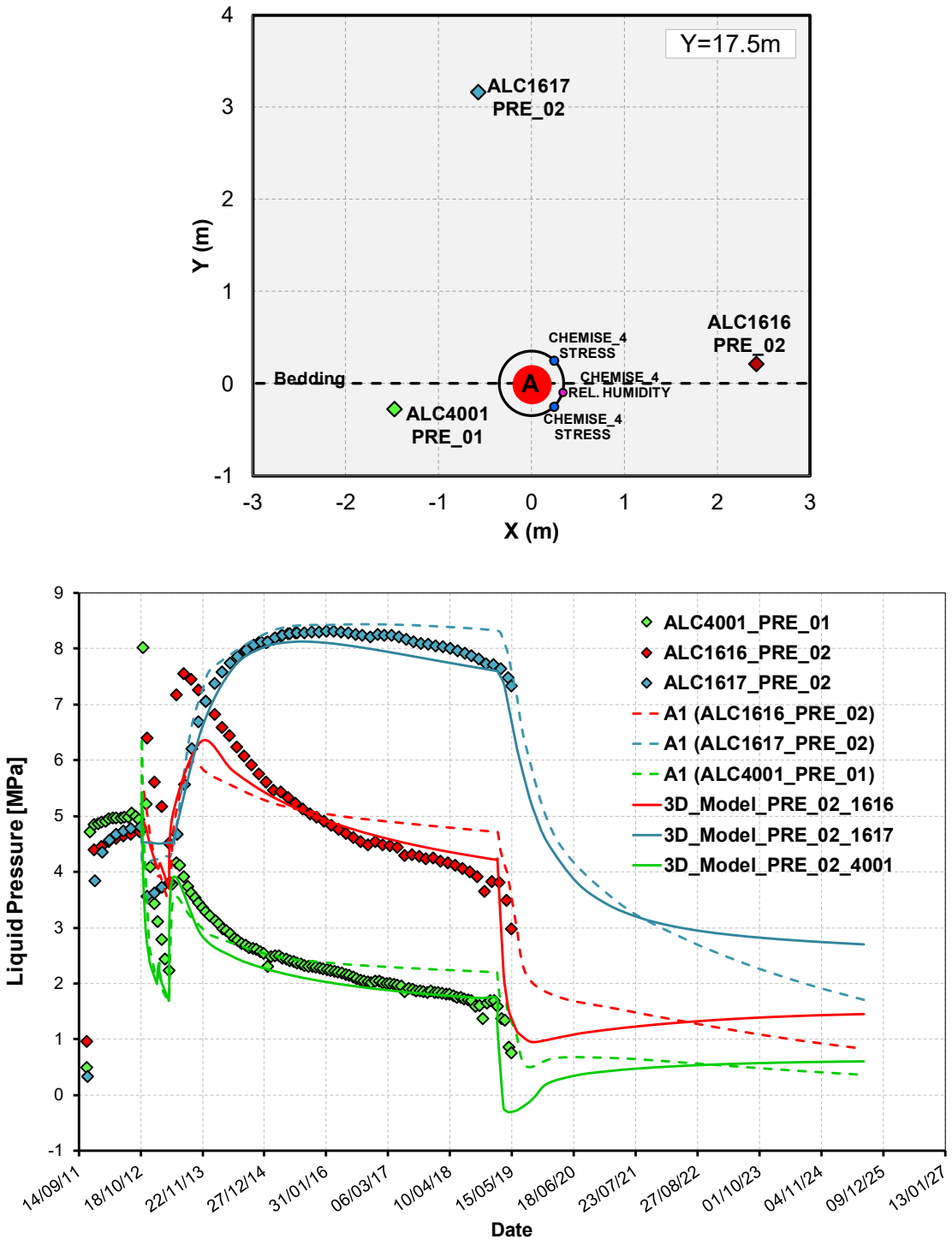

Figure 5-23 (a) Pore pressure evolution of sensors located in borehole ALC1616, ALC1617 and ALC4001 in section A1 at 17.5m from the entrance of the tunnel. ((From instrumentation emplacement to end of six years cooling).) The measurements (lines) performed are compared to the simulation results (dots).

Borehole ALC1616

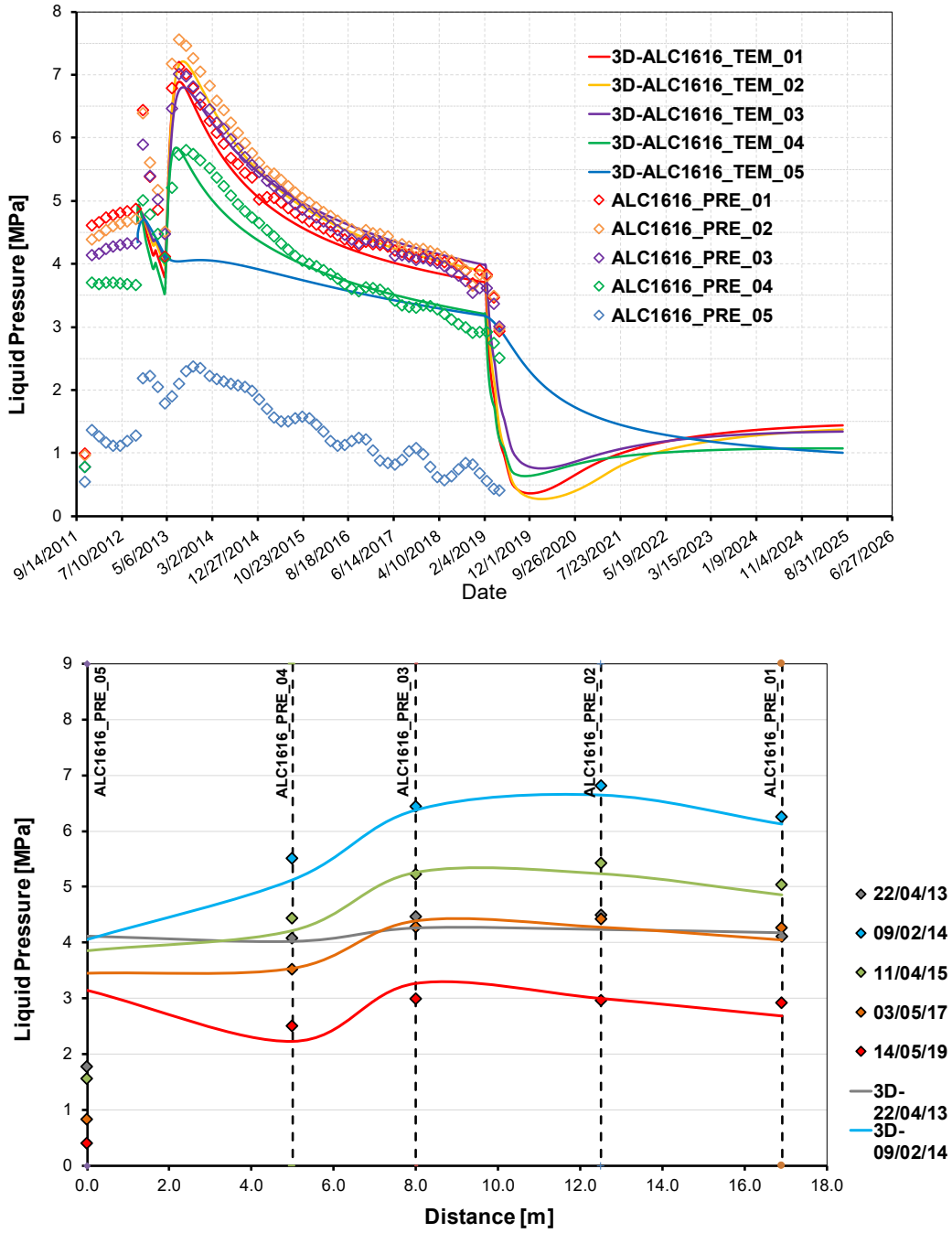

Figure 5-24 (a) Pore pressure evolution of sensors located in borehole ALC1616. (b) Pore pressure profile of sensors located in borehole ALC1616. The measurements (lines) performed are compared to the simulation results (dots).

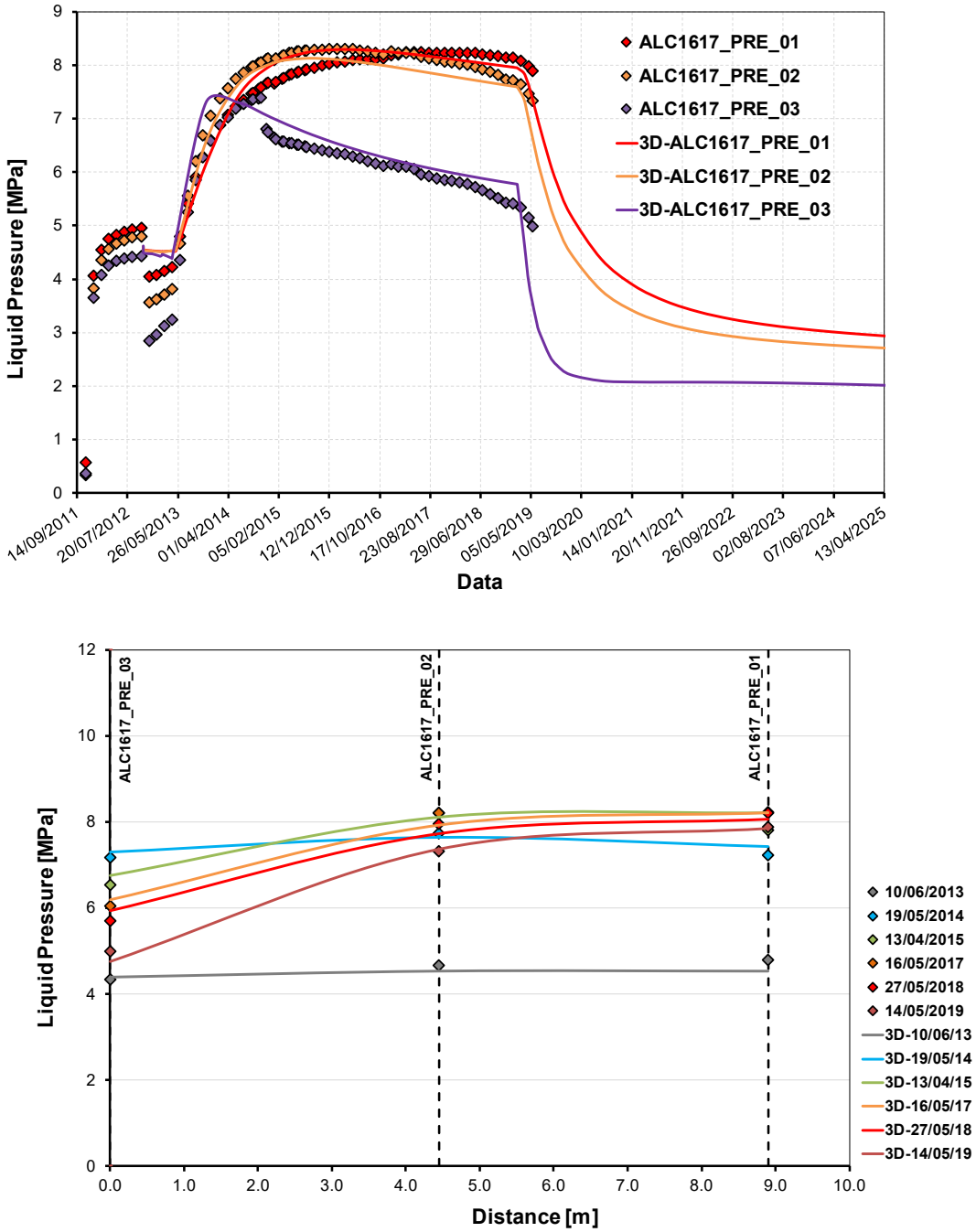

Figure 5-25 (a) Pore pressure evolution of sensors located in borehole ALC1617. (b) Pore pressure profile of sensors located in borehole ALC1617. The measurements (lines) performed are compared to the simulation results (dots).

5.3.3 Convergence Measurements

Figure 5-326 indicates the location of the instrumented sections for the sleeve and the. Each sleeve section is equipped with the following sensors (Figure 5-27):

- six strain gauge sectors at the sleeve intrados, with an axial gauge and a circumferential gauge for each sector; these sectors are positioned horizontally and at a 45° angle;
- a temperature sensor measuring the insert 15° below the horizontal axis;
- For section 9 (Figure 5-27), two convergence sensors for measuring the horizontal and vertical convergence of the sleeve.

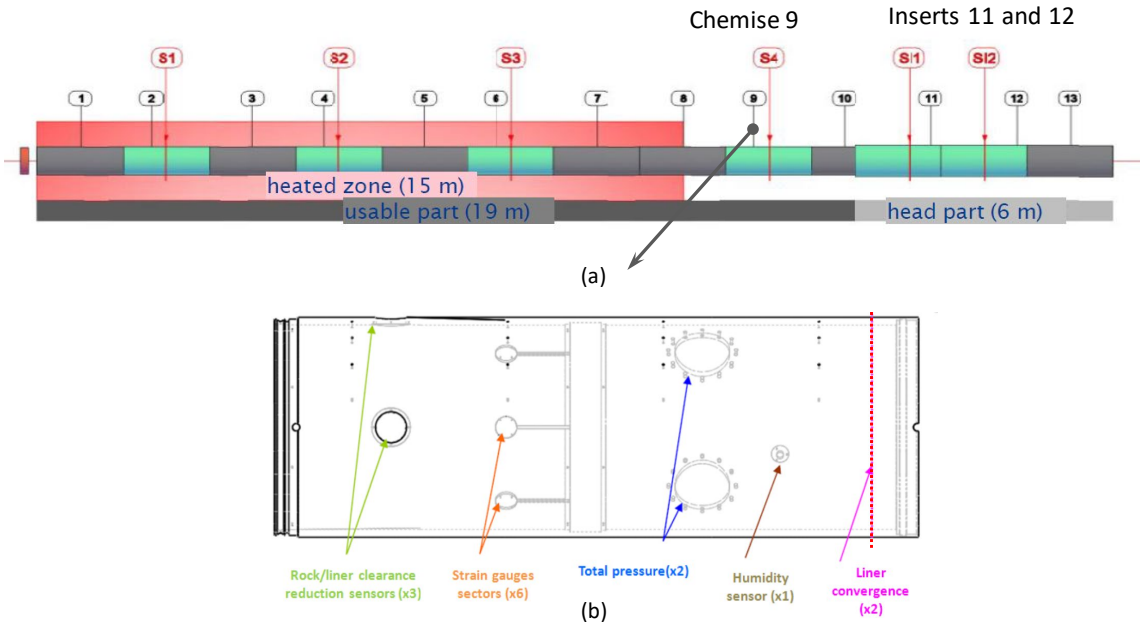

Figure 5-26 a) Location of the sleeve sections and insert sections equipped with sensors b) Location of the sensors on the sleeve sections equipped with instruments

Figure 5-28 shows the overall evolution of convergence measurements of the sleeve for section 9 (depth of 7 m), since the connection of the sensors (48 days after the micro-tunnel excavation). Although the in-situ stress field is almost isotropic in the cross-section (orthogonal to micro-tunnel) measurements exhibit an anisotropic load. This behaviour is consistent with the anisotropy of convergence measurements reported by (Morel *et al.*, 2013) and Armand et al. (2013).

Concerning sleeve response, three loading steps can be distinguished in Figure 5-28. In the first one, the radial load is localised in the horizontal direction corresponding to the maximum extension of the excavation induced fracture network. It can be observed that immediately after emplacement, the sleeve starts to converge in the horizontal direction, meaning that the theoretical initial annular space, which is about 3 per cent of the excavation diameter, is consumed in this direction in less than 25 days.

This loading results in the radial bending of the sleeve and the decrease in diameter. The heating phase sharply increases the sleeve convergence rate and thus its deformation, until contact with

the micro-tunnel vault occurs. In this step, the ovalization of the casing continues until it reaches the rock wall in the vertical direction. Once the annular space is taken up in the vertical direction, a second loading stage starts, characterized by the fact that mechanical load remains anisotropic with no impact on the sleeve convergence.

This second loading step is followed by the third one, corresponding to a progressive decrease of the load anisotropy, resulting in a decrease of the ovalization. After one year of heating, the convergence rate is less than 5 10^{-11} s^{-1}, which is of the same order of magnitude as the convergence rate measured in 5 m diameter drifts having the same orientation (Armand et al. 2013).

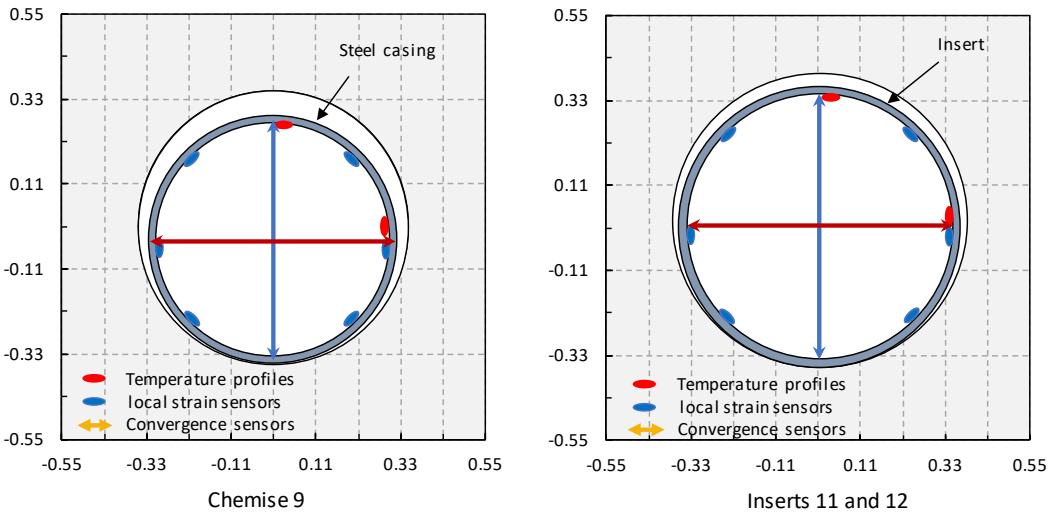

Figure 5-27 a) Location of measurements at a depth of 7m; b) Location of measurements at a depth of 4m and 2m.

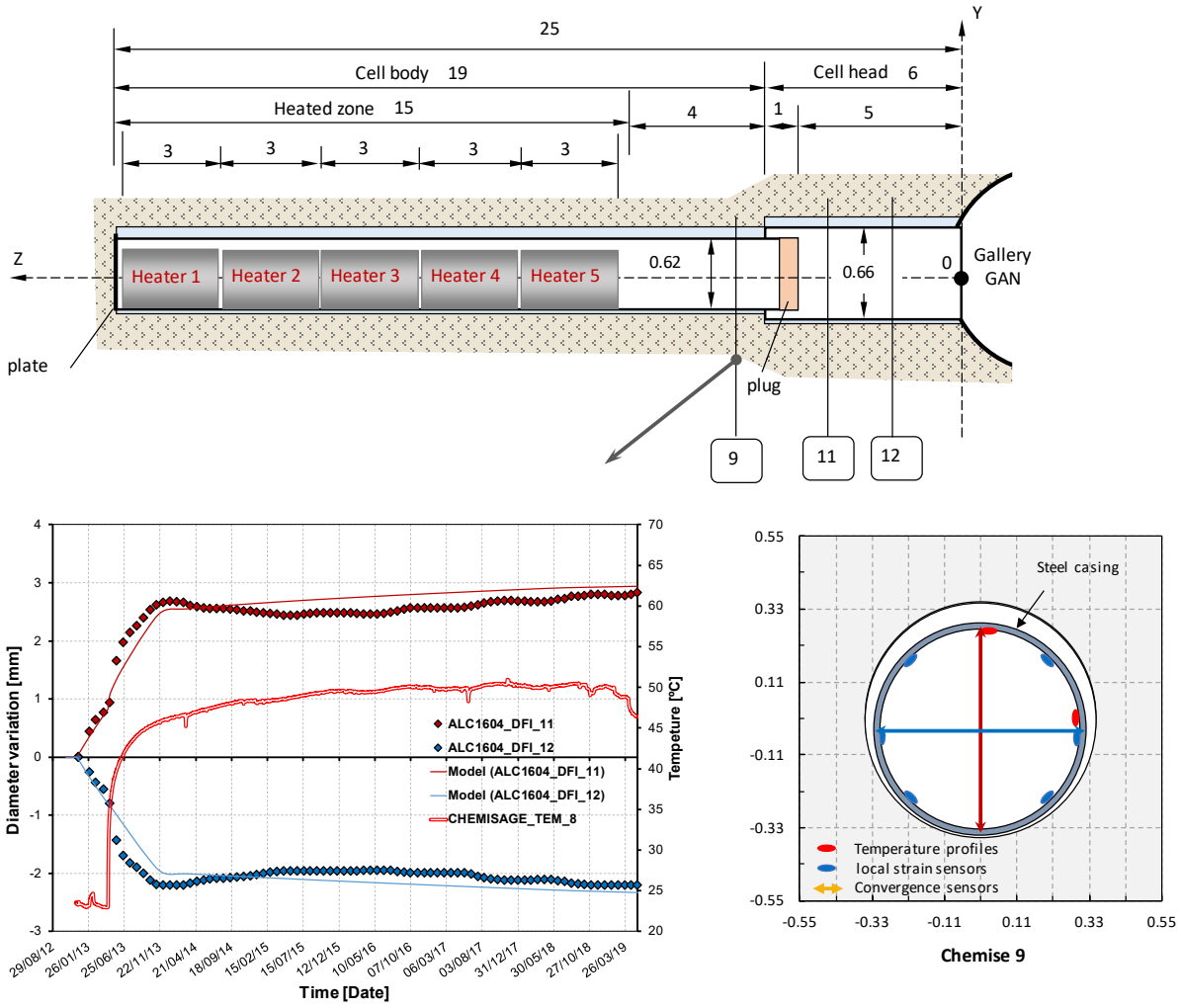

Figure 5-28 Diameter variations measured on the sleeve at a depth of 7 m (negative values correspond to convergence).

Figure 5-29 and Figure 5-30 present the horizontal and vertical convergence of insert sections 11 and 12. A similar short-term mechanical loading of the casing is observed at insert. However, after five years of measurements, the convergence of the insert is not stabilised, which means that they are still in the first loading step mentioned above. The behaviour of the insert sections does not show any significant heating impact (the sections were 8 and 6 meters behind the heated zone). On both sections, the loading scheme is the inverse of the one of the sleeve, consisting of vertical convergence and noticeably equivalent horizontal divergence.

A possible explanation relies on the fact that the annular space is much smaller at the insert level (initially 12 mm at the radius, compared with 25 mm around the sleeve). This behaviour could then be caused by the insert being in contact with the rock in the vertical and horizontal planes. As the mechanical strength of the rock was lower horizontally due to the damage generated during excavation, the insert tended to diverge horizontally. For both sections, the loading direction is reversed with respect to the sleeve, i.e. vertical convergence and noticeably equivalent horizontal divergence.

In all the cases, evolution and maximum convergence is reasonably well captured by the model.

More information from the numerical analysis is given in Figure 5-31 and Figure 5-32 in terms of displacement contours and vectors in a section across Heater 3 (section 17.5m) at various times. The following times have been selected for plotting: 176 days (end of the test heating stage a day before heating stage); 1285 days (three years heating); 2500 days (six-year heating); 4500 days (five years cooling). The anisotropic load distribution and ovalization of the casing are apparent in the figures. The figure also shows that the sleeve follows deforming during the cooling phase, as a result of creep effect.

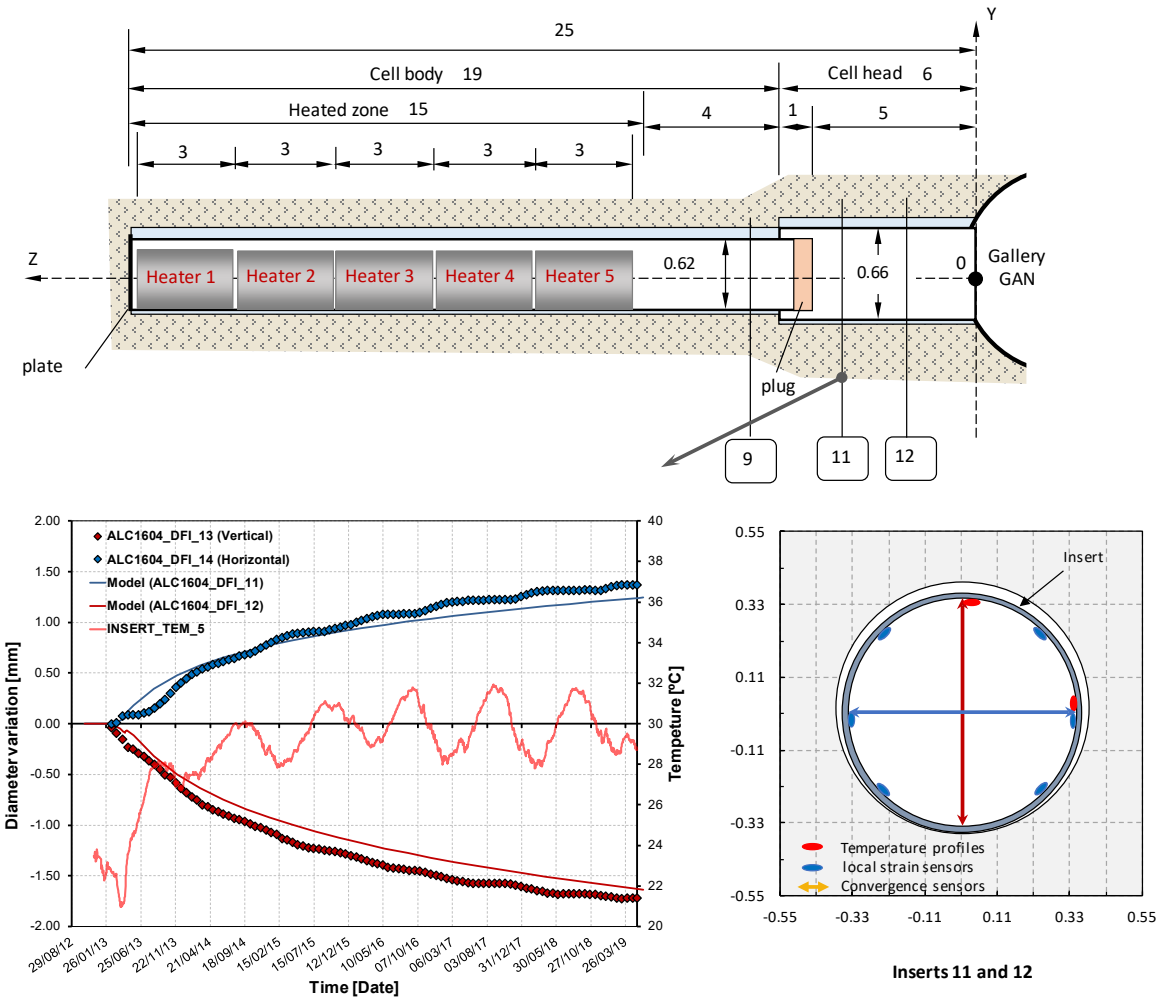

Figure 5-29 Diameter variations measured on the insert at a depth of 4m (negative values correspond to convergence).

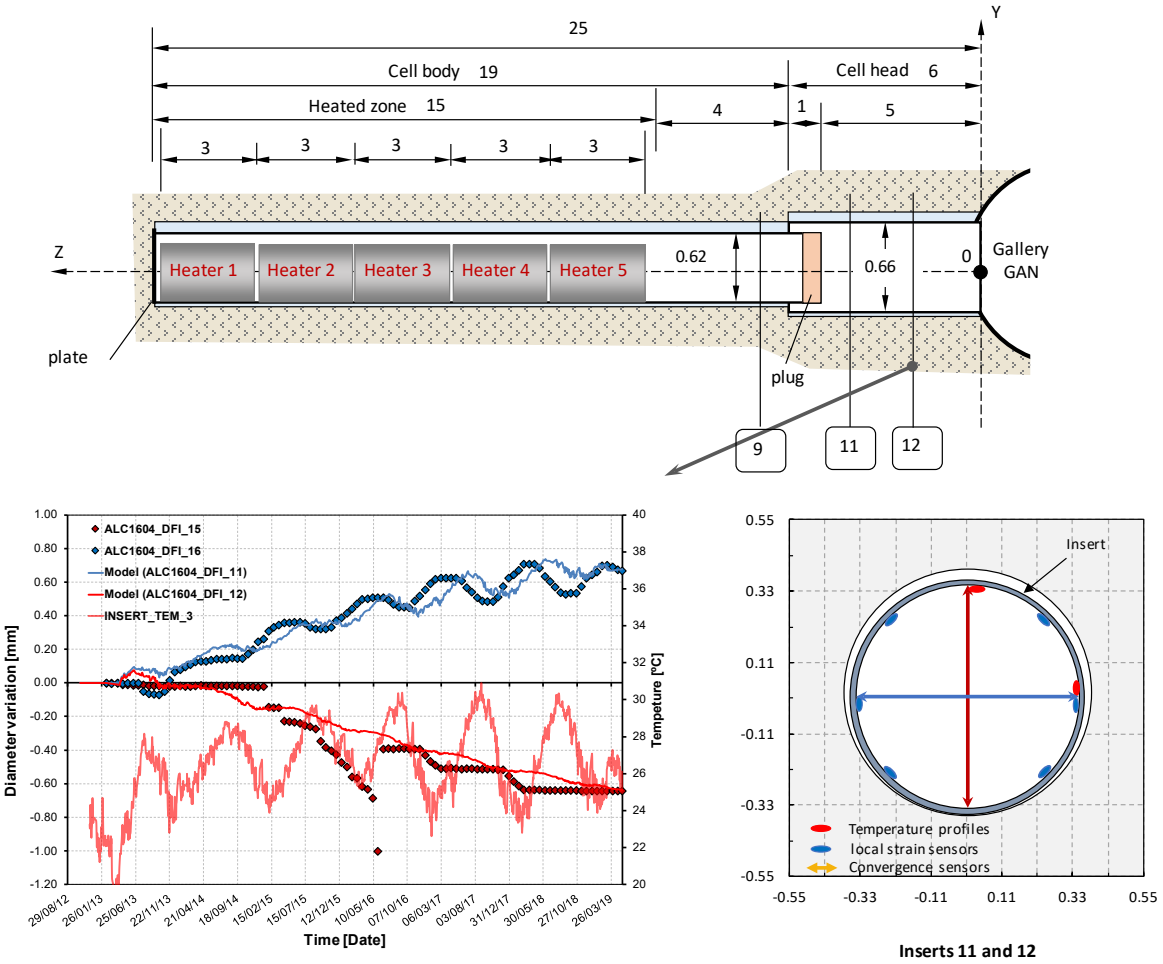

Figure 5-30 Diameter variations measured on the insert at a depth of 2m (negative values correspond to convergence).

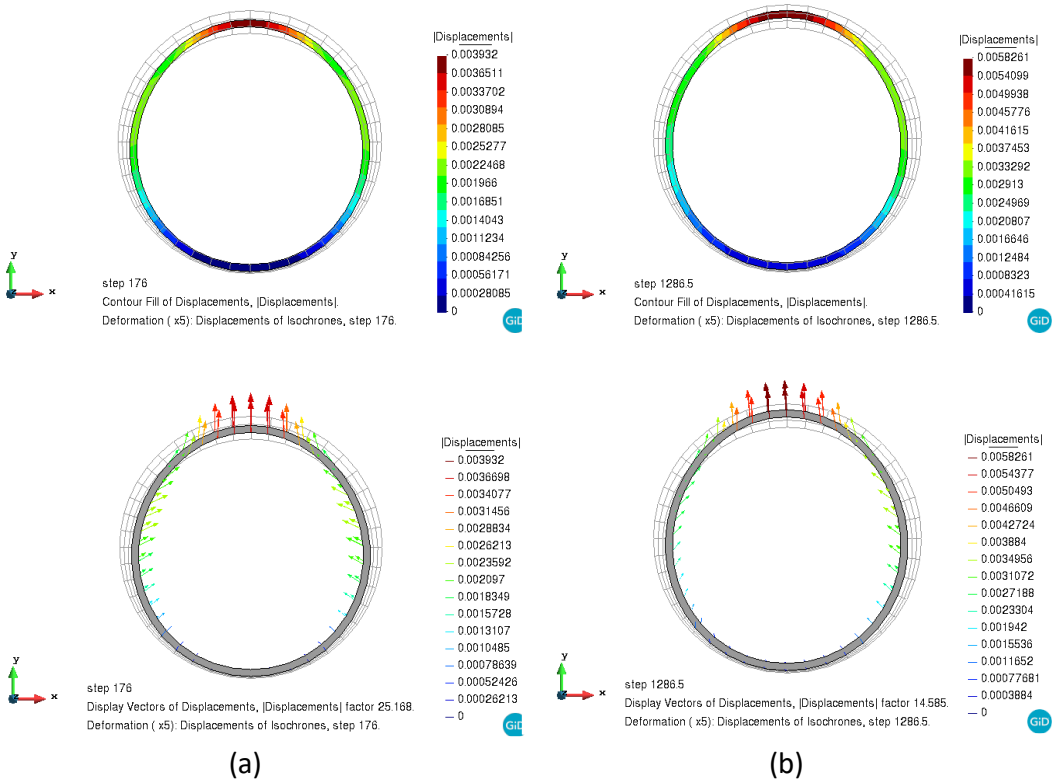

(a) (b)

Figure 5-31 Computed contours and display vectors of displacement in casing at section 17.5m for: (a) 176 days (before heating phase started); (b) 1285 days (three years heating test).

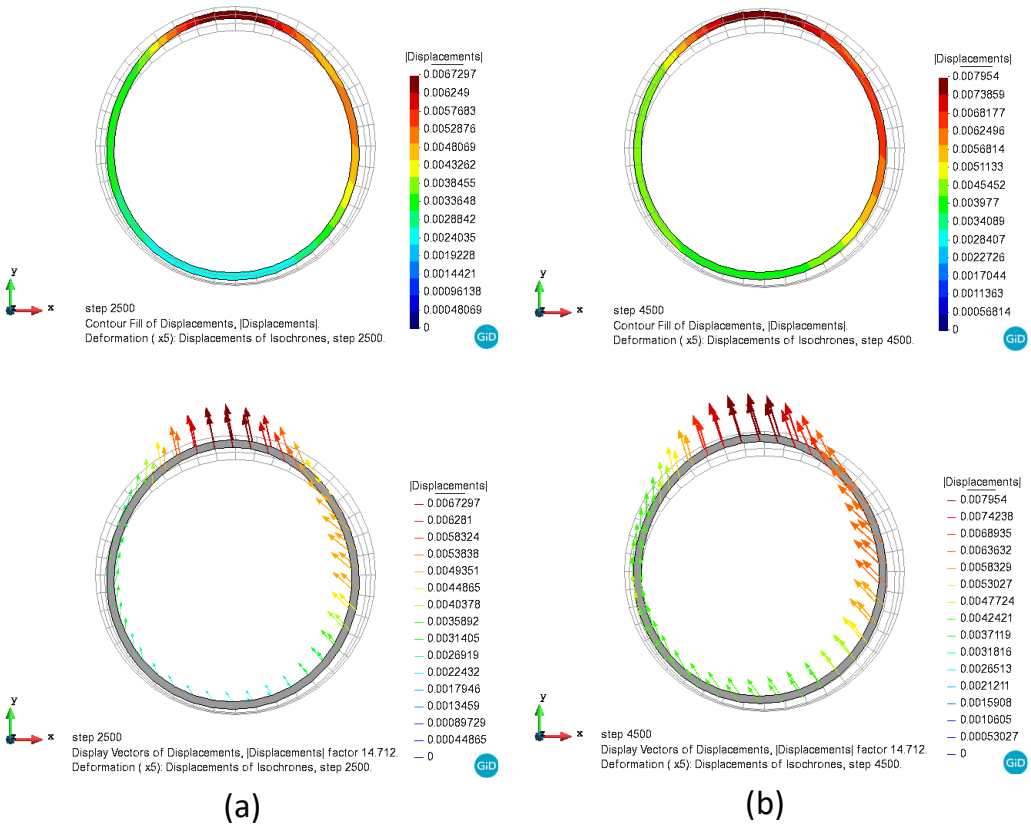

Figure 5-32 Computed contours of displacement of the casing at section 17.5m for: (a) 2500 days (six-year heating); (b) 4500 days (five years cooling).

5.3.4 Mechanical signatures

The strain gauges, which were preinstalled on the casing, were connected 27 days after the cell was excavated. For each section, the gauges are spread out into six sectors, two in the horizontal plane and the other four at 45° angles on either side of it.

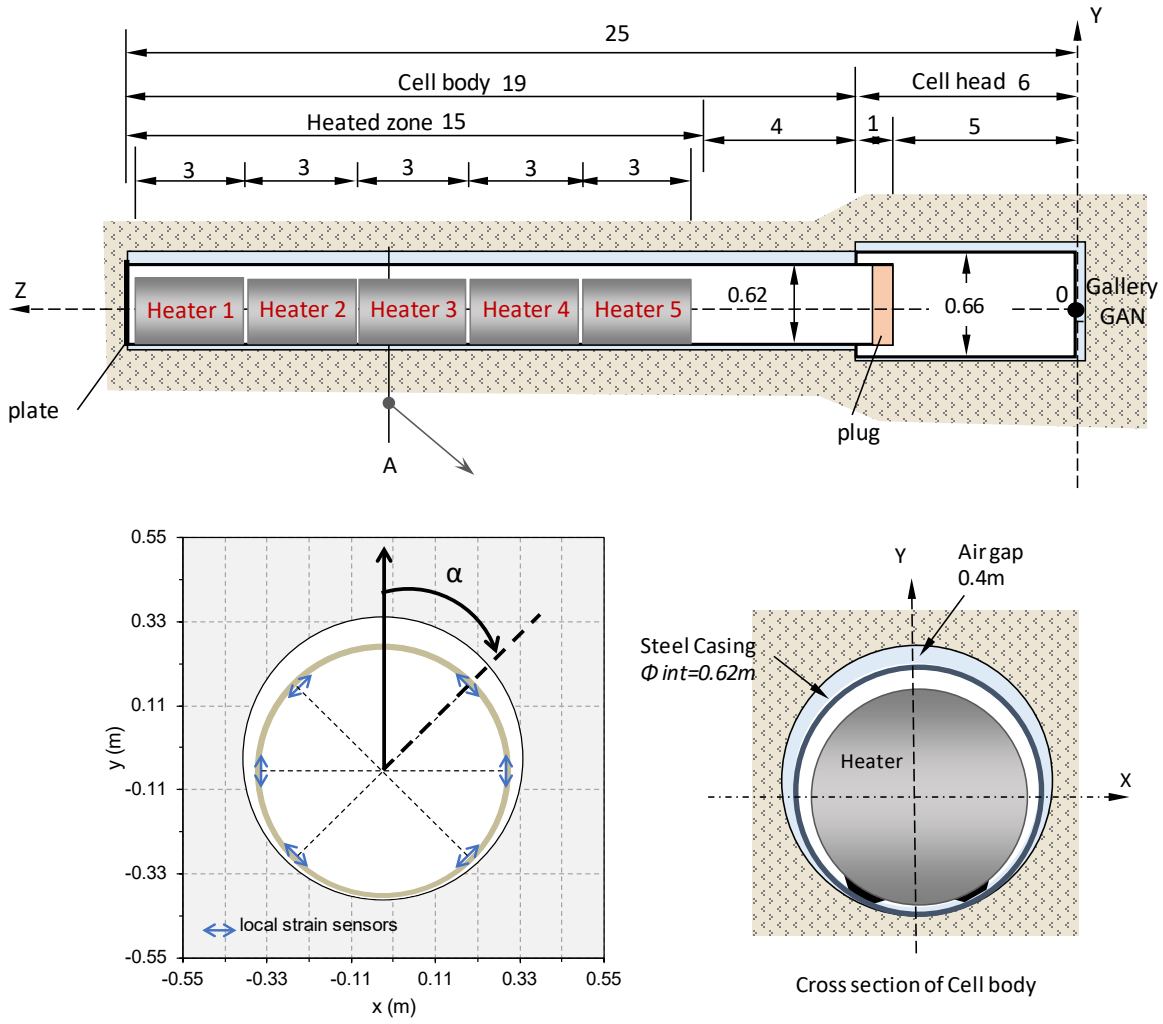

Figure 5-33 Location of circumferential mechanical strains observation points at a depth of 18m.

Figure 5-34 presents the evolution of the circumferential strain ($\varepsilon_{\theta\theta}$) around the inner face of the casing at different times and 18 m depth (section 4) with the computed results from the analysis. These evolutions tend towards a stabilised curve, which represents the mechanical signature of the applied load. Mechanical signatures of the loading applied by the rock (i.e. the evolution of the circumferential strain around the inner face of the casing) confirm the loading anisotropy. However, the casing does not evolve significantly after the second year of heating. By comparison with the numerical results, the maximum load axis can be determined. A maximum inclination of 30° concerning horizontal direction can be reached. However, they are representative of a mainly horizontal loading of the casing.

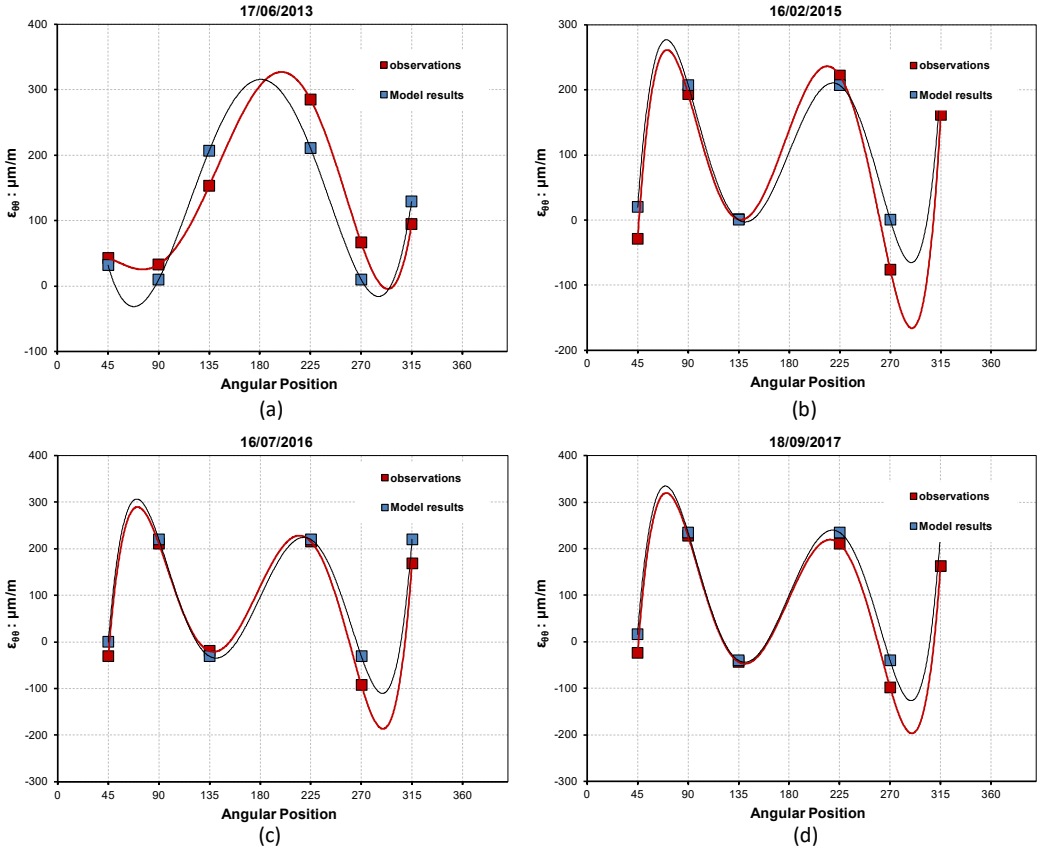

Figure 5-34 Evolution of circumferential mechanical strain at 18m depth for (a) 17/06/2013 (b) 11/08/2014 (c) 16/02/2015 (d) 16/07/2015 (e) 16/07/2016 (f) 18/09/2016.

6. Concluding remarks

This report presents the final modelling work carried out as a support to the interpretation of the HA-ALC1604 experiment.

The model is the outcome of the different simulations performed during the project, including:

1. 3D thermal analysis aiming at back-analysing the Callovo-Oxfordian thermal parameters,
2. 2D thermo-hydro-mechanical analysis for a preliminary interpretation of pore pressures around the experiment during the excavation and heating phases and deformation of the steel lining during heating,
3. Preliminary 3D thermo-hydro-mechanical modelling of the experiment.

The final modelling considers a three-dimensional geometry and includes most of material and experiment features:

- Transverse anisotropy for the host rock thermal conductivity, permeability and elastic stiffness.
- An anisotropic viscoplastic hardening/softening constitutive law with creep to model the Callovo-Oxfordian mudstone.
- A dependency of permeability on rock damage.
- Experiment geometry, including the host rock, excavated alveolus, steel lining, insert and the gaps between the steel lining and the rock, the steel lining and the insert and the insert and the rock.
- The different stages of the experiment (alveolus excavation, heating and cooling) in the same modelling.
- The thermo-hydraulic effect of the surrounding gallery
- The full anisotropy stress state.
- Material parameters are generally consistent with previous field and laboratory experiments or with values reported in the literature.

Comparison between numerical results and measurements provides a good agreement at all the sensors, evidencing the consistency of the model.

Aspects of particular interest are:

- Parameters specifically back analysed from experiment field measurements were the thermal conductivity, permeability, Young moduli and parameter of change in permeability with damage. Values obtained for the anisotropic parameters are:
  - $\lambda_{//} = 2.05\ W/m/K$
  - $\lambda_{\perp} = 1.33\ W/m/K$
  - $k_{//} = 2.10^{-20}\ m^2$
  - $k_{\perp} = 10^{-20}\ m^2$
  - $E_{//} = 5200\ MPa$
  - $E_{\perp} = 4000\ MPa$
- The simulation predicts an Excavated Damaged Zone similar in size and shape to the ones observed in the excavation of the same diameter that develops during the excavation of the alveolus. Further thermal loading appears not to affect the size of the EDZ and to increase marginally the damage intensity.

- Accounting for change of permeability within the EDZ is fundamental to reproduce well the pore pressure measurements.
- The deformation of steel lining can be well reproduced by the model.

Future improvements of the model would include a better representation of the EDZ accounting for deformation localization and the implementation of temperature dependency in the mechanical law of the host rock. (Hamidi, Tourchi and Khazaei, 2015; Tourchi and Hamidi, 2015; Hamidi, Tourchi and Kardooni, 2017; Tourchi, Gens, and others, 2017; Hamidi and Tourchi, 2018, 2018; Tourchi *et al.*, 2019a, 2019b)

References

Andra (2005) *Dossier 2005, Référentiel du site Meuse/Haute-Marne. Report CRPADS040022B*. Châtenay-Malabry: ANDRA.

Andra (2012) *Référentiel du comprotement des formations sur le site de Meuse/Haute Marne. Report D.RP.AMFS.1 2.0024*. Châtenay-Malabry: ANDRA.

Andra (2013) *Alveole chauffante ALC1604. Rapport d'installation et premier resultats. Document technique D.RP.AMFS.13.0013.* Châtenay-Malabry: ANDRA.

Armand, G. *et al.* (2013) 'Short- and long-term behaviors of drifts in the Callovo-Oxfordian claystone at the Meuse/Haute-Marne Underground Research Laboratory', *Journal of Rock Mechanics and Geotechnical Engineering*, 5(3), pp. 221–230. Available at: https://doi.org/10.1016/j.jrmge.2013.05.005.

Armand, G. *et al.* (2014) 'Geometry and properties of the excavation-induced fractures at the meuse/haute-marne URL drifts', *Rock Mechanics and Rock Engineering*, 47(1), pp. 21–41. Available at: https://doi.org/10.1007/s00603-012-0339-6.

Auvray, C. (2004) 'Thermomechanical tests on opalinus clays of the Mont Terri, ANDRA Report C', *RP. OENG*, pp. 4–239.

Blümling, P. *et al.* (2007) 'The excavation damaged zone in clay formations time-dependent behaviour and influence on performance assessment', *Physics and Chemistry of the Earth*, 32(8–14), pp. 588–599. Available at: https://doi.org/10.1016/j.pce.2006.04.034.

Bumbieler, F. *et al.* (2015) 'Mechanical And SCC Behavior Of An API5L Steel Casing Within The Context Of Deep Geological Repositories For Radioactive Waste', *ASME 2015 Pressure Vessels and Piping Conference*, pp. 1–11. Available at: https://doi.org/10.1115/PVP2015-45234.

Conil, N., Gatmiri, B. and Armand, G. (2010) *Premiers résultats de l'expérimentation TED*. Centre de Meuse/Haute-Marne, Rapport Andra D.RP.AMFS.10.0067.

DIT-UPC (2002) *A 3D program for thermo-hydro-mechanical analysis in geological media*, *Users guide*.

Gens, A. *et al.* (2007) 'In situ behaviour of a stiff layered clay subject to thermal loading: observations and interpretation', *Géotechnique*, 57(2), pp. 207–228. Available at: https://doi.org/10.1680/geot.2007.57.2.207.

Gens, A. *et al.* (2013) 'Homogenization in clay barriers and seals: Two case studies', *Journal of Rock Mechanics and Geotechnical Engineering*, 5(3), pp. 191–199. Available at: https://doi.org/10.1016/j.jrmge.2013.04.003.

Van Genuchten, M.T. (1980) 'A closed-form equation for predicting the hydraulic conductivity of unsaturated soils 1', *Soil science society of America journal*, 44(5), pp. 892–898.

Hamidi, A. and Tourchi, S. (2018) 'A thermomechanical constitutive model for unsaturated clays', *International Journal of Geotechical Engineering*, 12(2), pp. 185–199. Available at: https://doi.org/10.1080/19386362.2016.1260312.

Hamidi, A., Tourchi, S. and Kardooni, F. (2017) 'A critical state based thermo-elasto-plastic constitutive model for structured clays', *Journal of Rock Mechanics and Geotechnical Engineering*, 9(6), pp. 1094–1103. Available at: https://doi.org/10.1016/j.jrmge.2017.09.002.

Hamidi, A., Tourchi, S. and Khazaei, C. (2015) 'Thermomechanical constitutive model for saturated clays based on critical state theory', *International Journal of Geomechanics*, 15(1), p. 4014038. Available at: https://doi.org/10.1061/(ASCE)GM.1943-5622.0000402.

Mánica, M. *et al.* (2016) 'A time-dependent anisotropic model for argillaceous rocks. Application to an underground excavation in Callovo-Oxfordian claystone', *Computers and Geotechnics* [Preprint]. Available at: https://doi.org/10.1016/j.compgeo.2016.11.004.

Miguel Mánica; *et al.* (2016) 'A time-dependent anisotropic model for argillaceous rocks . Application to an underground excavation in Callovo-Oxfordian claystone', *Computers and Geotechnics* [Preprint]. Available at: https://doi.org/10.1016/j.compgeo.2016.11.004.

Morel, J. *et al.* (2013) 'Feasibility and behavior of a full scale disposal cell in a deep clay layer', in *ISRM International Symposium-EUROCK 2013*.

Olivella, S. *et al.* (1994) 'Non-isothermal multiphase flow of brine and gas through saline media', *Transport in Porous Media*, 15(3), pp. 271–293.

Olivella, S. *et al.* (1996) 'Numerical formulation for a simulator (CODE_BRIGHT) for the coupled analysis of saline media', *Engineering Computations*, 13(7), pp. 87–112. Available at: https://doi.org/10.1108/02644409610151575.

Potts, D.M. and Zdravkovic, L. (1999) 'Finite element analysis in geotechnical engineering. Theory', p. 440. Available at: https://doi.org/10.1680/feaiget.27534.

Seyedi, D.M. and Gens, A. (2017) 'Numerical analysis of the hydromechanical response of Callovo-Oxfordian claystone to deep excavations', *Computers and Geotechnics*, 85, pp. 275–276. Available at: https://doi.org/10.1016/j.compgeo.2017.03.006.

Sloan, S.W. and Booker, J.R. (1986) 'Removal of singularities in Tresca and Mohr–Coulomb yield functions', *International Journal for Numerical Methods in Biomedical Engineering*, 2(2), pp. 173–179.

Tourchi, S. *et al.* (2019a) 'Coupled THM analysis of long-term anisotropic convergence in the full-scale micro tunnel excavated in the Callovo-Oxfordian argillite', in E. Oñate, M. Papadrakakis, and B.A. Schrefler (eds) *VIII international conference on computational methods for coupled problems in science and engineering*. Sitges, Spain: ECCOMAS, pp. 292–299.

Tourchi, S. *et al.* (2019b) 'Thermo-hydro-mechanical simulation of a full-scale steel-lined micro-tunnel excavated in the Callovo-Oxfordian claystone', in E. Oñate et al. (eds) *XIV*

international conference on computational plasticity. Fundamentals and applications. Barcelona, Spain: ECCOMAS, pp. 544–552.

Tourchi, S., Gens, A., and others (2017) 'Thermo-Hydro-Mechanical modelling of full-scale in situ heating test in the callovo-oxfordian argillite', in *9th workshop of CODE_BRIGHT users*.

Tourchi, S. and Hamidi, A. (2015) 'Thermo-mechanical constitutive modeling of unsaturated clays based on the critical state concepts', *Journal of Rock Mechanics and Geotechnical Engineering*, 7(2), pp. 193–198. Available at: https://doi.org/10.1016/j.jrmge.2015.02.004.

Tsang, C.F., Bernier, F. and Davies, C. (2005) 'Geohydromechanical processes in the Excavation Damaged Zone in crystalline rock, rock salt, and indurated and plastic clays - In the context of radioactive waste disposal', *International Journal of Rock Mechanics and Mining Sciences*, 42(1), pp. 109–125. Available at: https://doi.org/10.1016/j.ijrmms.2004.08.003.

Appendix I Mechanical constitutive law for argillites

I.1 Introduction

The model used in this work has been developed by (Miguel Mánica; *et al.*, 2016), in which the both saturated and unsaturated conditions have been considered.

To this end, a generalized effective stress expression has been adopted:

$$\sigma' = \sigma + S_e s B \mathrm{I} \tag{I.1}$$

where σ' is the effective stress tensor, σ is the total stress tensor, S_e is the equivalent degree of saturation (defined below), s is suction, B is Biot's coefficient and I is the identity tensor. Naturally, for saturated conditions, equation (I.1) reduces to:

$$\sigma' = \sigma + p_l B \mathrm{I} \tag{I.2}$$

where liquid (water) pressure, p_l, is equated to –s. From a number of experimental and in situ observations of the behaviour of COx claystone, two main deformation mechanisms can be identified: a short-term response related to changes in the stress state and a time-dependent response occurring under constant stress.

I.2 Short-term response

The short-term response is described within the framework of elasto-plasticity. Under low deviatoric stresses the response is assumed cross-anisotropic elastic, with a vertical symmetry axis. In addition, vertical and horizontal Young's moduli depend on the effective mean stress according to:

$$E = E_1\left(p'\right) + E_2 \tag{I.3}$$

where E is the Young's modulus, p' is the mean stress, E_1 is a coefficient giving the rate of change and E_2 is the value of the modulus at zero mean stress.

At higher deviatoric stresses, plastic deformations develop. On reaching the yield surface, plastic strains accumulate that are physically related to the development and growth of microcracks and they are modelled by hardening plasticity. Therefore, further loads can be sustained by the material until reaching the failure surface that represents the maximum strength of the material. From that point onwards, strength is gradually reduced to its residual value. This is related to the coalescence of microcracks into macrocraks and it is modelled through softening plasticity. The Mohr-Coulomb criterion is used for both yield and failure limits.

In terms of stress invariants, this criterion is expressed by equation (I.4), which produces a cone in the principal stress space, with a hexagonal cross section in the deviatoric plane. Corners have been smoothed using (Sloan and Booker, 1986) procedure.

$$f = \left(cos\,\theta + \frac{1}{\sqrt{3}} sin\,\theta\, sin\,\varphi \right) J - sin\,\varphi \left(c\,cot\,\phi + p \right) = 0 \tag{I.4}$$

Where φ is the friction angle, c is the cohesion and the remaining variables are stress invariants given by the following expressions,

$$p' = \frac{1}{3}\left(\sigma_{xx} + \sigma_{yy} + \sigma_{zz} \right) \tag{I.5}$$

$$J = \left(\frac{1}{2} tr\mathbf{s}^2 \right)^{1/2} \tag{I.6}$$

where s is the deviatoric stress tensor $\mathrm{s} = \sigma - p\mathrm{I}$.

$$\varepsilon_{eq}^{p} = \left(\frac{2}{3} \varepsilon^{p} : \varepsilon^{p} \right)^{1/2} \tag{I.7}$$

where ε^{p} is the plastic strain tensor. The friction angle varies in a piecewise manner as shown in Table I.1; the evolution laws corresponding to each zone are given in Figure I. 1. Cohesion evolves in parallel with the friction angle according to:

$$c_{mov} = c_{peak}\, \cot \varphi_{ini}\, \tan \varphi_{mov} \tag{I.8}$$

Table I.2 Evolution laws for the mobilized friction angle

Zone 1	$\varphi_{mov} = \varphi_{ini} + \dfrac{\varepsilon_{eq}^{p}}{a_{hard} + \dfrac{\varepsilon_{eq}^{p}}{\Delta\varphi_{hard}}}, \quad \Delta\varphi_{hard} = \dfrac{\xi_1}{\dfrac{\xi_1}{\varphi_{peak} - \varphi_{ini}} - a_{hard}}$
Zone 2	$\varphi_{mov} = \varphi_{peak}$
Zone 3	$\varphi_{mov} = \varphi_{peak} - \dfrac{\varepsilon_{eq}^{p} - \xi_2}{a_{soft} + \dfrac{\varepsilon_{eq}^{p} - \xi_2}{\Delta\varphi_{soft}}}, \quad \Delta\varphi_{soft} = \dfrac{\xi_3 - \xi_2}{\dfrac{\xi_3 - \xi_2}{\varphi_{peak} - \varphi_{res}} - a_{soft}}$
Zone 4	$\varphi_{mov} = \varphi_{res}$

φ_{mov} = mobilized friction angle, φ_{res} = residual friction angle, ξ_1 = equivalent plastic strain at which the maximum strength is reached, ξ_2 = equivalent plastic strain at which softening begins, ξ_3 = equivalent plastic strain at which the residual strength is reached, a_{hard} = constant that controls the curvature of the function in the hardening branch, a_{soft} = constant that controls the curvature of the function in the softening branch.

where c_{mov} is the mobilized cohesion.

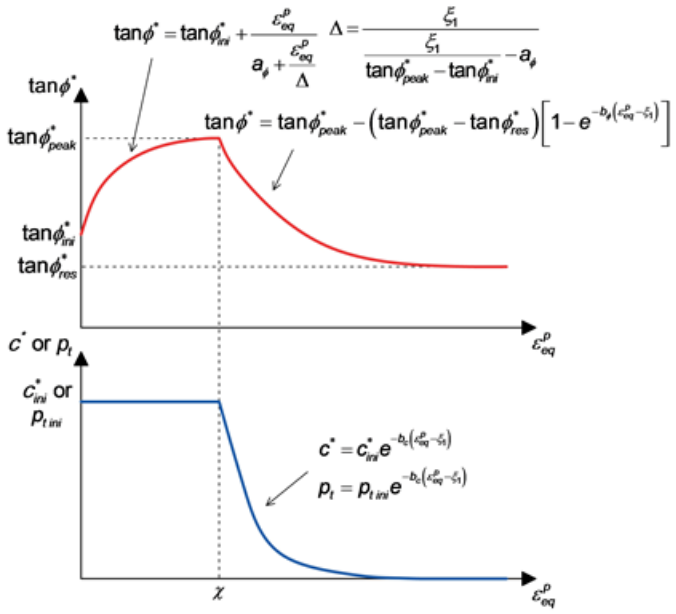

Figure I. 2 Friction angle evolution in hardening and softening regimes

It is well known that associated flow rules for geomaterials tend to overestimate volumetric strains during plastic flow. Therefore, a non-associated flow rule is adopted in the model.

Rather than deriving a specific function for the plastic potential, the flow rule is directly obtained from the yield/failure criterion in the following way,

$$\frac{\partial g}{\partial \sigma'} = \omega \frac{\partial f}{\partial p}\frac{\partial p}{\partial \sigma'} + \frac{\partial f}{\partial J}\frac{\partial J}{\partial \sigma'} + \frac{\partial f}{\partial \theta}\frac{\partial \theta}{\partial \sigma'} \tag{I.9}$$

where g is the plastic potential and ω is a constant that controls the volumetric component of plastic deformations. With $\omega = 1$ an associated flow rule is recovered, while with $\omega = 0$ no volumetric plastic strains occur. An adequate value for geomaterials usually lies between these limits. The model has been extended to consider cross-anisotropy through a non-uniform scaling of the stress tensor, as described in (Mánica *et al.*, 2016).

As Figure I. 3 Shows, the local coordinate system 1-2-3 corresponds to the principal axes of anisotropy with direction "2" oriented orthogonal to the isotropic plane. In a general case, the global coordinate system, x-y-z, does not coincide with the local anisotropy one.

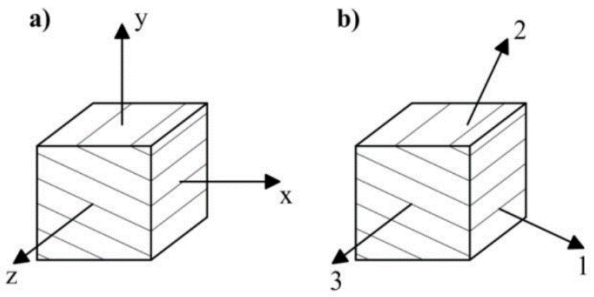

Figure I. 4 (a) Global and (b) local coordinate systems

Transformation of the stress tensor from global to local coordinates is achieved via the usual rotation transformation:

$$\sigma^{loc} = a\ \sigma\ a^{T} \tag{I.10}$$

where σ^{loc} is the stress tensor orientated with the local coordinate system, and a is the rotation matrix:

$$a = \begin{bmatrix} \cos\beta\cos\alpha & \sin\beta & -\cos\beta\sin\alpha \\ -\cos\alpha\sin\beta & \cos\beta & \sin\beta\sin\alpha \\ \sin\alpha & 0 & \cos\beta\cos\alpha \end{bmatrix} \tag{I.11}$$

where α and β are the angles indicated in Figure 3.

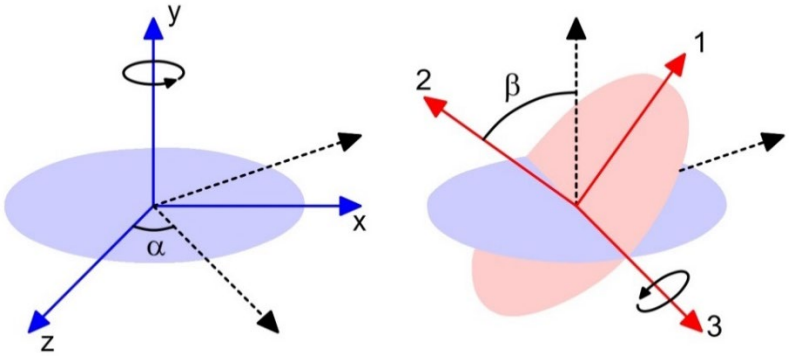

Figure I. 5 Definition of the angles in the rotation

The cross-anisotropic extension of the model is obtained by replacing p', J and θ in Eq. (16) by p'^{ani}, J^{ani} and θ^{ani} respectively. These variables are invariants with the same definition as shown in Eq. (17) but calculated from the anisotropic stress tensor σ'^{ani}. This tensor is obtained through the non-uniform scaling of the effective stress tensor oriented with the local coordinate system (σ^{loc}), as shown below

$$\mathrm{a} = \begin{bmatrix} \dfrac{\sigma_{11}^{loc}}{c_N} & c_s\sigma_{12}^{loc} & \sigma_{13}^{loc} \\ c_s\sigma_{12}^{loc} & c_N\sigma_{22}^{loc} & c_s\sigma_{23}^{loc} \\ \sigma_{13}^{loc} & c_s\sigma_{23}^{loc} & \dfrac{\sigma_{33}^{loc}}{c_N} \end{bmatrix} \tag{I.12}$$

where c_N and c_s are the normal and shear scaling factors respectively. An appropriate selection of strength parameters and scaling factors allows a satisfactory matching of a specified strength variation with loading orientation. Details about the physical meaning of the anisotropy parameters, their effects and of the derivation of the corresponding elastoplastic constitutive matrix are given in (Mánica *et al.*, 2016).

I.3 Time-dependent response

For the time-dependent response, an additional mechanism is considered characterized by a modified form of Lemaitre's law. Assuming small strains, the total strain increment is decomposed as the sum of the two mechanisms,

$$d\varepsilon = d\varepsilon^{ep} + d\varepsilon^{vp} = d\varepsilon^{ep} + \Delta t\left(\dot{\varepsilon}^{vp}\right) \tag{I.13}$$

where $d\varepsilon$ is the total strain increment; $d\varepsilon^{ep}$ is the elastoplastic strain increment, related to the short-term response; $d\varepsilon^{vp}$ is the viscoplastic strain increment, related to the time-dependent response; Δt is the time increment, and $\dot{\varepsilon}^{vp}$ is the viscoplastic strain rate tensor.

It is assumed that viscoplastic deformations are mainly caused by deviatoric stresses, and the strain rates are given by:

$$\dot{\varepsilon}^{vp} = \frac{2}{3}\frac{\dot{\varepsilon}^{vp}}{q}s \tag{I.14}$$

$$q = \left(\frac{3}{2}\mathrm{s} : \mathrm{s}\right)^{1/2} \tag{I.15}$$

$$\dot{\varepsilon}^{vp} = \gamma\left(q - \sigma_s\right)^n\left(1 - \varepsilon_{eq}^{vp}\right)^m \tag{I.16}$$

where γ is a viscosity parameter, σ_s is a threshold from which viscoplastic strains are s activated, n and m are material constants, and ε_{eq}^{vp} is the state variable of the time-dependent response given by,

$$\varepsilon_{eq}^{vp} = \int_0^t \left(\frac{2}{3}\dot{\varepsilon}^{vp} : \varepsilon^{vp}\right)^{1/2} dt \tag{I.18}$$

In this way, larger viscoplastic strain rates are obtained for higher deviatoric stresses, and those rates decrease as viscoplastic strains accumulate in time, as observed in laboratory tests. In the numerical implementation, an explicit scheme is employed, i.e. viscoplastic strains are computed from the stress state at the beginning of the step. These strains are subtracted from the total strain increment, and the elastoplastic relationship is integrated only for $d\varepsilon^{ep}$ using now an implicit scheme. This procedure allows for preserving the standard format of the elastoplastic constitutive matrix, and it is considered accurate enough if small time steps are used.